FLUORESCENCE DYNAMICS OF DYE-DYE AND DYE-NANOSTRUCTURES INTERACTIONS

by

Sabriye Açıkgöz

B.S., Physics, Marmara University, 2003

M.S., Physics, Boğaziçi University, 2006

Submitted to the Institute for Graduate Studies in
Science and Engineering in partial fulfillment of
the requirements for the degree of
Doctor of Philosophy

Graduate Program in Physics

Boğaziçi University

2011

ACKNOWLEDGEMENTS

Firstly, I would like to thank my supervisor, Prof. M. Naci İnci. I could not have imagined having a better advisor and mentor for my PhD, and without his common-sense, knowledge, perceptiveness and encouragement, I would never have completed my PhD. I would like to extend my special thanks to Dr. Amitav Sanyal for his guidance.

I want to thank my husband, Erkan, who always stands next to me with all his love, patience and wisdom. Words cannot suffice to describe how much he supported me during the preparation of this thesis; I could never imagine going through this year without him. I would like to thank my dearest daughter, Elif Tuğçe, who has brought joy into our life and has give us another reason to carry on.

Finally, I owe a great deal of gratitude to my parents. They have been a constant source of love and encouragement throughout the long road of my academic career.

ABSTRACT

FLUORESCENCE DYNAMICS OF DYE-DYE AND DYE-NANOSTRUCTURES INTERACTIONS

The decay dynamics of (Boradiazaindacene) BODIPY dye molecules embedded in Porous silicon (PSi) nanostructures produced by electrochemical anodization of p-type silicon wafers in an HF solution are investigated using time-resolved lifetime measurements. Illumination light and resistivity effects on the growth mechanism of the PSi are studied. Coherence is observed to be the foundation of regularity in obtaining conical shapes and the pillar size is almost linearly proportional to the illumination wavelength. Moreover, high resistivity of silicon wafer considerably changes the surface topography of the PSi and silicon nanospheres are obtained instead of nanopillars. The decay rate of the BODIPY embedded in the vicinity of various size pillar tips is affected due to different apex angles of the conical nature. Interaction between BODIPY and nanospheres is explained using confocal FLIM technique. It is observed that there is an efficient energy transfer mechanism between BODIPY and PSi. Energy transfer efficiency strongly depends on the thickness of the silicon dioxide layer covering the PSi. As oxidation increases, energy transfer rate decreases. This change in energy transfer rate seems to obey NSET mechanism, which allows us to obtain a three dimensional topographic map of the developed oxide layer on the rough and complicated surface of a PSi nanostructure. Finally, interaction between BODIPY dye molecules, which are covalently bound to a PEG based hydrogel is also studied. Since the hydrogel structure is capable of absorbing a large amount of water, without dissolving and losing its shape, upon swelling, the distance between the BODIPY dyes is controllably changed; it is observed that the fluorescence lifetime of BODIPY increases. The decay dynamics of the BODIPY dye molecules confined within a hydrogel cluster obeys FRET rather than self (or contact) quenching.

ÖZET

BOYA MOLEKÜLLERİNİN BİRBİRLERİYLE VE NANOYAPILARLA ETKİLEŞİMLERİNİN IŞIMA DİNAMİĞİ

Elektrokimyasal anodizasyon metodu ile hazırlanan Gözenekli silikon (PSi) nano yapılar üzerine yerleştirilen BODIPY boya moleküllerinin ışıma karakterleri zaman ayrımlı yarıömür ölçümleri yapılarak incelenmiştir. Aydınlatma ışığı ve silikon levhanın direnç değerinin PSi oluşması üzerindeki etkileri araştırılmıştır. Eş fazlı ışık kaynağı kullanıldığı zaman düzenli konik yapıların oluştuğu ve nano boyuttaki bu yapıların büyüklüğünün ışık kaynağının dalgaboyu ile orantılı olduğu gözlemlenmiştir. Ayrıca, yüksek direnç değerine sahip olan silikon levha kullanıldığında, PSi yüzeyinde oluşan yapıların karakteri değişmiş ve konik tepeler yerine nano boyutta küreler elde edilmiştir. Nano tepeciklere yerleştirilen boya moleküllerinin ışıma oranı, konik yapıların tepe açılarına bağlı olarak değişir. BODIPY ve küre şeklindeki nano yapılar arasındaki etkileşim ise konfokal FLIM tekniği ile incelenmiştir. BODIPY ve nano yapılar arasında enerji tranferinin söz konusu olduğu ve transfer miktarının PSi yüzey üzerinde oluşan silikon dioksit tabakasının kalınlığına bağlı olduğu gözlemlenmiştir. Oksit tabakasının kalınlığı arttıkça, enerji transfer miktarı ise giderek azalmaktadır. Enerji transfer oranı NSET modeli kullanılarak hesaplanabilir ve böylece PSi yüzey üzerinde oluşan oksit tabakasının üç boyutlu haritası elde edilmiş olur. Son olarak, hydrogel içerisine kovalent bağlarla bağlanan BODIPY molekülleri arasındaki etkileşim incelenmiştir. Hydrogel çözünmeden ve yapısal değişime uğramadan içine su alabilme ve şişme özelliğine sahip olduğundan, boya molekülleri arasındaki mesafe kontrollü bir şekilde değiştirilebilir. Şişme sonucunda boya moleküllerinin ışıma yarıömürleri artar. Hydrogel içine yerleştirilen BODIPY boya moleküllerinin ışıma karakteri boya konsantrasyonuna bağlı sönmeden daha çok FRET teorisine uymaktadır.

TABLE OF CONTENTS

LIST OF FIGURES

LIST OF TABLES

LIST OF SYMBOLS

A_{21}	Einstein coefficient
c	Speed of light
d_0	Characteristic distance length for NSET model
D_{axial}	Axial resolution
$D_{pinhole}$	Pinhole diameter
E	Energy transfer efficiency
E_F	Fermi energy level
E_g	Band gap energy
F	Fluorescence intensity in the presence of the quencher
F_0	Fluorescence intensity in the absence of the quencher
F_D	Fluorescence intensity in the absence of the acceptor
F_{DA}	Fluorescence intensity in the presence of the acceptor
$F_D(\lambda)$	Normalized fluorescence intensity of the donor
J	Overlap integral
K_D	Stern-Volmer contant for dynamic quenching
k_F	Fermi wavevector
k_q	Bimolecular quenching constant
K_S	Stern-Volmer contant for static quenching
k_T	Energy transfer rate
M_E	Demodulation ratio
n	Refractive index
NA	Numerical aperture
$n(t)$	Number of molecules in the excited state
$[Q]$	Quencher concentration
R_0	Förster distance
r	Distance between donor and acceptor molecules
$r_{lateral}$	Lateral resolution
$\%S$	Swelling ratio

α	Vertex angle of a nanopillar
γ_{nr}	Nonradiative spontaneous emission decay rate
γ_r	Radiative spontaneous emission decay rate
λ	Wavelenght
$\varepsilon_A(\lambda)$	Extinction spectrum of the acceptor
κ^2	Orientation factor
λ	Wavelength
ϕ_d	Quantum yield of donor molecule
τ_{DA}	Fluorescence lifetime of donor in the presence of acceptor
τ_D	Fluorescence lifetime of donor in the absence of acceptor
θ_T	Angle between the donor dipole and acceptor dipole
θ_D	Angle between the donor dipole and **r** joining vector
θ_A	Angle between the acceptor dipole and **r** joining vector
ϕ	Phase angle shift
ω_{dye}	Angular frequency of the dye molecule
ω_F	Fermi frequency
ω_p	Plasma frequency
Ω	Vibration frequency of the dipole

LIST OF ACRONYMS/ABBREVIATIONS

A	Acceptor molecule
APD	Avalanche photodiode
BODIPY	Boradiazaindacene
CW	Continuous wave
D	Donor molecule
ESEM	Environmental scanning electron microscope
F	Fluorophore
FLIM	Fluorescence lifetime imaging microscopy
FRET	Förster resonance energy transfer
HF	Hydrofluoric acid
LED	Light emitting diode
MCP	Multi channel plate
NSET	Nano surface energy transfer
PEG	Polyethylene glycol
PL	Photoluminescence
PMT	Photomultiplier tube
PSi	Porous silicon
Q	Quencher
TCSPC	Time-correlated single photon counting
UV	Ultraviolet

1. INTRODUCTION

Photoluminescence (PL) has emerged as an important tool for studying the optical and electronic properties of solid state materials suited for optoelectronic applications. PL-experiments provide relatively direct information about recombination and relaxation processes. In general, these experiments are useful for the investigation of the electronic properties of the excited state and offer several advantages over other optical techniques. Moreover, PL is the foundation of all light technologies, from lasers to LEDs, detectors and sensors. Tailoring PL becomes very important in nanotechnology; for example, quantum switching is a phenomenon that is based on inhibition or enhancement of PL emission rate. Therefore, interaction of dye-nanostructures and dye-dye molecules have an important potential to be studied as basic research science and engineering applications are concerned.

Silicon has a very special place amongst all in semiconductor technology due to its unique intrinsic properties for device processing as well as being an excellent substrate for silicon and non-silicon appliances. Since the discovery of photoluminescence from porous silicon at room temperature by Canham [1], porous silicon (PSi) nanostructures have been widely used to design silicon-based optoelectronic devices. The surface morphology of the PSi layer can be modified during the electrochemical anodization process by changing the current density, HF concentration, wafer type (n or p), wafer resistivity and illumination light source properties. Obtained PSi network can be a solid-state host matrix for some organic dyes and these dye-PSi composites have an important role in producing laser materials, solar cells and optical waveguides [2, 3]. Although excitation mechanism of the dye-PSi nanocomposites has not yet been clarified, the steady state photoluminescence (PL) intensity and polarization memory studies have been shown that the PL properties of nanocomposites can be explained with an energy transfer mechanism [4].

Recently, it has been demonstrated that the PL intensity of the fluorescent dye molecules embedded in PSi nanostructures depends on the oxidation level of the porous

silicon [5]. When fluorescent dye molecules are attached to freshly etched PSi nanostructure, fluorescence of these molecules is completely quenched due to physical contact between dye and silicon surfaces. After the oxidation process, SiO_2 layer insulates the dye from quenching PSi matrix and consequently turns on fluorescence of the dye [6]; hence, the excitation energy transfer occurs from PSi nanostructures to the dye molecules. The size of the oxidized PSi layer defines the nature of the photonic properties of the material in concern. However, to our knowledge, the dynamics of this fluorescence mechanism of the dye-SiO_2 interaction in a porous silicon nanostructure has not yet been satisfactorily studied in the scientific literature.

Oxidation is an inevitable natural process for porous silicon substrates. The thickness of the oxide layer can be effective on the processing and use of the optoelectronic devices produced from the PSi technology. For example, the photo-conversion efficiency of photodedectors and solar cells strongly depends on the oxidation rate of PSi [7]. Oxidation of the PSi layer improves the electrical performance of sensors, in terms of stability, recovery time, and interference with the relative humidity level [8]. Moreover, optical loss reduction in PSi waveguides depends on the thickness of the oxide layer [9]. Oxidation behavior of the PSi can be analyzed with infrared IR spectroscopy or transmission FTIR spectroscopy [10, 11]. All these techniques measure the thickness of the oxide layer at a single point, preferably, on a flat surface or substrate; whereas here in this work, the depth and the entire topography of the porous silicon oxide layer is obtained with NSET based FLIM technique.

Fluorescence lifetime imaging microscopy (FLIM) is a powerful technique for observation of biological material such as proteins, lipids, nucleic acids and ions in tissue and cell research areas. In contrast to traditional imaging methods based on fluorescence intensity, FLIM provides contrast according to the fluorescence decay time. The fluorescence decay time does not change on intensity variations, and therefore lifetime measurements are not dependent on the local concentration of fluorophores, bleaching, the optical path of the microscope, the local excitation light intensity, or on the local luminescence detection efficiency [12]. Also, the fluorescence decay time for aromatic molecules usually depends usefully on the intrinsic characteristics of the fluorophore

and local environment the local viscosity, pH, or refractive index as well as interactions with other molecules, such as collisional or energy transfer quenching. Therefore, FLIM method has the ability to remotely monitor the local environment of a molecular probe in a manner independent of fluorescence intensity of local concentration [13].

FRET technique is mostly employed in the area of biochemistry, medicine and sensing applications. It is used to study molecular interactions as well as imaging gene expressions inside a living cell [14]. The location of the fluorescent drugs in proteins, DNA, polymers, lipid bilayers can be easily determined through the FRET microscopy method [15]. This powerful technique is also used in photodynamic theory for cancer treatment [16]. Moreover, there are lots of studies in order to detect the protein-protein interactions and to determine kinematics of conformational changes in nucleic acids [17]. For example, strong distance dependence of the FRET efficiency allows construction of highly sensitive sensors. Some of these developed devices are those of pentose and disaccharide accumulation sensors in bacteria, protein, DNA and glucose [18]. The wide-spread and most important application of FRET technique is its use as a spectroscopic ruler. It is possible to measure the distance (from 1 nm up to 10 nm) that separates a donor and an acceptor fluorophore pair in a protein, polyprolines, or in a polymer [19].

Hydrogels play an important role in biomedical applications such as drug delivery systems due to their high water content and low interfacial tension with the surrounding biological environment [20]. Generally, drug gets trapped in the hydrogel during polymerization process. When this hydrogel is immersed in water, release occurs by outflow of drug from the hydrogel and inflow of water to the hydrogel [21]. Because the water uptake value of hydrogel directly depends on crosslink density and conformation of the clusters in the hydrogel network, drug release rate can be modulated by changing these parameters. Hydrogel network used as host in our experiments is a hydrophilic structure, and therefore the distance between the bodipy dye molecules is controllably adjusted without deforming the network. Understanding the displacement of entrapped molecules within the hydrogel matrix due to swelling allows one to probe the stimuli responsiveness of such systems.

This study consists of four chapters. The first chapter provides an introduction to why the time resolved photoluminescence experiments are important in nano-science researches and summarizes the reason behind the interaction between silicon nanostructures and dye molecules; and why hydrogel network is suitable to investigate energy transfer mechanism between two BODIPY dye molecules.

The second chapter of this thesis is devoted to a brief review of the spontaneous emission and the fluorescence lifetime of a dye molecule. Besides single point lifetime measurements, fluorescence lifetime imaging microscopy (FLIM) method is also explained. In addition, this chapter gives some basic information about fluorescence quenching, Nano surface energy transfer (NSET) and Förster resonance energy transfer (FRET) mechanisms.

The third chapter contains three different sections. In the first section, the interaction between BODIPY dye molecule and silicon nanopillars are investigated by means of time-resolved lifetime measurements. Silicon nanopillars are grown by an electrochemical anodization of p-type silicon wafers at low current densities in a hydrofluoric acid solution. Continuous wave (CW), white light and various UV pulsed lasers are employed as illumination sources in sample preparation to study wavelength and coherence effects on the growth mechanism of the nanopillars. Coherence is observed to be the foundation of regularity in obtaining conical shapes. The pillar size is found to be almost linearly proportional to the employed illumination wavelength during their growth. BODIPY dye molecules are chemically attached to these silicon nanopillars and the radiative decay rates are investigated by means of a time-resolved fluorescence experiment. The decay rate of the dye molecules embedded in the vicinity of various size pillar tips is significantly affected due to different apex angles of the conical nature. It is demonstrated that the pillar size and the separation between pillars can be adjusted if one uses a coherent light source with an appropriate wavelength during the course of fabrication process. It is observed that as the pillar size gets smaller, the inhibition in the spontaneous lifetime of BODIPY is more pronounced. In addition, a more regular pillar structure yields non-varying decay rates of the dye molecules throughout the silicon sample. In the second section, the effect of the SiO_2

layer's thickness on the dye-PSi interaction and energy transfer rate are investigated by means of time resolved lifetime measurements. Boradiazaindacene (BODIPY) is used as a fluorescent dye molecule and it is embedded in PSi nanostructure, which is produced by an electrochemical etching of p-type silicon wafer in an HF solution. It is observed that interaction between the dye molecules (donors) and silicon nanostructures (acceptors) is a distance dependent mechanism. When the separation between the silicon nanostructure and BODIPY dye molecule (that is, the thickness of SiO_2 layer) increases, the lifetime of BODIPY dye molecules increases and, hence, the energy transfer rate decreases. This mechanism satisfies the necessary condition for Nano Surface Energy Transfer (NSET) model. The oxide layer's topography of the porous silicon material is therefore easily obtained with the Fluorescence Lifetime Imaging Microscopy (FLIM) measurements together with NSET calculations. In the last section, the fluorescence dynamics of interaction between two BODIPY dye molecules within a chemically cross-linked three dimensional hydrogel network is studied. BODIPY dye molecules are covalently bound to the PEG-based hydrogel two different concentrations; highly concentrated and dilute. When the number of BODIPY azide dye molecules is increased within a cluster of a hydrogel, fluorescence intensity drastically decreases. Moreover, the intensity weighted fluorescence lifetime of the concentrated BODIPY dye molecules increases more than threefold upon exposing the hydrogel structure to water swelling. It is observed that FRET is the predominant mechanism and efficiency of the energy transfer is strongly sensitive to the distance between the donor and acceptor. If the hydrogel is dry, in which the distance between donors and acceptors is minimum, the energy transfer efficiency is found to be about 72%, and the distance between the two dye molecules is calculated to be 4.59 nm. As the separation increases upon hydrogel swelling, the FRET efficiency reduces to 2%, which corresponds to a separation of 10 nm between two bodipy dyes and hence a considerable increase in the level of fluorescence intensity. For the dilute hydrogel samples, the distance between the dye molecules is larger than the critical Förster distance. Therefore, the energy transfer efficiency for this type of dilute samples is found to be much lower.

The last chapter focuses on the brief history of this work, followed with the future promises and recommendations.

2. REVIEW

Spontaneous emission or fluorescence is the process by which an atom in an excited state undergoes a transition to the ground state and the energy difference between the states transfers to a photon or a waveguide mode. There are three different decay mechanisms, which occur under emission of light; radiative, guided and nonradiative [22]. In the radiative decaying process, the excitation energy is converted to a photon, which may escape away from the surrounding body. If the excitation energy is transferred to a photon that is localized inside the body, guided decay rate changes. Finally, nonradiative decay rate becomes effective for those dielectrics which have a complex dielectric permittivity. In which case, excitation energy transforms to the thermal heating as Joule loss.

$$\gamma = \gamma^{R} + \gamma^{NR} + \gamma^{Guided} \tag{2.1}$$

where γ^{R} is the radiative decay rate, γ^{NR} is the nonradiative decay rate and γ^{Guided} is the guided decay rate. In spontaneous emission, a molecule in the excited state can emit a quantum of radiation and undergoes $|2> \rightarrow |1>$ transition. $|2>$ is the excited state and $|1>$ is the ground state. This is due to the coupling of the atomic electron to the electromagnetic field in its vacuum state. Such a spontaneous transition rate is given by Fermi Golden rule. In Equation 2.2, A_{21} is Einstein coefficient and inverse of it is defined as the fluorescence lifetime.

$$A_{21} = \frac{1}{\tau_{21}} = \frac{2\pi}{\hbar^2} \sum_{f} |\langle f|\hat{H}_{ED}|i\rangle|^2 \delta(\omega_f - \omega_i) \tag{2.2}$$

The rate of the spontaneous emission could be altered or controlled by the modification of the electromagnetic vacuum field that leads to inhibition or enhancement in the emission rate properties of molecules. Nonradiative decay rate could be modified by quenching or Förster resonant energy transfer (FRET), whereas the radiative decay

rate is not affected by either quenching or FRET [23]. One way of controlling the radiative decay rate of a spontaneously emitted photon from a dye molecule is to embed it in the vicinity of a dielectric surface. The changes of the chemical (or photonic) environment of the dye molecule can lead to large effects on the fluorescence lifetime.

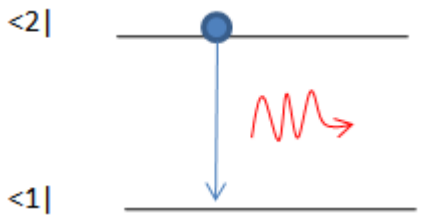

Figure 2.1. The spontaneous emission energy band diagram.

Molecular lifetime and fluorescence yield of an excited molecule strongly depend on the size of the body surrounding it. In the scientific literature, studies on the spectroscopic characteristics of an atom in the vicinity of a body are divided into two parts with respect to its size. If the dimensions of the body are larger than or comparable to the radiation wavelength, the spontaneous emission rate of the atom changes considerably due to resonant modes (whispering gallery modes) [24]. However, in the case of nanobodies, whose dimensions are much smaller than the radiation wavelength, surface curvature and quadruple transitions as well as the plasmon resonances become effective on the spontaneous decaying rates (see Figure 2.2).

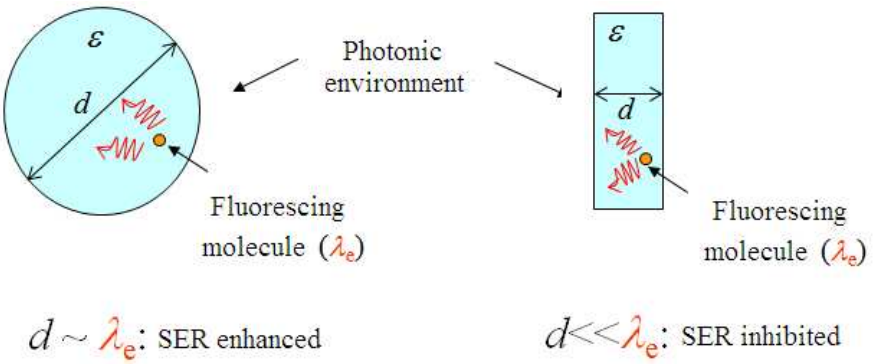

Figure 2.2. The modification of the spontaneous emission rate.

The problem of radiative and nonradiative decay rates of a molecule in the presence of various dielectric nanobodies like spheroidal, cylindrical and pillar has been studied considerably over the past few decades. The most important question about this phenomenon to answer is to find an expressive relationship between the geometrical properties of the dielectric nanobody in concern and the decay rates. Carminati *et al.* [25] has successfully derived an analytical procedure to explain the distance dependence of the radiative and nonradiative decay rates for spheroidal dielectric nanobodies, which demonstrates that the nonradiative decay rate follows an R^{-6} dependence at short range; where R is the distance between the emitter and the center of the nanoparticle. However, the distance dependence of the radiative is more complicated. The radiative decay rate exhibits both R^{-3} and R^{-6} dependencies. The R^{-6} contribution dominates at the plasmon resonance. Dielectric optical nanofibers and carbon nanotubes are important examples of the cylindrical nanocavities. The influence of such a cylindrical geometry is investigated either for an atom being confined inside or planted outside the cavity [26].

The nonradiative decay rate of spontaneous emission of a dye molecule is also affected by quenching or energy transfer mechanisms such as FRET and NSET. FRET involves interaction between the electric fields of the transition dipole of donor and acceptor molecules. As a result of dipole dipole interaction, the excitation energy of the donor molecule is transferred to the acceptor. While the donor molecule is a fluorescent molecule, the acceptor can be a fluorescent molecule or non-fluorescent nanoparticle. Due to energy transfer efficiency depends on the distance between the donor and the acceptor, FRET process could be used as a 'spectroscopic ruler' to determine the distance between two fluorophores. In the nano surface energy transfer (NSET) process, energy transfer flows from a donor molecule to a nanoparticle (NP) surface at a much slower decay rate than the dipole-dipole energy transfer in FRET, with a R^{-4} distance dependence. While NSET is similar to FRET, in that the interaction is dipole-dipole in nature, it is geometrically different from FRET because an acceptor NP has a surface and an isotropic distribution of dipole vectors to accept energy from the donor, leading to a dipole-surface resonance mechanism [27]. The NSET nanoruler represents the next leap forward to monitor structural components within living cell membranes.

2.1. Fluorescence Lifetime or Decay Time

The fluorescence lifetime is defined by the average time a molecule spends in the excited state prior to return to the ground state. Consider a population of $n(0)$ molecules, excited by an impulse at time $t = 0$; the number of molecules remaining in the excited state will decay as

$$\frac{dn}{dt} = -(\gamma_r + \gamma_{nr})n, \tag{2.3}$$

which has a solution of the form,

$$n(t) = n(0)e^{-(\gamma_r+\gamma_{nr})t}, \tag{2.4}$$

where $n(t)$ is the number of molecules in the excited state and $n(0)$ is the initial number of molecules. Equation 2.4 may be rewritten in terms of the fluorescence lifetime, τ, defined as the inverse sum of the decay rates:

$$\tau = (\gamma_r + \gamma_{nr})^{-1} \tag{2.5}$$

$$n(t) = n(0)e^{-t/\tau}. \tag{2.6}$$

In order to show that the lifetime is the average amount of time between the absorbtion and emission of the fluorophore, we must calculate the average time, $< t >$, in the excited state. It can be found by averaging t over the intensity decay of the fluorophore:

$$< t >= \frac{\int_0^\infty tI(t)dt}{\int_0^\infty I(t)dt} = \frac{\int_0^\infty texp(-t/\tau)dt}{\int_0^\infty exp(-t/\tau)dt}. \tag{2.7}$$

The denominator is equal to τ and the numerator is equal to τ^2. Hence the lifetime

equals the average time for a single exponential decay: $< t >= \tau$.

Generally fluorescence lifetime measurements are categorized into either steady-state or time resolved measurements. Steady-state measurements are most commonly performed due to their simplicity and the use of inexpensive equipment, unlike that necessary for more complex time-resolved measurements. Steady-state measurements are performed through the continuous excitation of a sample, followed by recording an excitation or emission spectrum. Therefore, they represent an average of the time resolved phenomena. The sample attains a steady state virtually instantaneously due to the nanosecond time scale of fluorescence. The fluorescence intensity decay of a sample, following a short pulse of excitation light, is measured using time-resolved techniques, typically performed on the nanosecond timescale.

2.1.1. Frequency-domain Fluorescence Lifetime Measurements

The frequency-domain approach utilizes sinusoidal modulation of the excitation light source (obtained from pulsed or modulated laser systems), and lifetimes are determined from the phase shift and demodulation depth of the fluorescence emission signal. The emission occurs at the same frequency as the excitation. Because of the loss of electron energy (Stokes shift) between excitation and emission, the emission waveform is demodulated and phase-shifted in comparison to the excitation. Thus the demodulation ratio (M_E) and phase angle shift (ϕ) constitute two separate observable parameters that are both directly related, via a Fourier transformation, to the initial fluorescence intensity, and lifetime, τ, for a population of fluorophores. In frequency-domain the phase angle shift is described by:

$$tan\phi = w\tau. \tag{2.8}$$

The demodulations of the excitation (M_E) and the emission (M_F) are given by:

$$M_E = (\frac{AC}{DC})_{EX} \tag{2.9}$$

where AC is the average alternate component of the signal that is the value peak to valley of the signal and DC is the average value of direct component of the signal.

$$M_F = (\frac{AC}{DC})_{EM}. \tag{2.10}$$

The relative modulation, M, of the emission is then:

$$M = \frac{(\frac{AC}{DC})_{EM}}{(\frac{AC}{DC})_{EX}}. \tag{2.11}$$

τ can also be determined from M according to the relation:

$$M = \frac{1}{\sqrt{1 + (w\tau)^2}}. \tag{2.12}$$

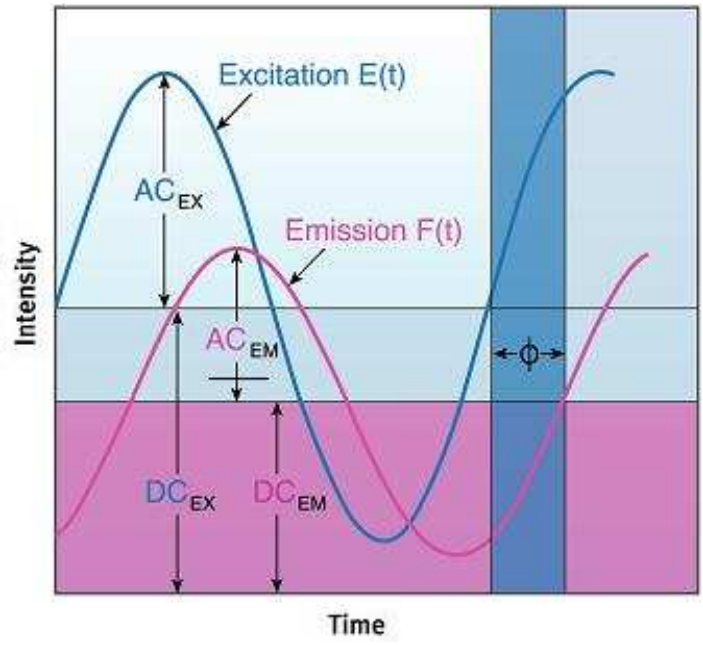

Figure 2.3. The frequency-domain lifetime measurements.

The intensity of the fluorescence is proportional to the amount of the radiation from the excitation source that is absorbed and the quantum yield for fluorescence. The intensity of fluorescence increases with an increase in quantum efficiency, incident power of the excitation source and concentration of the fluorescing species. However, as the fluorescence lifetime is an intrinsic property of the excited state of the fluorophore,

the fluorescence lifetime is independent of the concentration of the fluorescing species and the incident power of the excitation source. The use of fluorescence intensity to provide spatial quantification of samples is severely hampered by effects such as radiation scattering, optical aberrations, inhomogeneous excitation, photon pathlength, collection efficiency and autofluorescence. Therefore, fluorescence lifetime measurements can be a powerful means to provide quantification of samples due to inherent insensitivity to instrumental variations, photobleaching, autofluorescence and scattered light.

2.1.2. Time-domain Fluorescence Lifetime Measurements

In the time-domain method, the sample is illuminated with a short pulse of light and the intensity of the emission versus time is recorded. This usually occurs on the nanosecond time scale. If the decay is a single exponential and the lifetime is long compared to the exciting light, then the lifetime can be determined directly from the slope of the curve. If the lifetime and the excitation pulse width are comparable, some type of deconvolution method must be used to extract the lifetime.

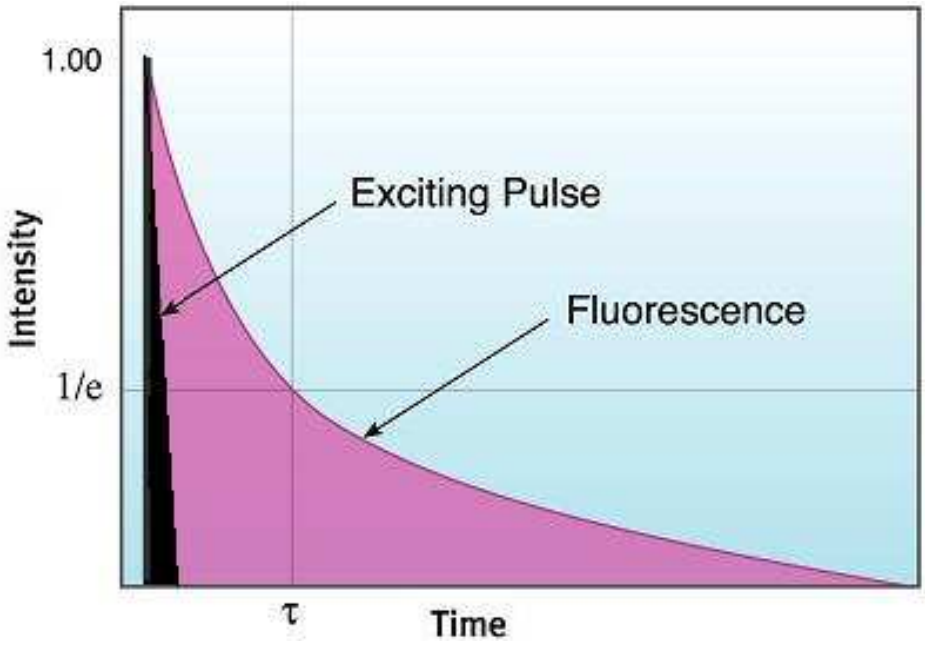

Figure 2.4. The time-domain lifetime measurements.

Time-domain measurements are based on the assumption that, when photons are absorbed, the molecules can be excited in an infinitely brief moment. This idea is commonly known as the delta or δ-pulse. The δ-pulse idea is used to interpret data obtained with real pulsed light sources with measurable pulse-widths. In practice, the time-dependent profile of the light-pulse is reconvolved with the decay-law function. Reconvolution assumes that the δ-pulses are continuous functions, so that the observed decay is the convolution integral of the decays from all δ-pulses initiated during the finite pulse-width.

Very few studies have been undertaken to compare the two methods of lifetime determination. It is indicated that the time-domain method was better suited to measurements made at low intensities, while the frequency-domain method was better when the measured luminescent intensity was high [28]. However, the signal-to-noise ratio (SNR) of the time-domain method was severely limited by saturation of the detector at high intensity values. A more general comparison that focuses on nonimaging applications requires the use of the same detectors so that differences in saturation are not an issue.

2.2. Fluoescence Quantum Yield

The efficiency of fluorescence can be expressed by the fluorescence quantum yield, Φ_F, which is the fraction of excited molecules returning to the ground state by fluorescence

$$\Phi_F = \frac{Number\ of\ photons\ emitted}{Number\ of\ photons\ absorbed}. \tag{2.13}$$

The quantum yield can range from 1, when every molecule in an excited state undergoes fluorescence, to 0 when fluorescence does not occur. The fluorescence quantum yield, Φ_F, can be related to the fluorescence lifetime by

$$\Phi_F = \frac{k_R}{k_F} = k_R \tau_F. \tag{2.14}$$

Therefore the fluorescence lifetime, τ_F (or the fluorescence decay rate k_F), is a measure of the fluorescence quantum yield, Φ_F. The rate constant for the radiative decay processes, k_R, is essentially constant for a particular fluorophore as it is a consequence of the intrinsic electronic properties of the molecule. Therefore the fluorescence lifetime is sensitive to changes in the nonradiative decay pathways. A subsequent increase in nonradiative decay rates will reduce the fluorescence lifetime. These effects make the fluorescence lifetime extremely sensitive to the molecular environment surrounding the fluorophore. Indeed, it is this aspect which has been exploited within this thesis to probe microenvironmental changes such as solvent composition and fluid temperature to investigate and spatially map fluid mixing and temperature within microfluidic devices. Fluorescence techniques can be used to investigate numerous other parameters that affect the microenvironment surrounding a molecule, including viscosity, temperature, polarity, presence of quenchers, pH and pressure.

2.3. Fluorescence Quenching

Fluorescence quenching refers to any process that decreases the fluorescence intensity of a sample. Quenching experiments can be used to determine the accessibility of quencher to a fluorophore [29], monitor conformational changes [30], monitor association reactions of the fluorescence of one of the reactants changes upon binding [31]. Quenching studies may allow isolation of signals from different fluorophores. They may also allow characterization of conformational changes that alter the accessibility of the fluorophore to the quenching agent. In quenching experiments with proteins, the quenching agent may interact with the protein in ways that alter the protein structure or that affect the degree of quenching observed. One method for examining this is the use of several quenchers with different properties. Commonly used quenchers include iodide, which is negatively charged, cesium, which is positively charged, and acrylamide, which is neutral. Cesium is a fairly poor quencher due to its low quenching efficiency. Acrylamide, due to its non-polar character, tends to exhibit static quenching.

There are two basic types of quenching: static and dynamic (collisional). Both types require an interaction between the fluorophore and quencher.

2.3.1. Static Quenching

Static quenching arises when the quencher (Q) forms a stable complex with the fluorophore (F) in the ground state and this complex is inherently non-fluorescent (see Figure 2.5a). After the non-fluorescent complex formation, both the excitation and the emission spectra of fluorophore change. Moreover, static quenching results in reduction in the fluorescence intensity of fluorophore.

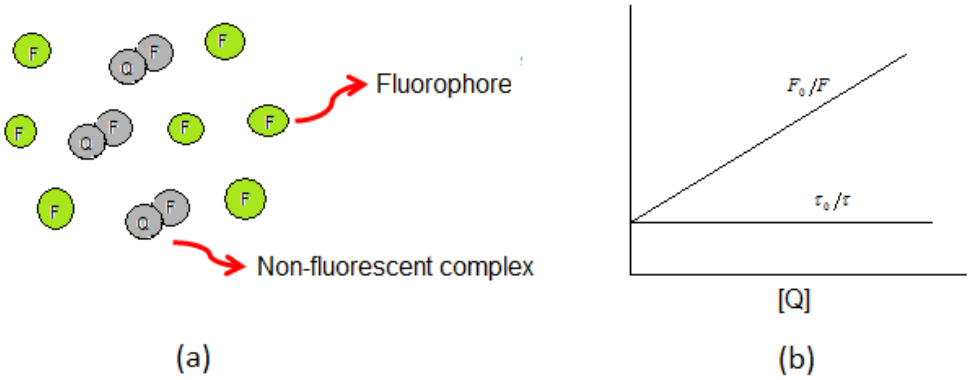

Figure 2.5. In static quenching, (a) Non-fluorescent complex formation, (b) Stern Volmer relation.

In most steady-state fluorescence quenching experiments, data is initially presented in the form of Stern-Volmer plots where the quenching efficiency is related to the total quencher concentration. The Stern-Volmer equation does not contain a variable for the fluorophore concentration and suggests that fluorescence quenching is independent of the fluorophore concentration. The Stern-Volmer relation is given by [32]:

$$\frac{F_0}{F} = 1 + K_S[Q]. \tag{2.15}$$

In Equation 2.15, the quencher concentration is $[Q]$, the Stern-Volmer constant is K_s, F_0 is the measured fluorescence intensity without quencher present, and F is the measured fluorescence intensity with $[Q]$ present. After plotting F_0/F against $[Q]$, the slope can

be determined to give the value of K_s, the Stern-Volmer constant. In Figure 2.5b, it is obvious that there is a linear relation between fluorescence intensity and the quencher concentration. Generally, a more sensitive system will have a steeper slope and, as a result, a higher K_s value. Due to complexation occurs in the ground state between the quenching species and the fluorophore, the fluorescence lifetime of the fluorophore does not change during the static quenching process. Therefore, uncomplexed fluorophores emit normally with the same lifetime and $\tau_0/\tau = 1$.

2.3.2. Dynamic Quenching

In dynamic quenching, quencher diffuses to the fluorophore during the lifetime of the excited state and the fluorophore returns to the ground state without emission of a photon. Most importantly, the dynamic character of the this quenching process was demonstrated by the parallel decrease of the fluorescence intensity and lifetime. Moreover, dynamic quenching mechanism does not affect the absorption spectrum of the fluorophore.

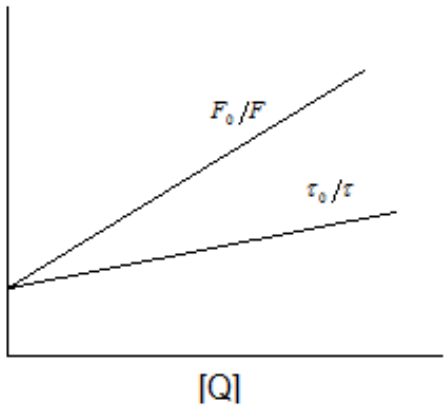

Figure 2.6. The Stern Volmer relation for dynamic quenching.

Dynamic quenching of fluorescence is described by the Stern-Volmer equation [32]:

$$\frac{F_0}{F} = 1 + k_q\tau_0[Q] = 1 + K_D[Q] \tag{2.16}$$

where F_0 and F are the fluorescence intensities in the absence and the presence of quencher, respectively; k_q is the bimolecular quenching constant; τ_0 is the fluorescence lifetime of the fluorophore in the absence of quencher, and $[Q]$ is the concentration of quenchers. When quenching datas are presented as plots of plots F_0/F versus $[Q]$, the slope of obtained line gives the Stern-Volmer quenching constant K_D which depends on the fluorescence lifetime of fluorophore $K_D = k_q\tau_0$ (see Figure 2.6).

2.4. Nano Surface Energy Transfer (NSET)

In the very short distance regime, nonradiative energy transfer from the electronic excited state to the metal or semiconductor plays a very important role in lifetime inhibition or enhancement. The longitudinal coulomb field of the dipole is much stronger than the radiative field at the dipole site, and when this field penetrates nano surface, absorption of the dipole field is high. This nonradiative decay mechanism was apparently first discussed by Kuhn [33].

In NSET model, the energy transfer efficiency depends on the inverse of fourth power of the donor-acceptor separation. Nano surface energy transfer (NSET) technique is based on the model of Persson and Lang which is concerned with the momentum and energy conservation in the dipole-induced formation of electron-hole pairs. The rate of energy transfer can be calculated by performing a Fermi golden rule calculation for an excited-state molecule depopulating with the simultaneous scattering of an electron in the nearby metal or semiconductor to above the Fermi level [34].

In the Persson model [35], the damping rate of the vibration due to excitation of electron-hole pairs in the metal is calculated. The metal conduction electrons are assumed to move in a semi-infinite positive background obtained by smearing out the positive metal-ion cores (see Figure 2.7). The vibration frequency of the dipole Ω assumes that much smaller than the plasma frequency, w_p, of the metal. Since $\Omega << w_p$, the metal conduction electrons can almost respond adiabatically to the slowly varying external field and thus almost adjust to the instantaneous static configuration.

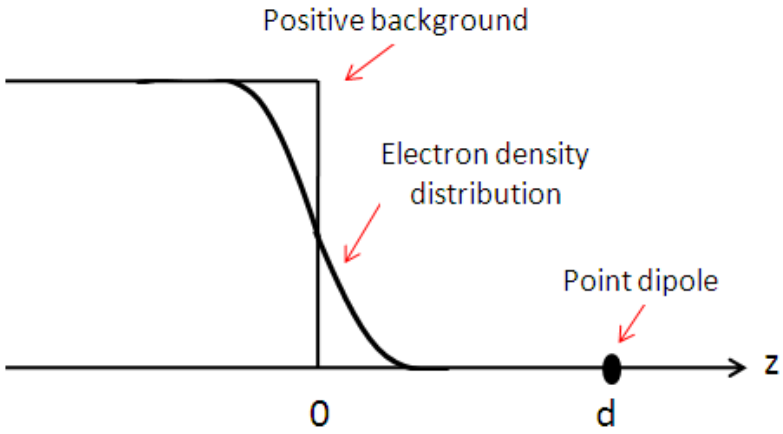

Figure 2.7. Schematic representation of the density distributions.

The damping rate $1/\tau$, the rate at which the vibrationally excited state ($n = 1$) decays to its vibrational ground state ($n = 0$) while an electron is scattered from a level $\vec{k}$ below the Fermi surface ($k < k_F$) to a level $\vec{k}'$ above the Fermi surface ($k' > k_F$), can be obtained from the golden-rule formula:

$$\frac{1}{\tau} = \frac{2\pi}{\hbar} \int d^3k \, d^3k' \, n_k \, (1-n_{k'}) \times | < \vec{k}', n = 0 | H' | \vec{k}, n = 1 > |^2 \times \delta(\epsilon_{k'} - \epsilon_k - \hbar\Omega) \quad (2.17)$$

where

$$H' = e\tilde{\phi}_{dipole}(\vec{x}) \quad (2.18)$$

and

$$n_k = \begin{pmatrix} 1 & if \; k < k_F \\ 0 & if \; k > k_F \end{pmatrix}. \quad (2.19)$$

Persson and Lang derived the energy transfer expression for coupling of the excited-state dipole (donor) to a nano metal surface (acceptor), predicting that the localization of the electric field oscillation at a thin layer leads to an energy transfer distance dependence that follows R^{-4}, where R is the separation distance between donor and acceptor. According to the NSET model, the rate of energy transfer is given

by:

$$k_{NSET} = 0.225 \ \frac{c^3}{w_{dye}^2 w_F k_F d^4} \ \frac{\Phi_{dye}}{\tau_{dye}} \tag{2.20}$$

where c is the speed of light, Φ_{dye} is the quantum yield of the donor dye molecule, w_{dye} is the angular frequency for the donor dye, w_F is the angular Fermi frequency for metal or semiconductor nano surface and k_F is the Fermi wave vector for for metal or semiconductor nano surface. In the NSET model, the characteristics distance length (d_0) is defined as:

$$d_0 = (\frac{0.225 c^3 \Phi_{dye}}{w_{dye}^2 w_F k_F})^{1/4}. \tag{2.21}$$

When the distance between the donor dye and acceptor nanosurface equals to the characteristics distance length (d_0), dye molecules will display equal probabilities for energy transfer and spontaneous emission. The energy transfer rate k_{NSET} can be rewritten using Equation 2.21 and it becomes

$$k_{NSET} = (\frac{1}{\tau_D})(\frac{d_0}{d})^4. \tag{2.22}$$

The efficiency of energy transfer (E) for steady-state PL quenching can be related to the intensity efficiency, $E(I)$

$$E(I) = 1 - (\frac{I'}{I_0}) \tag{2.23}$$

or to the efficiency of energy transfer for quenching of the excited-state donor lifetime $E(\tau)$, and this relationship can be written as:

$$E(\tau) = 1 - (\frac{\tau'}{\tau_0}). \tag{2.24}$$

A generic form of the efficiency of energy transfer allows the distance of separation

between the donor and acceptor (d) and d_0 value to be solved, leading to a power law distance dependence where [36]

$$E = \frac{1}{1 + (\frac{d}{d_0})^4}. \tag{2.25}$$

NSET process is an useful spectroscopic ruler for long distance measurement which will help to understand the large scale conformational dynamics of complex biomolecules in macroscopic detail.

2.5. Fluorescence Lifetime Imaging Microscopy (FLIM)

Fluorescence Lifetime Imaging Microscopy (FLIM) has the advantage of providing two dimensional maps of the fluorescence lifetime with high spatial and temporal resolution. Importantly, FLIM measurements are independent of probe concentration and photobleaching. FLIM also provides the opportunity to study the dynamics of the environment (i.e. "rigidity" or "fluidity") surrounding the fluorophores using time resolved emission anisotropy and can be used to generate information about the kinetics and degree of interaction of cellular constituents on a molecular scale using energy transfer theories.

FLIM is advantageous for complex environments such as tissue because fluorophore lifetimes are independent of fluorescence intensity and thus independent of the effects of absorption and scattering. FLIM microscopy provides a sensitive means of acquiring information about the molecular organization of DNA and RNA. Moreover, FLIM represents a key optical technique for imaging proteins and protein interaction in vivo. FLIM offers a wide variety of genetically expressible fluorescent biosensors, e.g. for the detection of ion concentration, pH, molecular oxygen, proteolytic and chaperone activity, and ubiquitination, many of which can be quantitatively detected by fluorescence lifetime sensing. FLIM technique can be used to measure absolute positions of fluorescent molecules within 100 nm above a metal or semiconductor nano

surface based on distance-dependent fluorescence lifetime modulations.

2.5.1. Widefield and Confocal FLIM

In traditional widefield fluorescence microscopy, the entire specimen is subjected to intense illumination from an incoherent mercury or xenon arc-discharge lamp, and the resulting image of secondary fluorescence emission can be viewed directly in the eyepieces or projected onto the surface of an electronic array detector or traditional film plane. In contrast to this simple concept, the mechanism of image formation in a confocal microscope is fundamentally different. The confocal fluorescence microscope consists of multiple laser excitation sources, a scan head with optical and electronic components, electronic detectors (usually photomultipliers), and a computer for acquisition, processing, analysis, and display of images. Moreover, Confocal microscopy offers several distinct advantages over traditional widefield fluorescence microscopy, including the ability to control depth of field, elimination or reduction of background information away from the focal plane (that leads to image degradation), and the capability to collect serial optical sections from thick specimens. The basic key to the confocal approach is the use of spatial filtering techniques to eliminate out-of-focus light or glare in specimens whose thickness exceeds the dimensions of the focal plane (see Figure 2.8).

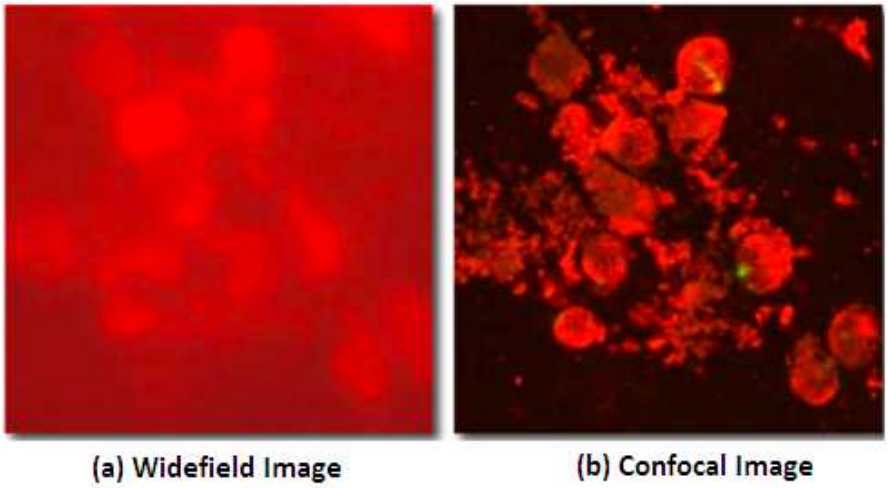

Figure 2.8. Comparison of confocal and widefield microscopy images.

Traditional widefield fluorescence microscope objectives focus a wide cone of illumination over a large volume of the specimen, which is uniformly and simultaneously illuminated (as illustrated in Figure 2.9a). A majority of the fluorescence emission directed back towards the microscope is gathered by the objective (depending upon the numerical aperture) and projected into the eyepieces or detector. The result is a significant amount of signal due to emitted background light and autofluorescence originating from areas above and below the focal plane, which seriously reduces resolution and image contrast. The laser illumination source in confocal microscopy is first expanded to fill the objective rear aperture, and then focused by the lens system to a very small spot at the focal plane (Figure 2.9b).

The size of the illumination point ranges from approximately 0.25 to 0.8 micrometers in diameter (depending upon the objective numerical aperture) and 0.5 to 1.5 micrometers deep at the brightest intensity. Confocal spot size is determined by the microscope design, wavelength of incident laser light, objective characteristics, scanning unit settings, and the specimen. Presented in Figure 2.9 is a comparison between the typical illumination cones of a widefield (Figure 2.9a) and point scanning confocal (Figure 2.9b) microscope at the same numerical aperture. The entire depth of the specimen over a wide area is illuminated by the widefield microscope, while the sample is scanned with a finely focused spot of illumination that is centered in the focal plane in the confocal microscope.

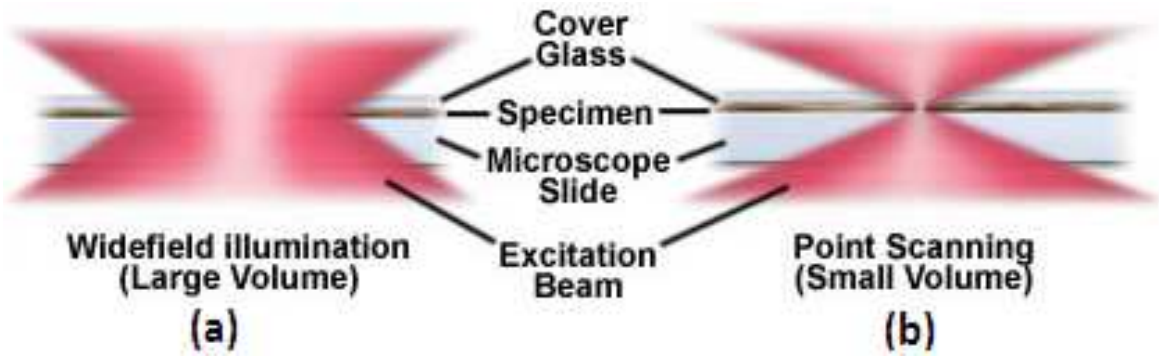

Figure 2.9. Widefield versus confocal point scanning of specimens.

2.5.2. Lateral and Axial Resolution for FLIM Images

The concept of resolution is inseparable from contrast, and is defined as the minimum separation between two points that results in a certain level of contrast between them. In a perfect optical system, resolution is restricted by the numerical aperture of optical components and by the wavelength of light, both incident (excitation) and detected (emission). The influence of noise on the image of two closely spaced small objects can readily affect the quality of resulting images. Confocal microscopy is an established optical imaging technique used to obtain high resolution images of fluorescent specimens. In contrast to conventional methods, confocal fluorescence microscopy affords elimination of emission from out-of-focus fluorescence, and outstanding spatial and depth resolution. This method also allows for three dimensional analysis by optically sectioning the sample.

The intensity distribution of the point spread function in the plane of focus is described by the rotationally symmetric Airy pattern. Because of the cylindrical symmetry of the microscope lenses, the two lateral components (x and y) of the Airy pattern are equivalent, and the pattern represents the lateral intensity distribution as a function of distance from the optical axis. The lateral distance is normalized by the numerical aperture of the system and the wavelength of light, and therefore is dimensionless. Figure 2.10 (airy disk and intensity function) illustrates diagrammatically the formation and characteristics of the Airy disc, the related three-dimensional point spread function, and Airy patterns in the fluorescence microscope. The Airy pattern intensity distribution is the result of Fraunhofer diffraction of light passing through a circular aperture, and in a perfect optical system exhibits a central intensity maximum and higher order maxima separated by regions of zero intensity. The point separation (r) in the image plane is the distance between the central maximum and the first minimum in the Airy disc and its value given by:

$$r_{lateral} = 0.61\frac{\lambda}{NA} \tag{2.26}$$

where λ is the emitted light wavelength and NA is the numerical aperture of the

objective. The low lateral resolution of optical microscopy is caused by the well-known diffraction limit. Objects with features smaller than the volume of the focused light cannot be resolved. Generally, the lateral resolution of an optical microscope cannot exceed 200 nm.

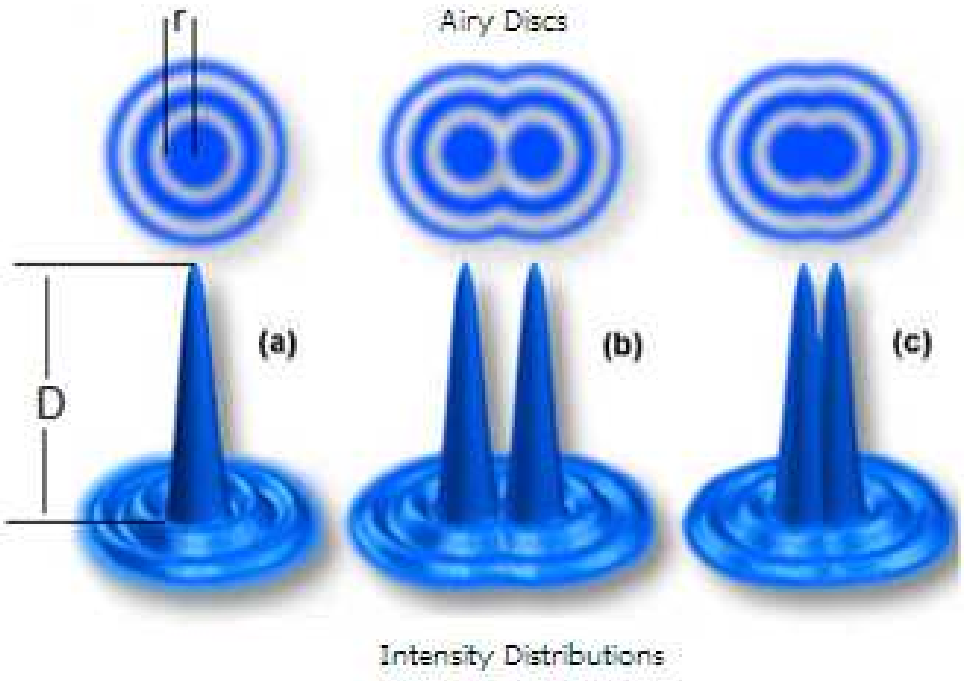

Figure 2.10. (a) Airy discs, lateral and axial resolution, (b) Resolved airy discs, (c) Unresolved airy discs.

The axial (z-axis) resolution is perpendicular to the plane of focus in which the lateral resolution was considered. In the case of lateral resolution, that is, the resolution in the plane of focus, the Rayleigh criterion makes use of the in focus diffraction images (the central cross-section of the 3D diffraction pattern) of two point sources and the minimum distance that they can approach each other laterally, yet still be distinguished as two (see Figure 2.10). Similarly, axial resolution can be defined by the minimum distance that the diffraction images of two points can approach each other along the axis of the microscope, yet still be seen as two. To define this minimum distance, we use again the diffraction image of an infinitely small point object and ask for the location of the first minimum along the axis of the microscope.

Axial resolution is proportional to the wavelength and refractive index of the specimen medium, and inversely proportional to the square of the numerical aperture. Consequently, the numerical aperture of the microscope objective has a much greater effect on axial resolution than does the emission wavelength. Axial resolution (D_{axial}) is given by

$$D_{axial} = 1.4\frac{n\lambda}{NA^2}. \tag{2.27}$$

The axial resolution of a confocal microscope is always worse than its lateral resolution and maximum axial resolution value is about 500 nm.

2.5.3. Pinhole size

Normally, the sample is completely illuminated by the excitation light, so all of the sample is fluorescing at the same time. Of course, the highest intensity of the excitation light is at the focal point of the lens, but nonetheless, the other parts of the sample do get some of this light and they do fluoresce. This contributes to a background haze in the resulting image. Adding a pinhole solves this problem. Because the focal point of the objective lens of the microscope forms an image where the pinhole is, these two points are known as "conjugate points" (or alternatively, the sample plane and the pinhole are conjugate planes). The pinhole is conjugate to the focal point of the lens, thus it is a confocal pinhole.

To understand confocal microscopy it is instructive to imagine a pair of lenses that focuses light from the focal point of one lens to the focal point of the other. This is illustrated by the green rays in Figure 2.11. The blue rays represent light from another point in the specimen, which is not at the focal point of the left-hand-side lens. The colors of the rays are purely for purposes of distinguishing the two setsthey do not represent different wavelengths of light. Clearly, the image of the blue point is not at the same location as the image of the green point. The aim is to see only the image of the green point. Accordingly, if a screen with a pinhole is placed at the other side of the lens system, then all of the light from the dark point will pass through the pinhole.

Note that at the location of the screen the blue point is out of focus. Moreover, most of the light will get blocked by the screen, resulting in an image of the blue point that is significantly attenuated compared to the image of the green point.

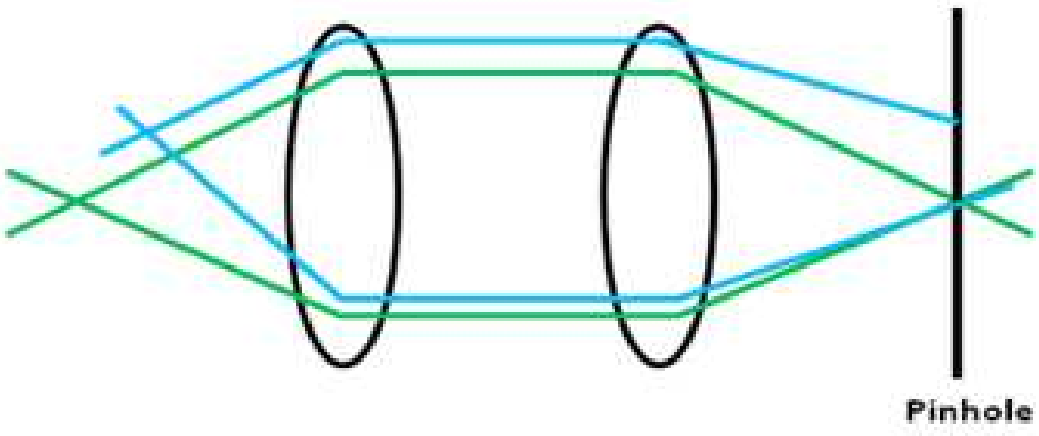

Figure 2.11. Focal plane and pinhole effect.

The size of the confocal pinhole needs to be matched to the size of the Airy disc. The bigger the pinhole, the more photons get through it, but also the less discrimination against scattered light from outside the focal volume. On the other hand, a pinhole smaller than one Airy unit does not improve resolution, it just loses light. The Airy unit can be calculated using Rayleigh criterion:

$$1\ Airy\ unit = 1.22\frac{\lambda}{NA}. \tag{2.28}$$

The diameter of this Airy disc as projected on the pinhole ($D_{pinhole}$) is:

$$D_{pinhole} = \frac{1.22\lambda}{NA}M = 1\ Airy\ unit \times M \tag{2.29}$$

where M is magnification at the pinhole image plane. The parameter $D_{pinhole}$ defines the physical size of one Airy unit in the pinhole image plane.

2.5.4. Statistical Model For FLIM Data

FLIM images represent the decay of fluorescence in time at many different locations in the underlying system. Each location is represented by a pixel x, so that the image may be represented as a matrix

$$\Psi = \left(\begin{array}{c|cccc} & x_1 & x_2 & . \ . \ . & x_n \\ \hline t_1 & \psi(t_1,x_1) & \psi(t_1,x_2) & . \ . \ . & \psi(t_1,x_n) \\ t_2 & \psi(t_2,x_1) & \psi(t_2,x_2) & . \ . \ . & \psi(t_2,x_n) \\ . & . & . & . \ . \ . & . \\ . & . & . & . \ . \ . & . \\ t_m & \psi(t_m,x_1) & \psi(t_m,x_2) & . \ . \ . & \psi(t_m,x_n) \end{array}\right). \tag{2.30}$$

Each column of Ψ represents a fluorescence decay in time at a given pixel x. The decay of fluorescence data in time $\psi(t)$ can often be satisfactorily modeled as a sum of n_{comp} first-order kinetic processes convolved with an instrument response function (IRF) $g(t)$, so that

$$\psi(t) = \sum_{l=1}^{ncomp} c_l a_l = \sum_{l=1}^{ncomp} exp(-t/\tau_l) \star g(t) a_l \tag{2.31}$$

where c_l represents the contribution to the data from process l in time t, a_l represents the amplitude of decay l, and $\star$ is the convolution operator. The model parameters to be fit are then the lifetimes τ_l and their associated linear coefficients a_l representative of intensity. When the same kinetic processes underly the fluorescence at all n locations, Equation 2.31 can be applied globally to the image Ψ, so that

$$\Psi = CE^\top = \sum_{l=1}^{ncomp} c_l a_l^\top = \sum_{l=1}^{ncomp} (exp(-t/\tau_l) \star g(t)) a_l^\top \tag{2.32}$$

where C is a matrix in which column l represents the time-profile of the l^{th} kinetic process, and E is a matrix in which column l represents the intensity of kinetic process l across pixels. Then the parameter estimation task is global analysis: estimation of

the n_{comp} lifetimes τ associated with the image as a whole and the n_{comp} amplitude parameters a_l associated with each pixel (so that $n * n_{comp}$ amplitude parameters are estimated in total). Under least-squares criteria this is

$$min||C(\tau)E^{\top} - \Psi||_{F^2}. \tag{2.33}$$

This is an instance of the multi-exponential analysis problem, which is common in physics applications. Ψ represents the number of photons fluorescing from the location represented by pixel x at time t, and is therefore count data, the noise associated with which is assumed to be Poisson distributed.

2.6. Förster Resonance Energy Transfer (FRET)

Förster Resonance Energy Transfer (FRET) is an important photoprocess in which excitation energy of an excited fluorophore (the donor) is transferred to a light absorbing molecule (the acceptor) without emission of a photon (see Figure 2.12). The most common term "Fluorescence" Energy Transfer is also used for FRET to imply that the acceptor is a fluorophore. Actually this energy transfer is the result of a long range dipole-dipole interaction between donor (D) and acceptor (A). Transfer occurs when the oscillations of an optically induced electronic coherence on the donor are resonant with the electronic energy gap of the acceptor.

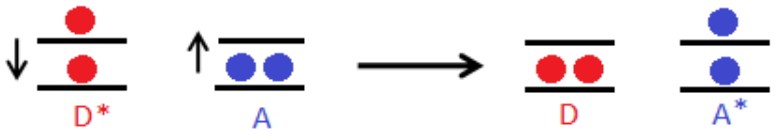

Figure 2.12. Energy transfer mechanism according to Förster.

The rate of nonradiative energy transfer between donor and acceptor molecules strongly depends on the distance between these molecules. Efficiency of FRET is proportional to the inverse sixth power of the intermolecular distance between donor and acceptor pair due to the dipole-dipole coupling mechanism. Apart from separation

distance, the spectral overlap of the donor emission and acceptor absorption spectra, quantum yield of the donor molecule and the transition dipole orientations are important parameters that can alter the rate of energy transfer between donors and acceptors [37].

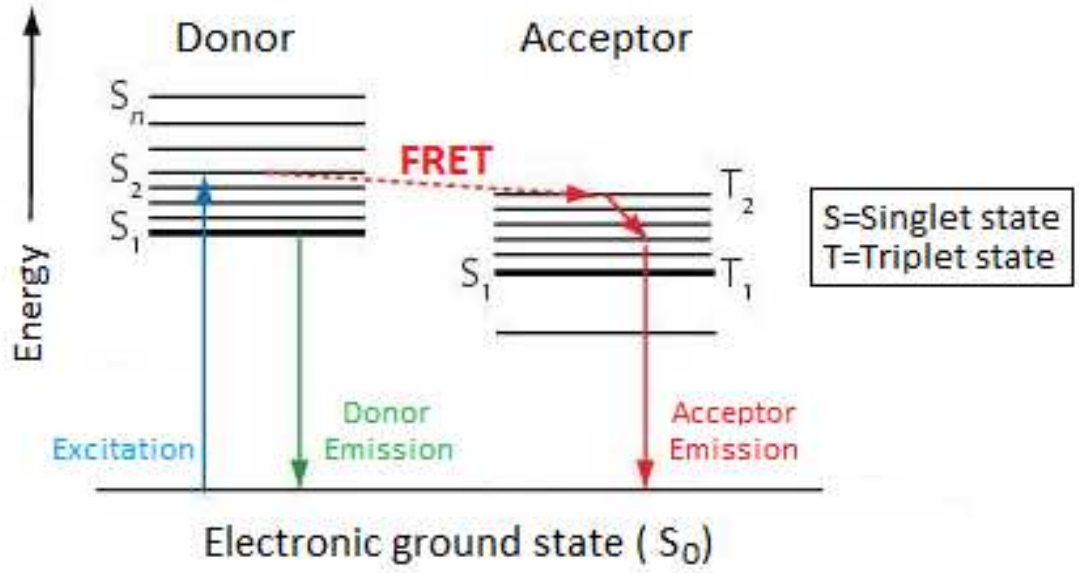

Figure 2.13. Jablonski Diagram for FRET.

2.6.1. Distance Dependence and Critical Förster Distance

The energy transfer rate is a strong function of the separation distance between donor and acceptor. The transfer of energy usually takes place within seperation $D-A$ separations of 1-10 nm. According to the Förster theory, for a fixed separation distance r, the rate of energy transfer from donor to acceptor is given by [38]

$$k_T = \frac{1}{\tau_D}(\frac{R_0}{r})^6 \tag{2.34}$$

where R_0 is the Förster distance and τ_D is the lifetime of the donor in the absence of the acceptor. R_0 represents the distance r where the rate of energy transfer is equal to the rate (probability per unit time) at which the excited donor molecule would decay

from the excited state were the acceptor molecule not present. In other words, when the distance between donor and acceptor equals the R_0 Förster distance, the donor dye molecule transfers half of its energy to the acceptor molecule. The Förster distance (in cm unit) is defined using the spectral properties of the donor and acceptor as:

$$R_0^6 = 8.8 \times 10^{-25}(\kappa^2 n^{-4} \phi_d J) \tag{2.35}$$

where ϕ_d is the quantum yield of the donor in the absence of the acceptor, n is the refractive index of the medium, κ^2 is the orientation factor defined by relative orientation of transition dipoles of the donor and acceptor. J is the overlap integral which represents the degree of the spectral overlap between the donor emission spectrum and the acceptor absorption spectrum.

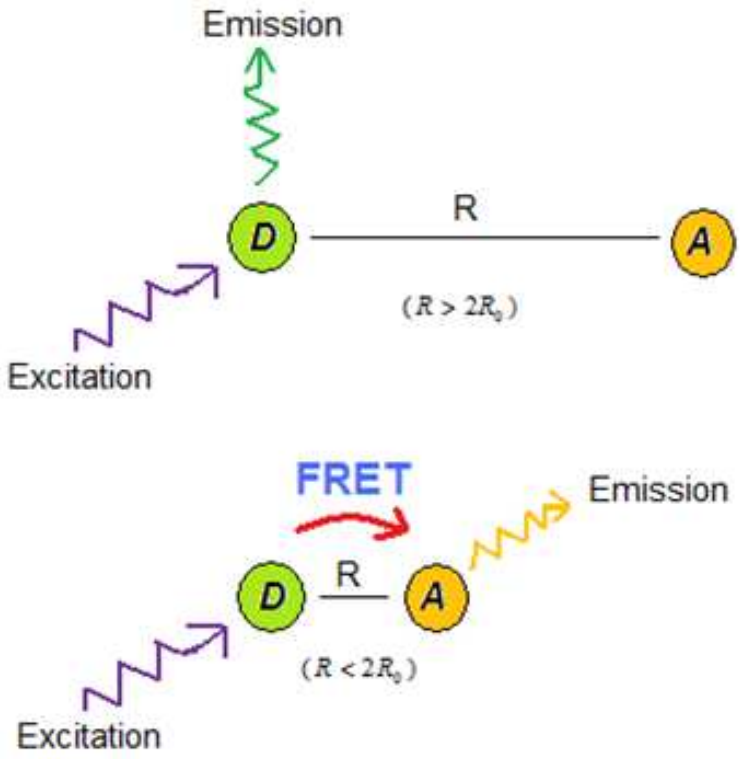

Figure 2.14. The critical Förster distance (R_0).

2.6.2. Spectral Overlap Region

A critical step in the practical application of resonance energy transfer is the calculation of the critical Förster distance value for the donor and acceptor pair. The most important factor in this calculation is the spectral overlap integral $J(\lambda)$. The rate of energy transfer depends upon the extent of the spectral overlap between the donor emission and the acceptor absorption spectra, as illustrated in Figure 2.15. It is crucial to find a compatible pair of fluorophores when doing a FRET experiment, too much spectral overlap may result in crossover and too little overlap will yield low FRET efficiency.

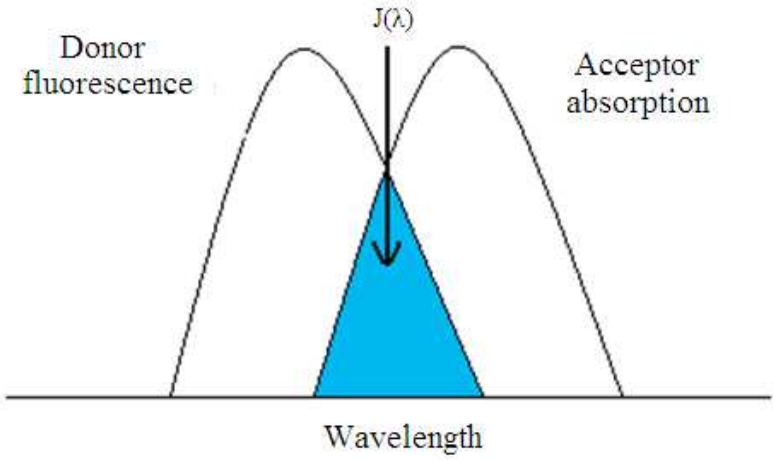

Figure 2.15. Spectral Overlap.

The spectral overlap integral is given by

$$J(\lambda) = \int_0^\infty F_D(\lambda)\varepsilon_A(\lambda)\lambda^4 d\lambda \tag{2.36}$$

where $F_D(\lambda)$ is the normalized fluorescence intensity of the donor and $\varepsilon_A(\lambda)$ is the extinction coefficient of the donor at a given λ wavelength value. $\varepsilon_A(\lambda)$ is the product of the normalized acceptor absorption spectrum with extinction coefficient ε_A which is in general provided by the fluorophore manufacturer.

2.6.3. Dipole Orientation Factor

The orientation factor κ^2 describes the influence of the orientation of the donor's dipole relative to the acceptor's dipole. It is given by:

$$\kappa^2 = (cos\theta_T - 3cos\theta_D cos\theta_A)^2 \tag{2.37}$$

$$\kappa^2 = (sin\theta_D sin\theta_A cos\phi - 2cos\theta_D cos\theta_D)^2. \tag{2.38}$$

In these equations, θ_T is the angle between the emission transition dipole of the donor and the absorption transition dipole of the acceptor θ_D and θ_A are the angles between these dipoles and the vector **r** joining the donor and the acceptor, and ϕ is the angle between the planes. Figure 2.16 illustrates these angles for a given orientation of the donor relative to the acceptor.

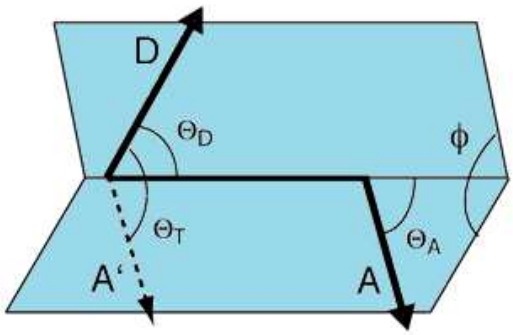

Figure 2.16. Orientation of the donor emission dipole relative to the acceptor excitation dipole.

Depending on this orientation, κ^2 can range from 0 to 4. For parallel transition dipoles in a head to tail arrangement the maximum $\kappa^2 = 4$ is reached, for parallel dipoles $\kappa^2 = 1$ and if the dipoles are perpendicularly oriented to each other $\kappa^2 = 0$ (see Figure 2.17).

κ^2 varies quite a bit for small movements of the donor and the acceptor relative

to each other. Since there are always fluctuations in positions and angles of the D and A molecules, the actual value of κ^2 is an ensemble average or time average. It has been found that the approximation $\kappa^2 = 2/3$ is usually quite satisfactory [39]. If during the excited state lifetime of the donor the orientations of the donor and acceptor can each individually fully reorient randomly, the κ^2 factor is rigorously 2/3. This assumption is widely used in biological experiments, where the fluorophores are theoretically free to rotate, but have in general a fixed distance between them. In most cases, $\kappa^2 = 2/3$ is a good approximation, and there are many examples in the literature where the distances derived are quite reasonable using this approximation.

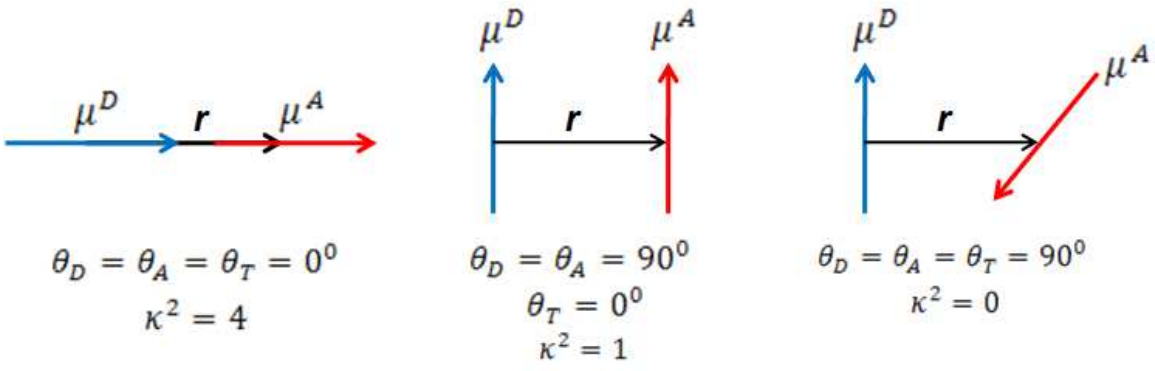

Figure 2.17. Three special cases of orientation factor κ^2.

2.6.4. Fluorescence Resonance Energy Transfer Efficiency

The efficiency of energy transfer (E) is an important parameter for the FRET process. It is defined as the proportion of the photons absorbed by the donor which are transferred to the acceptor.

$$E = \frac{Transferred\ excitation\ to\ the\ acceptor}{Excited\ donor} \tag{2.39}$$

This can be written in terms of rates as:

$$E = \frac{k_T}{\tau_D^{-1} + k_T} \tag{2.40}$$

which is the ratio of transfer rate to the total decay rate of the donor. By substituting k_T from Equation 2.34, FRET efficiency can be written directly in terms of r distance as:

$$E = \frac{R_0^6}{R_0^6 + r^6}. \tag{2.41}$$

This equation shows that the efficiency depends on the distance between the donor and the acceptor as well as on the Förster distance R_0, as shown in Figure 2.18. When the distance between the donor and acceptor equals the R_0 Förster distance, the donor transfers half of its energy to the acceptor and the efficiency E becomes 50%.

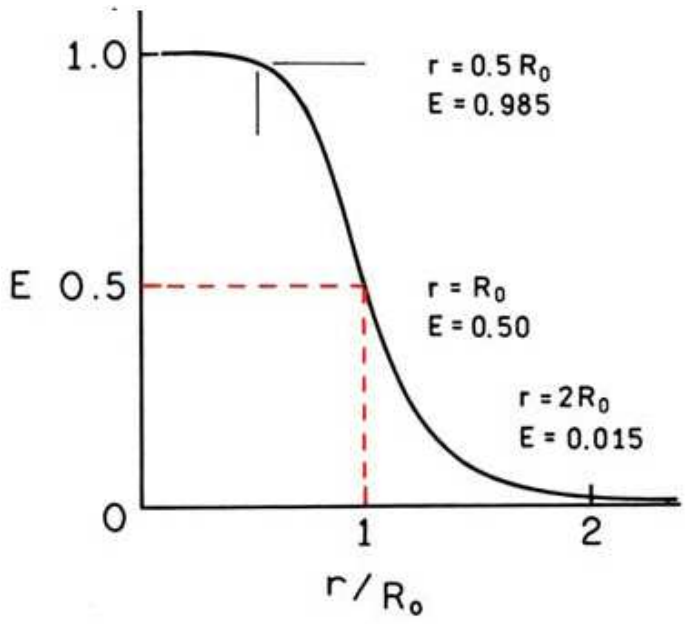

Figure 2.18. Dependence of the FRET efficiency on the distance between the donor and the acceptor.

The efficiency of the energy transfer can also be determined from the time-resolved lifetime measurements. The energy transfer efficiency changes as a function of donor lifetime. Equation 2.42 shows this relation:

$$E = 1 - \frac{\tau_{DA}}{\tau_D} \tag{2.42}$$

where τ is the fluorescence lifetime of the donor in the absence (τ_D) and presence (τ_{DA}) of the acceptor. It can be also calculated in terms of the fluorescence intensities under the same conditions:

$$E = 1 - \frac{F_{DA}}{F_D} \tag{2.43}$$

where F is the fluorescence intensity of the donor in the absence (F_D) and presence (F_{DA}) of the acceptor.

2.6.5. Methods for FRET detection

Every energy transfer event is associated with several characteristic changes in the fluorescence properties of both the donor and the acceptor. Design of a FRET assay depends on what property of the donor or acceptor is being monitored. Rarely is simply the detection of FRET a sufficient yardstick to estimate molecular proximity. There are several quantitative features of this fluorescence phenomenon that affect FRET efficiency, and understanding these features is crucial for a critical examination of FRET data.

When FRET occurs, the donor fluorophore reduces its emission intensity, lifetime of the excited state, and net emission anisotropy. The reduction in lifetime makes it resistant to photobleaching. The reduction in donor intensity, and changes in fluorescence lifetime, emission anisotropy, and photobleaching rates, can be reliable measures of FRET. For an acceptor, FRET increases sensitized acceptor emission and decreases emission anisotropy; measuring donor sensitized acceptor emission and its depolarization are quantitative indicators of FRET [40].

Two main types of determinations of FRET are possible: steady-state and time-resolved measurements. The method used strongly determines the instrumentation required and the information that may be obtained. In general, time-resolved measurements require expensive instrumentation, usually a pulsed laser or a frequency-modulated light source for excitation, a time-correlated photon-counting device or de-

vices capable of monitoring changes in fluorescence decay at the nanosecond time scale, and elaborate software for acquiring data as well as data-fitting modules for calculating the lifetimes and rotational correlation time for time-resolved fluorescence and anisotropy decays.

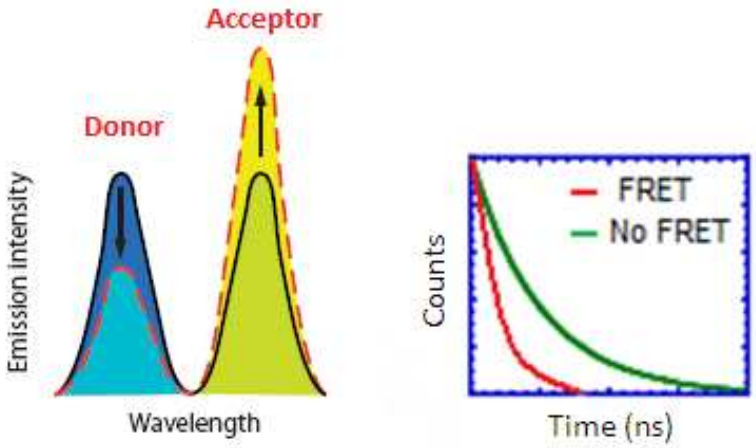

Figure 2.19. The effects of FRET on the donor and acceptor [40].

3. EXPERIMENTAL WORK AND RESULTS

3.1. Preparation of Silicon Nano-pillars and Nano-spheres

In 1990, electrochemical anodization process of silicon wafer in HF based solution is discovered by Canham [1]. It is demonstrated that both photoluminescence and structural properties of silicon-made nanostructures are dramatically affected by various factors of the fabrication parameters, such as HF concentration, current density, etching time and the light source used for illumination [41-43]. Altering the growth parameters, especially changing the properties of the illumination light source, one could manufacture different nanostructures on a silicon wafer such as nanopores, nanospheres, nanorods, conical nanopillars etc. In traditional electrochemical etching process, white light is used as an illumination source and nanopores of random sizes are formed on a silicon wafer [44]. These porous silicon (PSi) samples show an intense red photoluminescence when excited with an ultraviolet optical source. The reason behind this red photoluminescence of the porous silicon surface is explained by quantum confinement [1]. The quantum confinement effects arise when the pores become extensive enough to overlap with each other, generating nanometer scale (typically 10 nm or less) silicon filaments [45]. When the silicon material is sampled of nano meter size, the classical physics rules are no longer valid and quantum physics is needed to explain the behavior of the electrons and holes in silicon material. Because of the fact that the electrons and holes are confined, their motions are quantized in all dimensions. Consequently, energy spectrum turns to a discrete form and the band gap energy E_g increases [46]. The red color of the photoluminescence of the porous silicon is an evidence that the band gap energy level of porous silicon is significantly larger than that of the bulk silicon (1.1 eV). As the size of the nanostructure decreases, the band gap energy increases. Moreover, the confinement of the particles introduces an uncertainty in their momentum due to the Heisenberg's uncertainty relation $\Delta x \Delta p \geq \hbar/2$ [47].

Naddaf *et al.* studied the role of the illumination wavelength during the etching of the porous silicon formation using a halogen lamp. It is found that the PL intensity

of PSi is up to 100 times brighter if the PSi substrate is irradiated with a 450 nm light source; and the PL spectrum is blue-shifted by some 80 nm [47]. On the other hand, it is observed that 700 nm light illumination used in the fabrication process has no effects on subsequent PL spectrum. Only short-wavelength irradiations have a significant effect on the photoluminescence and structural properties of PSi due to their short penetration depth [48].

Employing a coherent light source, whether it is continuous wave (CW) or pulsed, instead of a white light one, results in formation of conical silicon pillars. In a CW laser-induced etching process, surface formation depends on the laser power density. While pore-like structures are formed at low laser power densities, irregular pillar-like structures are obtained at high power densities [49]. In order to obtain regular and sharp conical silicon pillars, the front size of silicon wafer must be illuminated using a coherent pulsed source. Crouch *et al.* observed that laser pulse rate is an effective parameter on the size of silicon pillars. For example, a femtosecond pulsed laser yields formation of smaller silicon pillars than a nanosecond laser [50].

In the first part of this thesis, the effects of coherence and wavelength of illumination light source on the growth mechanism of silicon nano pillars are investigated. PSi samples are prepared by electrochemical anodization of p-type silicon wafers at low current densities in $HF : C_2H_5OH$ (1:1) solutions under illumination of white light, hydrogen laser (Spectra Physics, 337 nm), HeNe laser (633 nm), blue and violet pulsed diode laser head with wavelength 467 nm and 405 nm (LDH-C-D-470, Picoquant, GmbH), respectively. Laser sources with different wavelengths are used to investigate the effects of the wavelength on the PSi growth mechanism. The clean silicon wafers are first cut into pieces and aluminum contacts are coated as thin films at the back of the samples by evaporation in Edwards Coating System, E306A. Copper wires are attached to the aluminum films at the back of the silicon samples by silver paste. The silicon samples then are immersed into $HF : C_2H_5OH$ solution. The copper wire is connected to the positive terminal of the power supply and the stainless steel is connected to the negative terminal as in Figure 3.1. The current is kept constant during anodization. The current density and also the time it takes for creating the best sam-

ples with the most intense photoluminescence is noted and all samples are prepared accordingly.

Several different mechanisms regarding the dissolution chemistry of silicon have been proposed but it is generally accepted that holes are required for both electro polishing and pores formation. The global anodic semi-reaction can be written during pore formation as

$$Si + 6HF \rightarrow H_2SiF_6 + H_2 + 2H^+ + 2e^-. \tag{3.1}$$

The final and stable product for silicon in HF is H_2SiF_6, or some of its ionized forms; it follows that during the pore formation only two of the four available silicon electrons participate in an interface charge transfer while the remaining two undergo a corrosive hydrogen formation.

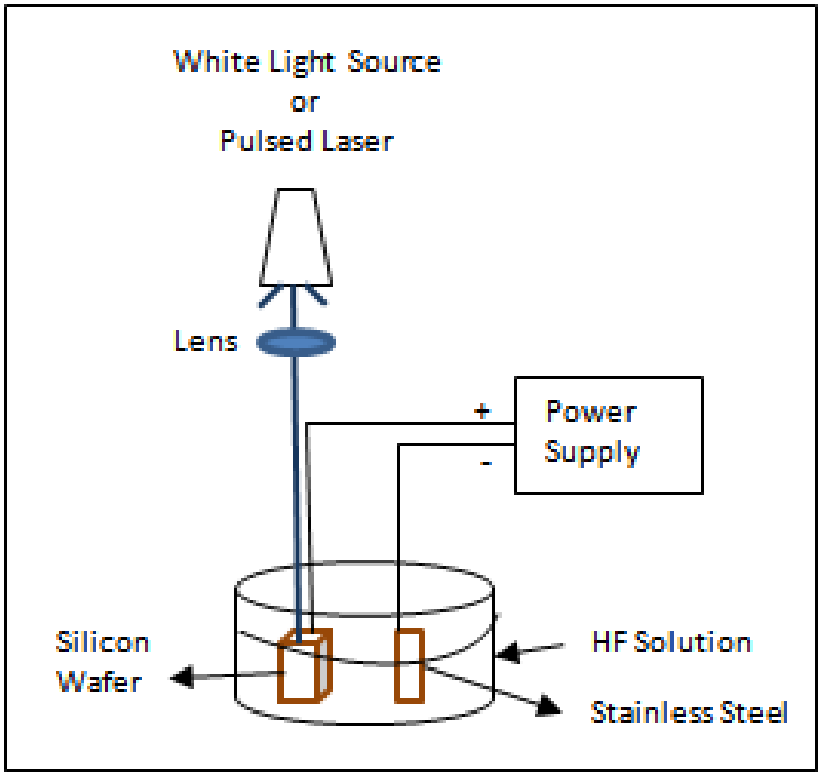

Figure 3.1. The electrochemical anodization setup.

After PSi samples are prepared and the photoluminescence emission of porous silicon is analyzed using a fiber optic spectrometer (USB4000-VIS-NIR Ocean Optics). PSi photoluminescence spectrum is given in Figure 3.2.

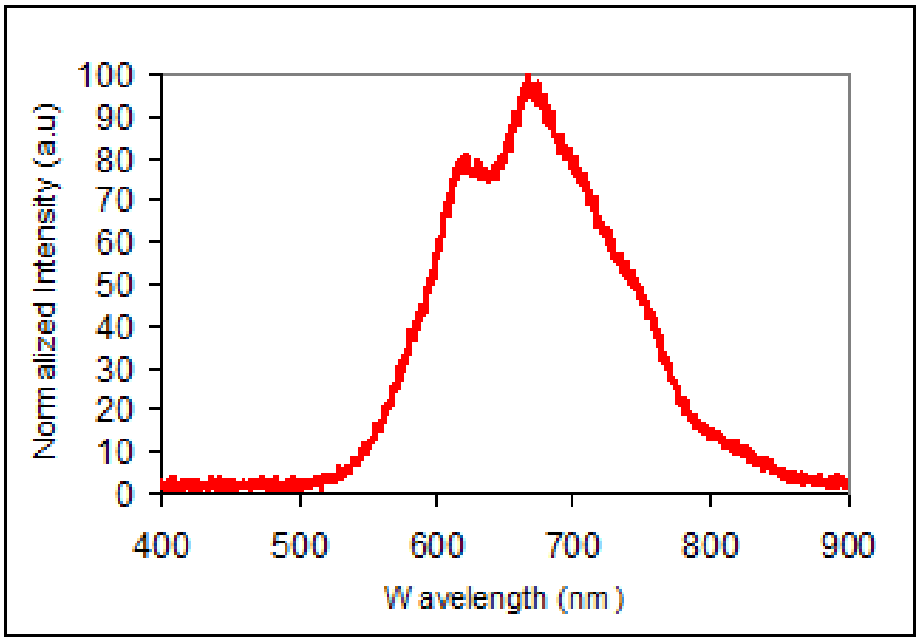

Figure 3.2. The photoluminesce spectrum of porous silicon.

Surface roughness of the PSi samples which are formed under the illumination of various light sources and nano-scale morphology are studied using an environmental scanning electron microscope (ESEM). Figure 3.3 and Figure 3.4 show the surface morphology of the porous layers prepared with the light sources mentioned above. When images are compared, the effect of the laser light on sample formation can be seen directly. Nanopores are observed in silicon wafers under illumination of white light, blue LED and HeNe laser. On the other hand, silicon nanopillars are formed on silicon wafers due to coherence and wavelength effects of different UV pulsed sources.

When silicon wafer is illuminated with white light source during the electrochemical anodization process, nanopores with different sizes are distributed all over the entire etched area as shown in Figure 3.3a. Non-monochromatic and incoherent properties of white light source leads to a surface disorder. Whereas larger and more regular

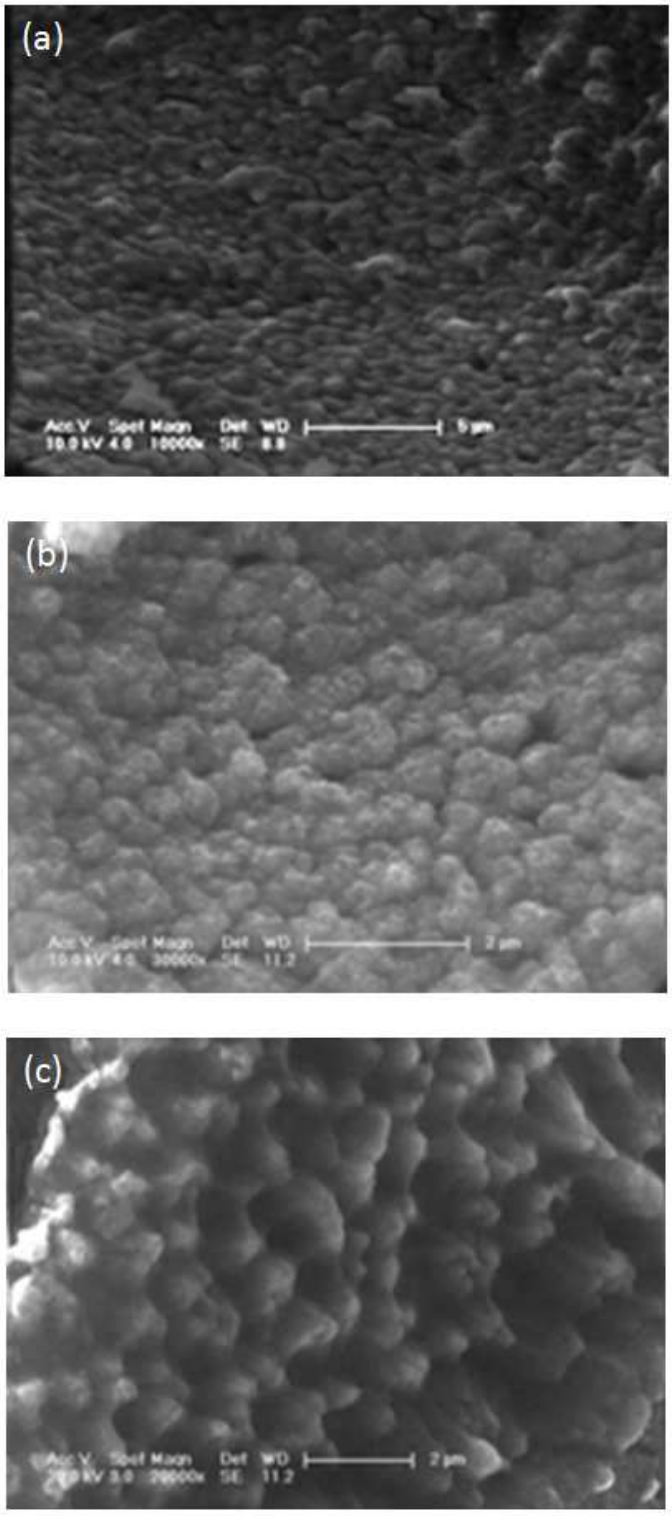

Figure 3.3. SEM pictures of PSi samples produced using various illumination of light sources. (a) White light, (b) Blue LED (450 nm), (c) CW HeNe laser (633 nm) [51].

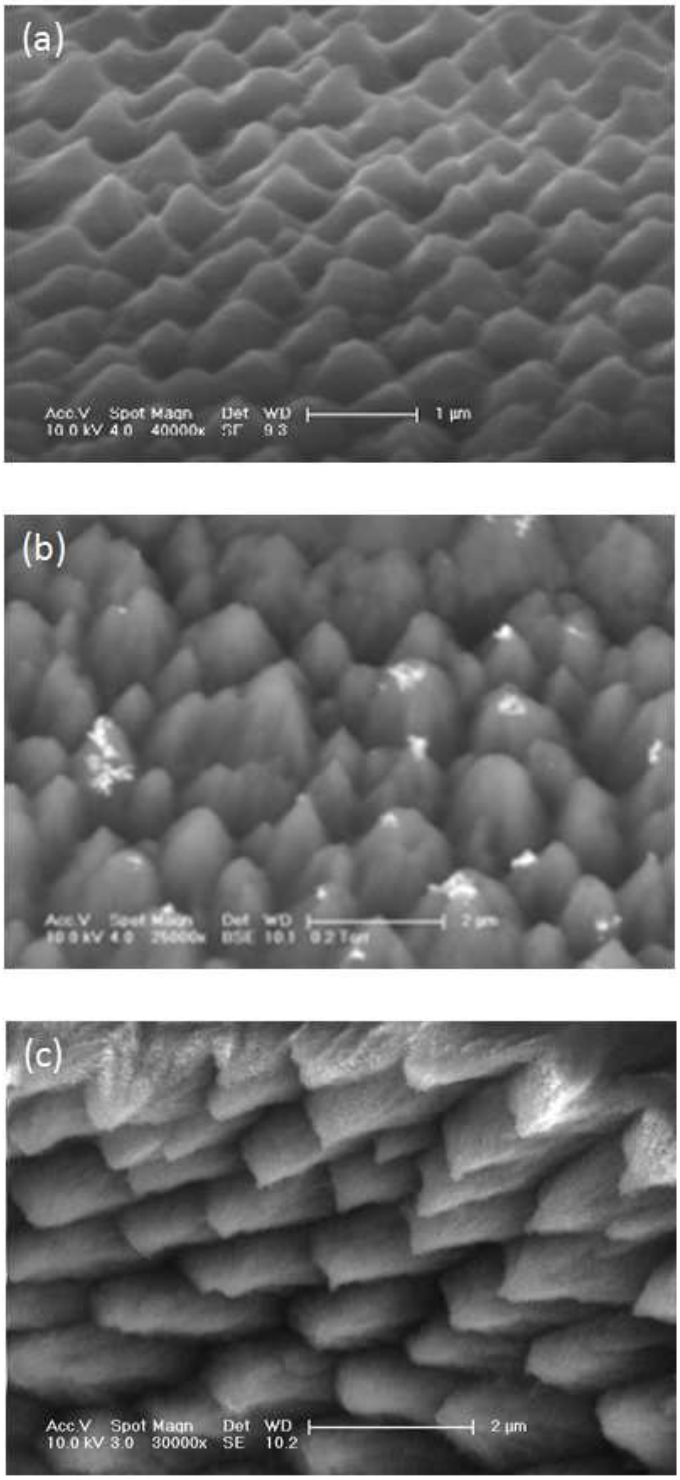

Figure 3.4. SEM pictures of PSi samples produced using various illumination of light sources. (a) Pulsed hydrogen laser (337 nm), (b) Pulsed diode laser (405 nm), and (c) Pulsed diode laser (467 nm) [51].

nanostructures are observed when the silicon wafer is etched under illumination of a CW blue LED of 440 nm in wavelength. This indicates that relatively more regular nanostructures can be obtained using a single wavelength light source instead of using a white light one. In addition to monochromatic property of the light source, if one adds the coherence property, it is observed that the quality of the discreteness of the etched surface morphology is enhanced. For example, Figure 3.3c shows the surface morphology of a silicon wafer etched under coherent 633 nm HeNe laser. It is seen that the individual elements of the nanostructure of the porous silicon surface are more regularly and discretely pronounced but their sizes are being transformed from nano to microstructure due to the relatively longer wavelength of the HeNe laser. However, these discrete micro-structures are not quite regular either, due to the longer wavelength and CW properties of HeNe laser. Figure 3.4a-c show the conical pillars produced with pulsed hydrogen and pulsed diode lasers.

As mentioned above, in Figure 3.3a, only white light is used, therefore, no regular structure is obtained. In Figure 3.3b, the illumination source used in the fabrication process is incoherent but monochoromatic and continuous wave, that is, a blue LED of 440 nm in wavelength; the resultant structure is more regular than the white light one but randomness in the surface morphology of the sample is still the dominant appearance. In Figure 3.3c, the source is both monochromatic and coherent (i.e., HeNe laser), the discreteness in the individual elements of the surface structure is much more pronounced compared to Figure 3.3b; however, as indicated above, the nano-scale size transformed to micro-scale due to relatively longer wavelength of the laser source. Whereas in Figure 3.4a-c, the UV illumination source used is now monochromatic, coherent and pulsed. Thus allowed to obtain quite regular and nice conical pillars. The reason that the pillar sizes are different in three pictures in Figure 3.4a-c is due to different wavelengths of the pulsed sources. As short wavelengths yield smaller pillars, longer wavelengths yield bigger pillars.

To calculate the size of the silicon pillars, a model shown in Figure 3.5 is used: silicon pillars have conical shapes of radius r at depth t from the tip and vertex angle of α. At $t = 100$ nm depth, a relation between α and wavelength of the source used is

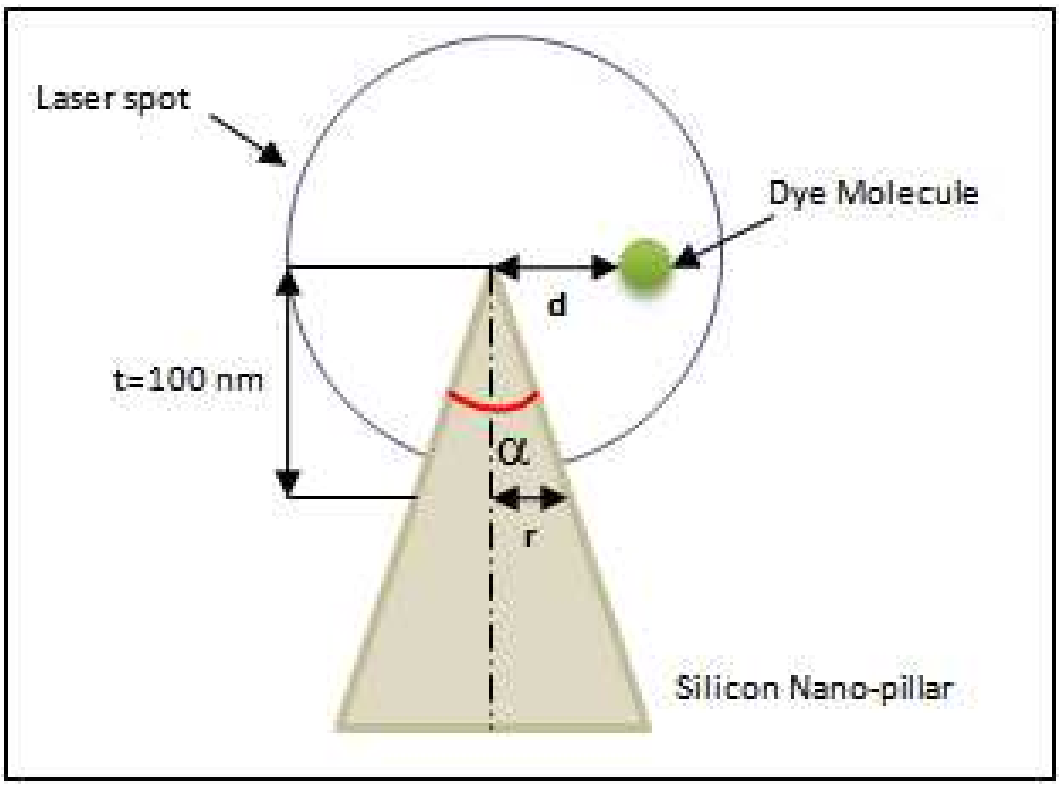

Figure 3.5. Schematic representation of dye molecule attached to a silicon nano-pillar.

found for each sample. Figure 3.6 shows the changes in the tip size and α as a function of illumination wavelength. The radius, therefore, the vertex of the nanopillars changes as a result of illumination wavelength. The exact values for average tip sizes and α angles are summarized in Table 3.1.

Table 3.1. The average tip sizes and α angles for silicon nanopillars.

	Hydrogen Laser (337 nm)	Purple Laser (405 nm)	Blue Laser (467 nm)
Average Tip Size (nm)	213.47±33.11	233.75±52.90	267.78±33.08
α (deg)	46.94±9.40	49.44±14.69	53.24±9.39

Besides illumination light source, resistivity of the silicon wafer is also an important parameter that changes the surface structure of the porous silicon. When the resistivity of the silicon wafer equals to 8-10 Ωcm, regular pillar like nanostructures are formed under the pulsed diode laser illumination. However, an increase in resistivity

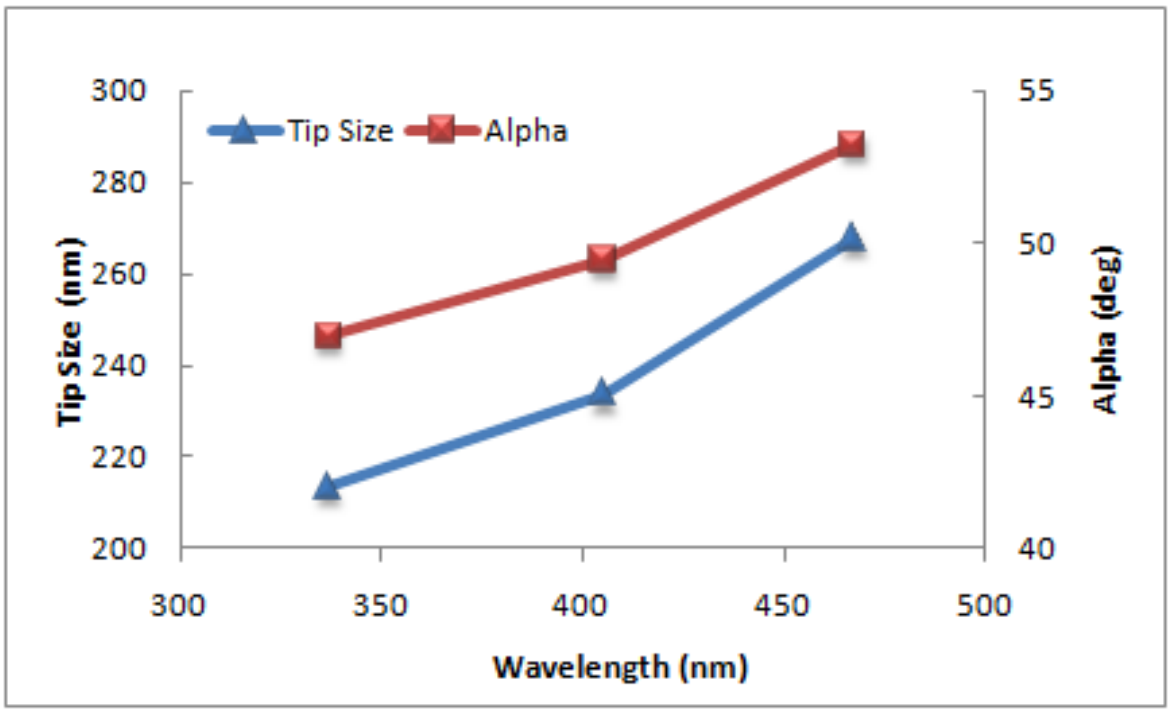

Figure 3.6. The change in the tip size and in vertex of a dye molecule as a function of illumination wavelength.

of silicon wafer leads to microsphere formation on the electrochemically etched surface. The porosity of the samples is examined by scanning electron microscopy (ESEM) and ESEM micrographs of top view of the PSi substrate are given in Figure 3.7. The microspheres, which have diameters between 1 and 15 μm, are clearly observed in the ESEM images. Moreover, there are lots of silicon nanoparticles formed on the surface of each microsphere. Due to the quantum confinement effect of these nanoparticles, PSi substrate exhibits an emission spectrum with a peak at about 680 nm.

The easy fabrication of the pillars and control of the structure with electrochemical anodization parameters make silicon an attractive material, since the samples with different nanostructures have different optoelectronic properties. Moreover, the obtained nanostructures can be used to modify the fluorescence properties of some emitters such as dye molecules. Consequently, they become promising for applications in many fields such as solar cells, nanoscale electronic devices, laser technology, waveguide, chemical and biosensors [52-54].

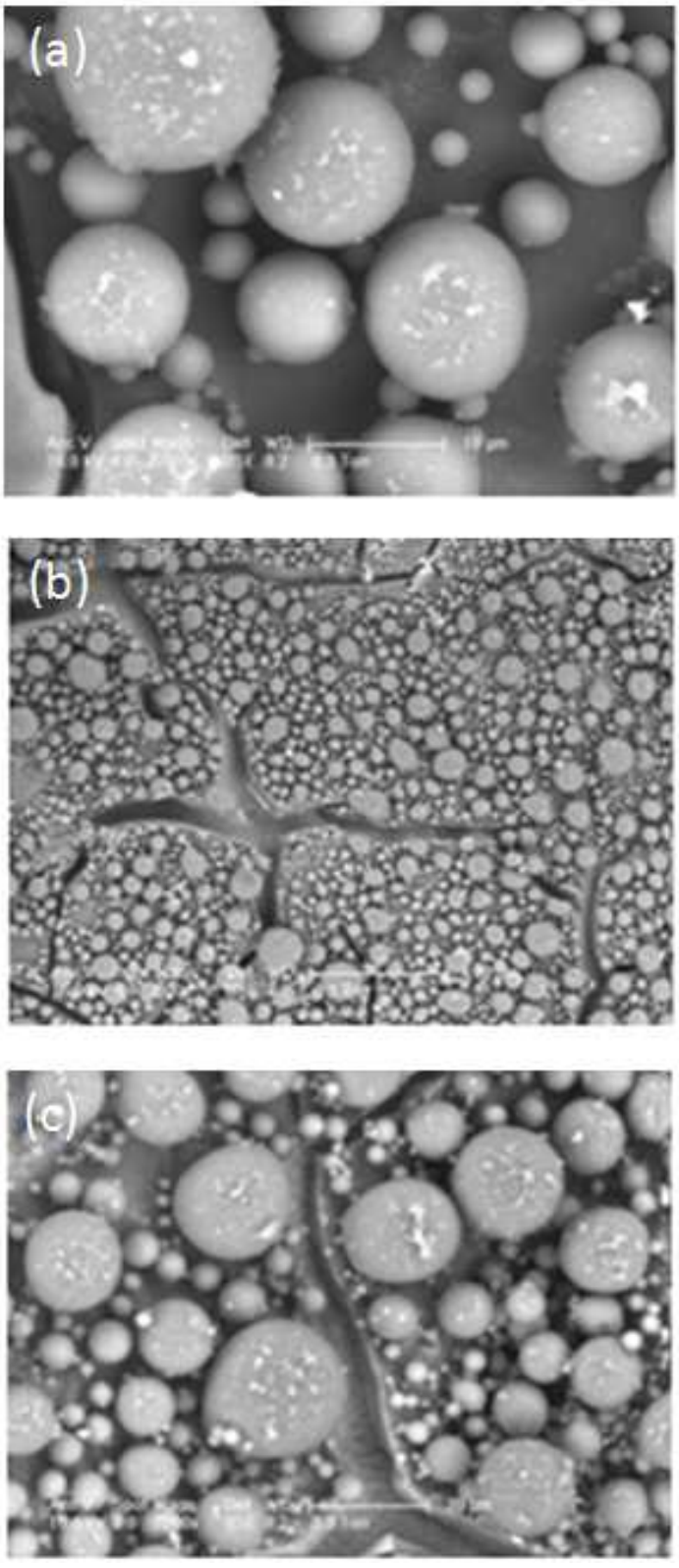

Figure 3.7. ESEM images of porous silicon nanospheres.

3.2. Interaction Between BODIPY Dye and Silicon Nanopillars

3.2.1. BODIPY Dye Attachment to Nanopillars

As the fluorescence dynamics of dye-nanobody is concerned, the rate of spontaneous emission for an atom in the vicinity of nanobodies is either enhanced or inhibited depending on the nanobody structure and the distance of the atom to the nanobody [55]. This is mainly due to the modification of the local electromagnetic field leading to changes in the optical properties of the adsorbed molecule and therefore enhancement or inhibition in the decay rate. In this work, Boradiazaindacene (BODIPY) dye molecules are attached to our silicon pillars and the inhibition of spontaneous emission is observed by time-resolved lifetime measurements. BODIPY is a versatile fluorescence molecule widely used in imaging applications due to its smooth and almost location-fixed excitation and emission spectra contributing to overall brightness, which is superior to those of many fluorophores with its high quantum yield, often approaching over 90% in various solvents.

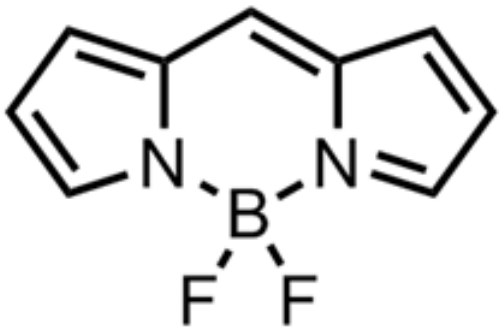

Figure 3.8. The chemical structure of BODIPY dye.

Dye attachment to the PSi surfaces were carried out as follows. First, 4,4-difluoro-1,3,5,7-tetramethyl-8-[(10-bromo)]-4-bora-3a,4a-diaza-s-indacene, a bromo derivative of the BODIPY dye was synthesized according to previously reported literature [56]. Thereafter, this dye was covalently immobilized onto the surface by first treating the surface with a solution of 3-aminopropyltri(methoxy)silane in dry toluene (0.2 mL/10

mL) at room temperature, followed by heating thus modified surface in a solution of BODIPY-Br in N-methylpyrrolidone (2 mg/10 mL) at 60 °C for 20 h. Surfaces were extensively washed with dichloromethane to remove any residual unbound dye molecules. The penetration of the dye molecules is studied by spectroscopy and the results show that the dried dye uniformly covers the pore walls. The fluorescence emission spectrum of BODIPY dye molecules on PSi surface is given in Figure 3.9.

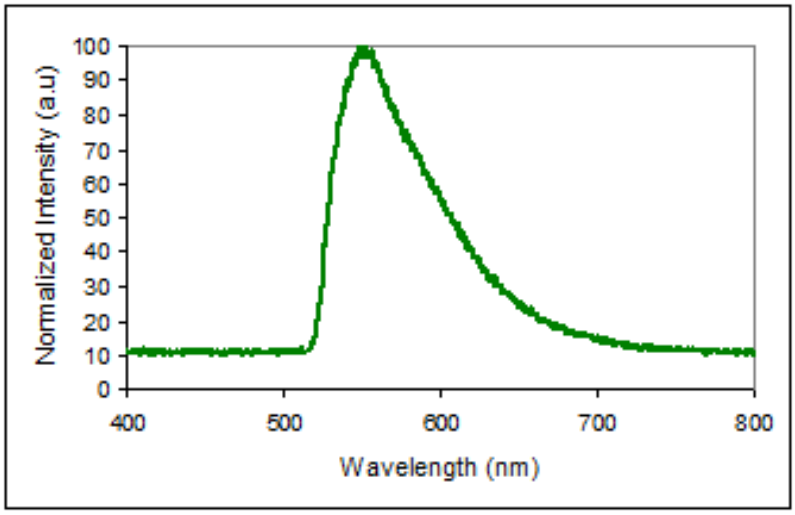

Figure 3.9. The fluorecence emission spectrum of the BODIPY dye on PSi.

3.2.2. Time correlated single photon counting (TCSPC)

The time-resolved fluorescence lifetime of the BODIPY dye molecule is performed using the Timeharp 200 PC-Board system (PicoQuant). The measurement of the fluorescence lifetime is based on the time correlated single photon counting (TCSPC) method. Time-Correlated Single Photon Counting (TCSPC) is based on the detection of single photons of a periodical light signal, the measurement of the detection times of the individual photons and the reconstruction of the waveform from the individual time measurements. The method is based on the repetitive precisely timed registration of single photons of a fluorescence signal. The reference for the timing is the corresponding excitation pulse. As a single photon sensitive detector, a Photomultiplier Tube (PMT), Multi Channel Plate (MCP) or a Single Photon Avalanche Photodiode (SPAD) can be

used. Provided that the probability of registering more than one photon per cycle is low, the histogram of photon arrivals per time bin represents the time decay one would have obtained from a single shot time-resolved analog recording. The precondition of single photon probability can be met by simply attenuating the light level at the sample if necessary. If the single photon probability condition is met, there will actually be no photons at all in many cycles. The diagrams below illustrate how the histogram is formed over multiple cycles.

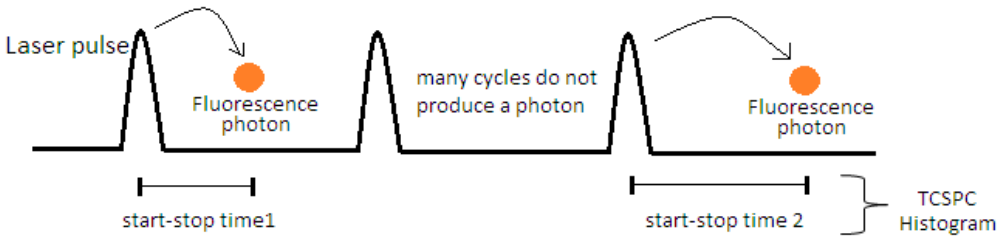

Figure 3.10. Principle of classic time-correlated single-photon counting.

The histogram is collected in a block of memory, where one memory cell holds the photon counts for one corresponding time bin. These time bins are often referred to as time channels. In practice the registration of one photon involves the following steps: first the time difference between the photon event and the corresponding excitation pulse must be measured. For this purpose both signals are converted to electric signals. For the fluorescence photon this is done via the single photon detector mentioned before. For the excitation pulse it may be done via another detector if there is no electrical sync signal supplied by the laser. Obviously all conversion to electrical pulses must preserve the precise timing of the signals as accurately as possible. The actual time difference measurement is done by means of fast electronics which provide a digital timing result. This digital timing result is then used to address the histogram memory so that each possible timing value corresponds to one memory cell or histogram channel. Finally the addressed histogram cell is incremented. All steps are carried out by fast electronics so that the processing time required for each photon event is as short as possible. When sufficient counts have been collected the histogram memory can be read out. The histogram data can then be used for display and, for example, fluorescence lifetime calculation.

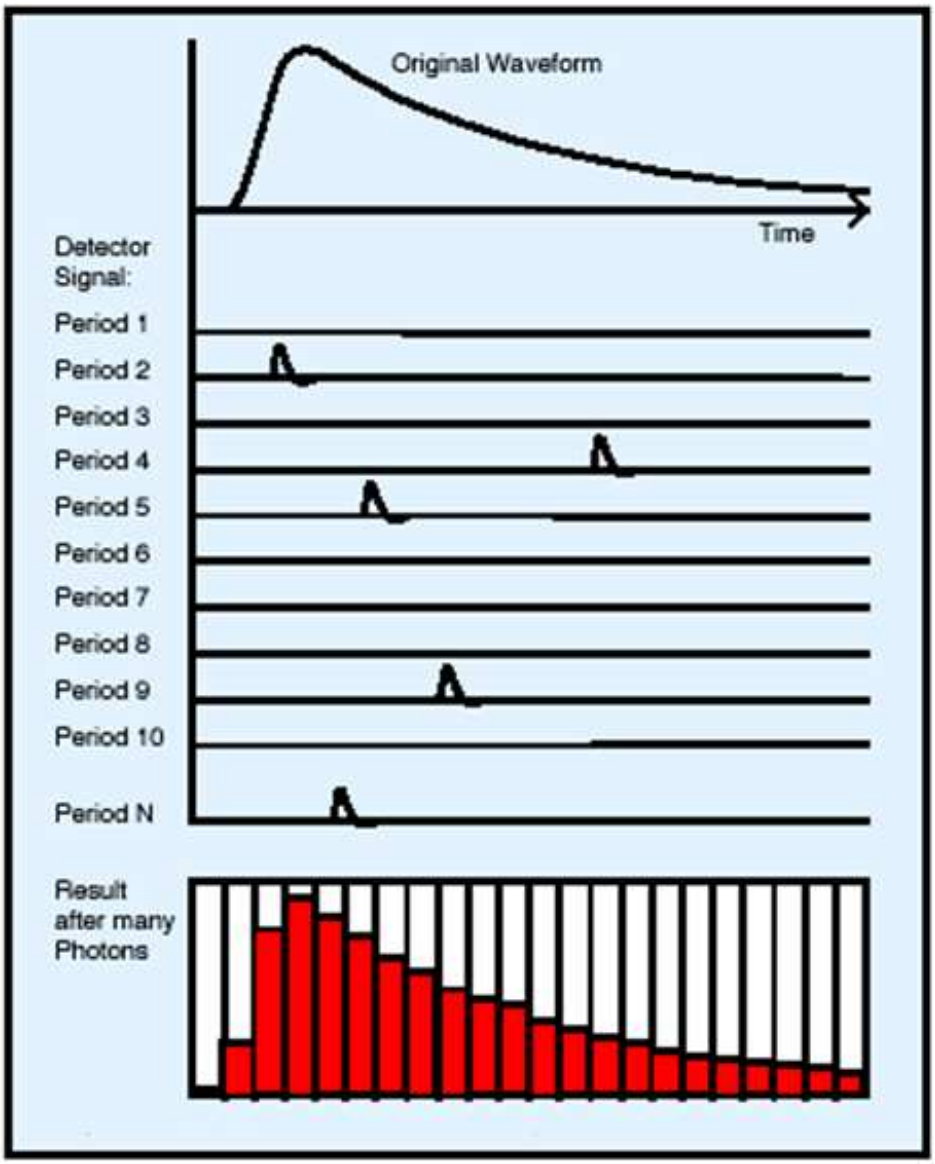

Figure 3.11. The fluorescence lifetime histogram.

For multi-exponential fluorescence decay fitting, FluoFit 4.2 computer program (Picoquant, GmbH) is used. The fluorescence intensity decays is recovered from the frequency-domain data in terms of a multi exponential model,

$$I(t) = \sum_{i=1}^{n} A_i exp(-t/\tau_i) \tag{3.2}$$

where A_i is the amplitude of each component and τ_i is its lifetime. The fractional

contribution of each component to the steady-state intensity is described by

$$f_i = \frac{A_i \tau_i}{\sum_j A_j \tau_j}. \tag{3.3}$$

The intensity weighted average lifetime is represented as

$$\langle \tau \rangle = \sum_i f_i \tau_i \tag{3.4}$$

and the amplitude-weighted lifetime is given by

$$\bar{\tau} = \frac{\sum_i A_i \tau_i}{\sum_i A_i}. \tag{3.5}$$

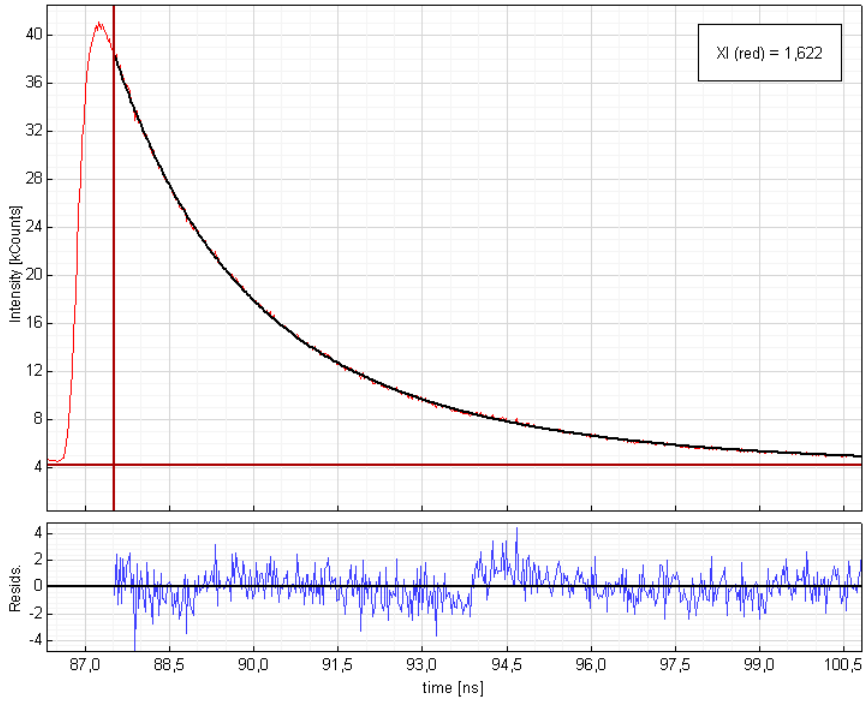

Figure 3.12. Decay fitting and calculation of decay parameters of BODIPY dye on silicon wafer.

Figure 3.13 shows the optic experimental setup. The excitation source used in the experiment is an ultraviolet pulsed diode laser head with a wavelength of 405 nm (LDH-C-D-470 Picoquant, GmbH). The separation of the fluorescence emission and the excitation occurs at a dichroic mirror. The excitation light is focused onto the sample

using a microscope objective of 0.55 numerical aperture with a working distance of 10.1 mm (Nikon, ELWD 100X).

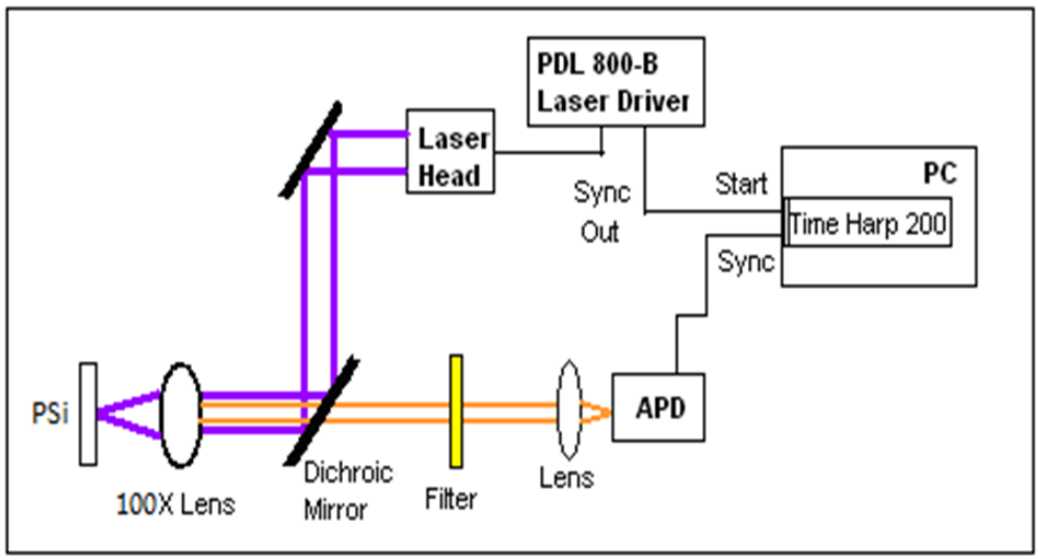

Figure 3.13. Optical setup.

3.2.3. Single Point Lifetime Measurements

The spontaneous emission of an emitter is not an intrinsic property of the emitter and it is strongly affected by the surrounding environment. Therefore, the decay lifetime of an emitter in the vicinity of a nanostructure is inhibited or enhanced. Such structure may be, for example, a flat surface [57], a nanosphere [58], a nanorod [58] or a nanoparticle [59]. Understanding and controlling the emission properties of molecules in nanostructured geometries has a great potential for applications in the area of nano optics, biochemistry and molecular biology [60].

Silicon samples shown in Figure 3.3 and Figure 3.4 are impregnated by BODIPY dye molecules and the attached dye molecule is at a distance of d, which is a fixed distance in our experiments. Pillars grown are seen to be away from each other in the range of 1-2 μm for various wavelengths we used during the production. Since our laser excitation spot-size is about 0.8 μm, one can attach dyes or quantum dots only

to the tips of the pillars and the inhibition will be due to the tip only without in situ monitoring. Apart from the conical tip of the pillars, the spontaneous emission rate (or lifetime τ) is mainly due to the tip and does not vary from its value in the atmosphere for other parts of the pillars. In other words, as one goes from the tip to the bottom of the pillar, the structure gets much thicker, which does not cause any inhibition in BODIPY's rate of the spontaneous emission. The fluorescence lifetime of BODIPY dye molecules attached to silicon nanostructures and in free space are compared. Decay parameters are determined using the double exponential tailfit model, and the best fits are obtained by minimizing χ^2 values (see Figure 3.12). For free space lifetime of dye molecule, a silicon wafer is impregnated by BODIPY dye molecule and its lifetime is measured as 4.5 ns.

Table 3.2. The Fluorescence Lifetimes of BODIPY Dye Molecules in all Samples.

White Light Illuminated $< \tau > (ns)$	Hydrogen Laser Illuminated $< \tau > (ns)$	Blue Laser Illuminated $< \tau > (ns)$
2.55	2.66	3.50
2.66	2.77	3.57
2.88	2.79	3.59
3.55	2.82	3.62
3.70	2.86	3.65

In this work, we have seen that the decay rates of the dye molecules interacting with their surroundings are substantially different than those of free dye molecules. When BODIPY dye molecules are embedded in porous silicon, which is formed under white light illumination, the lifetime of the molecules is inhibited, however, it varies between 2.55 and 3.70 ns due to an irregular surface morphology. On the other hand, the lifetime values in the case of pulsed diode laser assisted samples are also inhibited but the variation is found to be insignificant due to regularly shaped nanopillars. The decay lifetimes of BODIPY calculated from five different positions in all samples are

given in Table 3.2. It is observed that the decay rate of the dye molecules decreases as the illumination wavelength increases since the illumination wavelength is almost linearly proportional to the size of the grown structure. While the lifetime for hydrogen laser illuminated sample is 2.80 ns, this value is 3.61 ns for a pulsed blue laser illuminated sample shown in Figure 3.4.

Our experimental results show that one can control inhibition in the spontaneous emission rate by adjusting the nanopillar size through the fabrication parameters. In addition, no in situ imaging mechanism is needed to monitor a single tip of the nanostructure since the separation distance between the nanopillars is much greater than the spot-size of the excitation source, which is interrogated in a confocal time-resolved setup.

3.3. Interaction Between BODIPY Dye and Silicon Nanospheres

3.3.1. Fluorescence Dynamics of BODIPY Embedded in Silicon Nanospheres by FLIM Technique

The fluorescence lifetime of a dye molecule on the nano structured surface such as nanopillar or nanospheres strongly depends on the surface topography. Therefore, single point lifetime measurement cannot be sufficient to explain the interaction between the dye molecules and nanostructures. To obtain individual lifetime values on the silicon nanostructures and to construct surface lifetime map of these nano surfaces, Fluorescence Lifetime Imaging Microscopy (FLIM) technique can be used. FLIM is a technique to map the spatial distribution of lifetimes within microscopic images and it allows measurements in living cells as well as in fixed materials. Moreover, FLIM is a very efficient way of monitoring in situ physical, chemical, biological phenomena as well as various kinds of surface topographies.

The optical setup for the confocal FLIM measurements is given in Figure 3.14. The excitation source used in the experiment is an ultraviolet pulsed diode laser head with a wavelength of 467 nm (LDH-C-D-470 Picoquant, GmbH). To obtain a Gaussian

beam illumination, a single mode optical fiber is used as a waveguide (Thorlabs, S405-HP). The excitation light is focused onto the sample using a microscope objective of 0.55 numerical apertures with a working distance of 10.1 mm (Nikon, ELWD 100X). A pinhole, which has a diameter 75 μm, is placed in the focal plane, in order to increase the resolution of the FLIM images. In the confocal FLIM setup, a xy piezo scanner from Piezosystem Jena, which allows a scan range of 100×100 μm^2 (NV40-3CLE), and SCX 200 (Picoquant, GmbH) fluorescence lifetime imaging controller are used for PSi surface scanning. Fluorescence lifetimes are calculated pixel-by-pixel using SymPho Time software (Picoquant, GmbH).

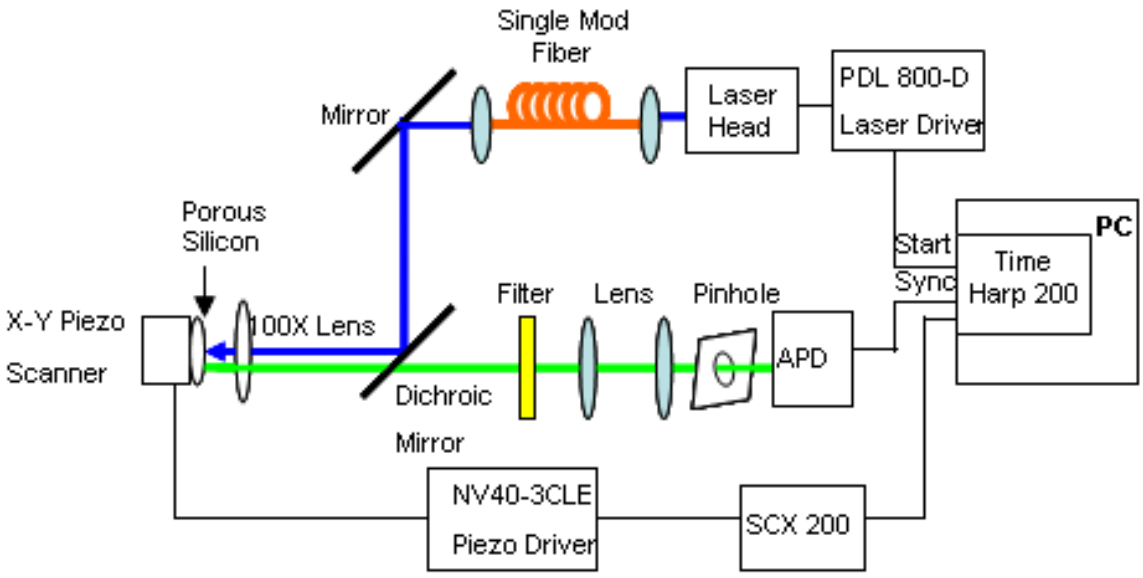

Figure 3.14. Optical FLIM setup.

To obtain surface lifetime map of dye molecules on the silicon nano surfaces, PSi substrate is impregnated with BODIPY dye molecules. After the dye impregnation, PSi emission disappears and only the emission spectrum of BODIPY dye at 540 nm is observed. To compare the fluorescence dynamics of BODIPY dye in the PSi with the respective dynamics on nonporous silicon surface and to calculate energy transfer efficiency rate, the same BODIPY solution is also deposed on bulk silicon wafer as a thin film. While the fluorescence lifetime of the BODIPY on nonporous silicon wafer is measured as 4.94 ns, lifetime of the same dye molecules on PSi structure is

measured to be 1.35 ns. The reason behind the quenching of PSi photoluminescence and the enhancement of the fluorescence lifetime of BODIPY is thought to be the energy transfer mechanism from BODIPY dye molecules to Si nanoparticles.

The surface of PSi substrate is periodically scanned in the xy directions for 2 months and FLIM images are analyzed with the SymPho Time software program. It is observed that the decay parameter of BODIPY dyes is independent of the size of the microspheres. In addition, we investigated that the average lifetime and fluorescence intensity of the dye molecules increase as a function of time. In PSi structures, there is only one time-dependent parameter, which is the thickness of the silicon dioxide layer covering the nanostructure (see Figure 3.15). When the PSi sample is exposed to the ambient, the thickness of the SiO_2 layer gradually increases. Thus, the separation between the surface of the silicon nanostructure and the embedded BODIPY dye molecules (that is, d in Figure 3.15) increases. Confocal FLIM images of BODIPY-impregnated PSi are given in Figure 3.16. Such images are displayed using a continuous pseudocolor scale ranging from 1 to 3 ns (from blue to red). In other words, color of the images represents the fluorescence lifetime of BODIPY dye molecules on silicon microspheres.

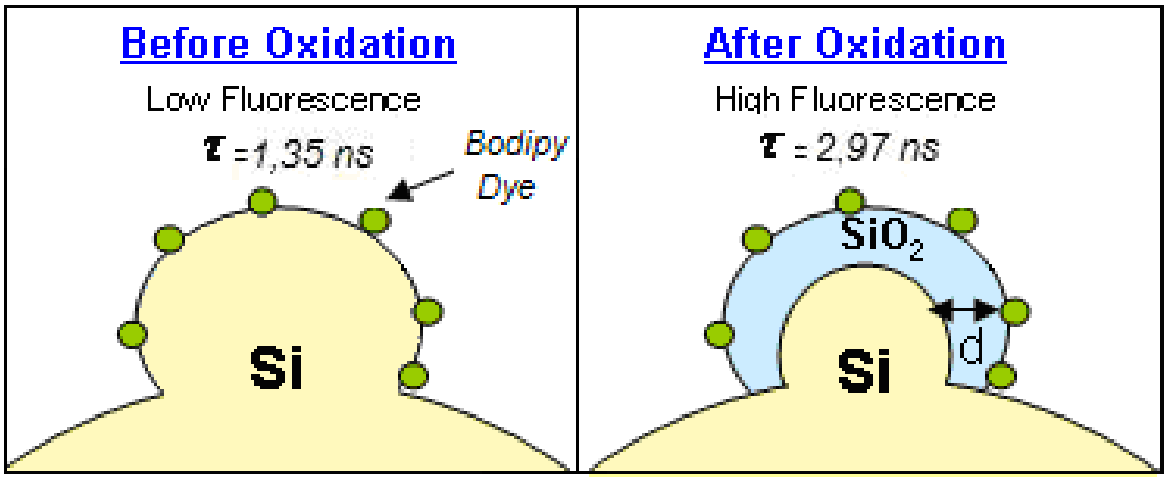

Figure 3.15. Schematic diagram of silicon nanostructures on microspheres.

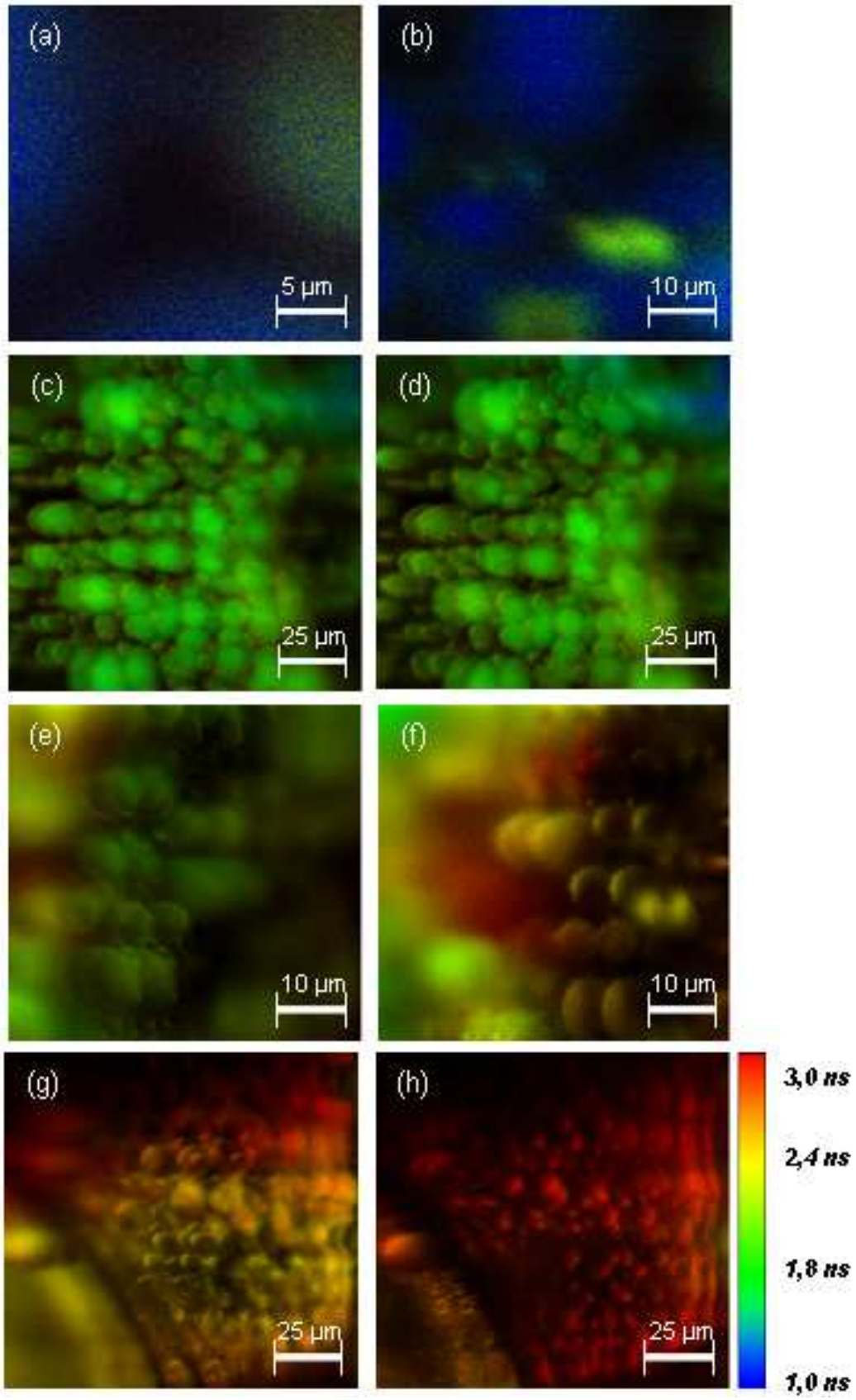

Figure 3.16. Confocal FLIM images of silicon microspheres and the effects of oxidation time on lifetime of BODIPY dye.

3.3.2. Monitoring Formation of SiO_2 Layer via a Confocal FLIM Based NSET Method

To explain the physics behind the fluorescence dynamics of the interaction between BODIPY azide dye molecules and the porous silicon nanostructure, one, first of all, needs to resolve whether the acceptor, which is the silicon nanosemiconductor as depicted in Figure 3.15 behaves as a dipole or a nanosurface agent. If the silicon acceptor acts like a dipole, this dipole-dipole interaction can be explained with the theory of the Fluorescence Resonance Energy Transfer (FRET, or Förster theory). Necessary conditions indicated by Förster theory are, first, the spectral overlap between the donor and acceptor; second, a coupling between the two systems; and third, the distance between the donor and acceptor being less than 10 nm [61]. Otherwise, it is more appropriate to explain the dipole-nano surface interaction by Nano Surface Energy Transfer (NSET) because in the physical origin of NSET theory, electromagnetic field of the donor-dipole interacts with the nearly free conduction electrons of the accepting nanosurface [62]. While a discrete resonant electronic transition is fundamental for FRET process, it is not necessary for the dipole-nanostructure interaction. Moreover, NSET is a technique that is capable of measuring distances nearly twice as far as FRET in which the energy transfer takes place from donor molecules to a nanosurface. It is obvious that SiO_2 layer acts like an insulator between Si nanostructures and the dye molecules and the thickness of this layer becomes an effective parameter in energy transfer mechanism, as depicted in Figure 3.15. To obtain information about the order of magnitude for the oxide layer's thickness on the porous silicon surface, the thickness of the oxide layer on a non-porous silicon surface is measured by a discrete wavelength ellipsometry (SC610, TeknoTip). The wavelength of ellipsometry source is HeNe laser with 632.8 nm, and data are acquired at 50° angle of incidence. Measured Ψ and Δ angles are 49.244 $\pm$ 0.492° and 168.539 $\pm$ 1.685°, respectively. The thickness of the native oxide layer is calculated to be 20.784 $\pm$ 1.252 nm with a 0.01 mean square error (MSE) value. According to our ellipsometric measurements, our system does not satisfy the close distance (i.e., a separation distance less than 10 nm) condition of FRET theory. Moreover, spectral overlap region between absorption spectrum of PSi and emission spectrum of BODIPY is very poor. Consequently, enhancement of BODIPY lifetime

on porous silicon nanostructures cannot be explained by FRET theory.

To address the interactions of molecules with surfaces over distances more than 10 nm, Nano Surface Energy Transfer (NSET) theory is described by Persson and Lang in 1982 [39]. According to this model, the electromagnetic field of the donor-dipole interacts with the nearly free conduction electrons of the accepting metal and these electrons behave like a Fermi gas. Energy transfer efficiency of NSET is proportional to the inverse fourth power of the distance between the donor-dipole and nanosurface. For a fixed separation distance d , the rate of energy transfer is given by [62]

$$k_{NSET} = (\frac{1}{\tau_D})(\frac{d_0}{d})^4 \tag{3.6}$$

where d_0 is a characteristic distance length at which a dye will display equal probabilities for energy transfer and spontaneous emission. In the Persson model, value of d_0 can be calculated by the following relation:

$$d_0 = (0.225\frac{\Phi_0}{w_{dye}^2}\frac{c^3}{w_F k_F})^{1/4} \tag{3.7}$$

where c is the speed of light, Φ_0 is the quantum yield, and w_{dye} is the angular frequency of the donor. For the BODIPY dye we used in our experiments, Φ_0 and w_{dye} are 0.90 and $3.49 \times 10^{15}\ s^{-1}$, respectively. w_F is the Fermi frequency and k_F is the Fermi wave vector of the nanosurface.

Although the Persson and Lang model is derived for a thin metal film nanosurface, it is successively applied to gold nanoparticles and dye interaction [63]. Moreover, several optical-based molecular rulers are designed to measure conformational changes in proteins and ribozymes [64, 65]. However, the NSET model has never been applied to a dye-semiconductor structure before. We anticipate that such a model is a well-appropriate scheme to apply to a dye and silicon-semiconductor system like ours, as described in this work, because it is well known that the nearly free electrons at the Fermi level take a crucial role in this energy transfer model. This condition is satisfied

with the existing free electrons at the Fermi level in silicon. Therefore, the NSET model is used to explain the fluorescence dynamics of the interaction between BODIPY dye molecules and silicon nanoparticles on a porous silicon surface. Thus, the energy transfer mechanism between the dye and silicon nanoparticle provides a new method for designing an optical nanoruler for the thickness of measuring the native oxide layer on a porous silicon sample. The Fermi energy level of porous silicon, which is prepared by electrochemical anodization of a p-type silicon wafer, is measured as 1.33 eV [66, 67]. The energy band structure of porous silicon is given in Figure 3.17. According to the energy band diagram of the PSi nanostructures, energy difference between the valance band and conduction band equals to 1.8 eV. When the PSi nanostructure is excited with the ultraviolet range laser ($\sim$ 450 nm), the PSi nanostructure emission spectrum peak wavelength value is calculated as

$$\lambda = \frac{hc}{\Delta E} = \frac{1.24 \times 10^{-6}\ eV.m}{1.8\ eV} = 688 \times 10^{-9}\ m. \tag{3.8}$$

On the other hand, our PSi nanostructure emission spectrum is measured by a fiber optic spectrometer and peak value is determined as 680 nm. This result shows that Fermi energy level can be taken as 1.33 eV. Therefore, Fermi angular frequency is calculated as

$$w_F = \frac{E_F}{\hbar} = \frac{(1.33\ eV)(1.602 \times 10^{-19}\ J/eV)}{1.05 \times 10^{-34}\ Js} = 2.03 \times 10^{15}\ s^{-1} \tag{3.9}$$

and Fermi wave vector values is calculated as

$$k_F = \sqrt{\frac{2mE_F}{\hbar^2}} = 5.94 \times 10^{9}\ m^{-1}. \tag{3.10}$$

Then, the NSET characteristic distance d_0 is calculated as $13.9 \times 10^{-9}\ m^{-1}$ via Equation 3.7.

The efficiency of energy transfer (E) is an important parameter for the NSET process. It is defined as the proportion of the photons absorbed by the donors, which

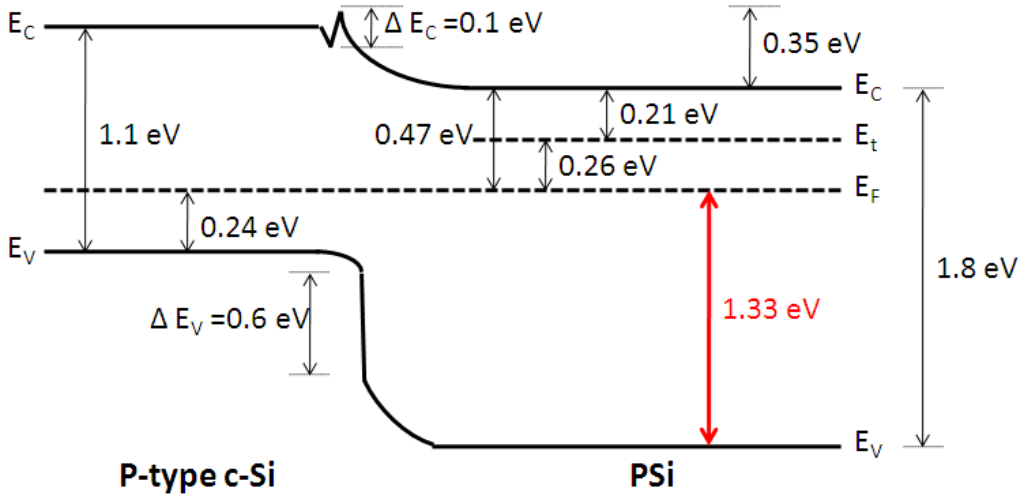

Figure 3.17. Schematic of deduced energy band diagram of c-Si and PSi [68].

are transferred to acceptor silicon nanosurface. The NSET efficiency can be written directly in terms of distances as using Equation 2.25. The efficiency of the energy transfer can also be determined from the time resolved lifetime measurements using Equation 2.24. The distance between the donor and accepting nanosurface or the thickness of oxide (SiO_2) layer can be calculated using Equation 2.24 and Equation 2.25 as a function of fluorescence lifetime of the donor BODIPY dye molecules.

Table 3.3. Experimentally Calculated SiO_2 Layer Thickness on Porous Silicon.

$FLIM$ $Image$	$Oxidation$ $Time$	$ScanArea$ (μm)	τ_{AV} (ns)	$EnergyTransfer$ $Efficiency(E)$	$SiO_2Thickness$ d(nm)
(a)	1	25 × 25	1.35	0.73	10.88
(b)	2	50 × 50	1.37	0.72	10.94
(c)	9	100 × 100	1.79	0.64	12.07
(d)	14	100 × 100	1.98	0.60	12.57
(e)	37	50 × 50	2.19	0.56	13.13
(f)	51	50 × 50	2.42	0.51	13.76
(g)	63	100 × 100	2.82	0.43	14.93
(h)	70	100 × 100	2.97	0.40	15.40

Oxidation time, scan area, and average lifetime values of the related FLIM images are summarized in Table 3.3. Just after BODIPY azide dye molecules attached to the porous silicon surface, the energy transfer efficiency is found to be about 73% and the distance between the dye and the nanosurface (or the thickness of the oxide layer) is calculated as 10.88 nm by the NSET model. As the PSi surface oxidizes in air, the energy transfer efficiency reduces to 40%, which corresponds to an oxide layer thickness of 15.40 nm. The pseudocolor scale property of the FLIM images, which are shown in Figure 3.15, provides convenience in order to estimate the oxide thickness on the PSi surface. For example, the SiO_2 thickness corresponds to 10 nm in blue regions and 15 nm in red regions. Therefore, the map of the oxide layer for PSi samples, together with their oxide layer's depth, is obtained via the FLIM method [68]. The energy transfer rate and lifetime versus the oxide layer's thickness are shown in Figure 3.18.

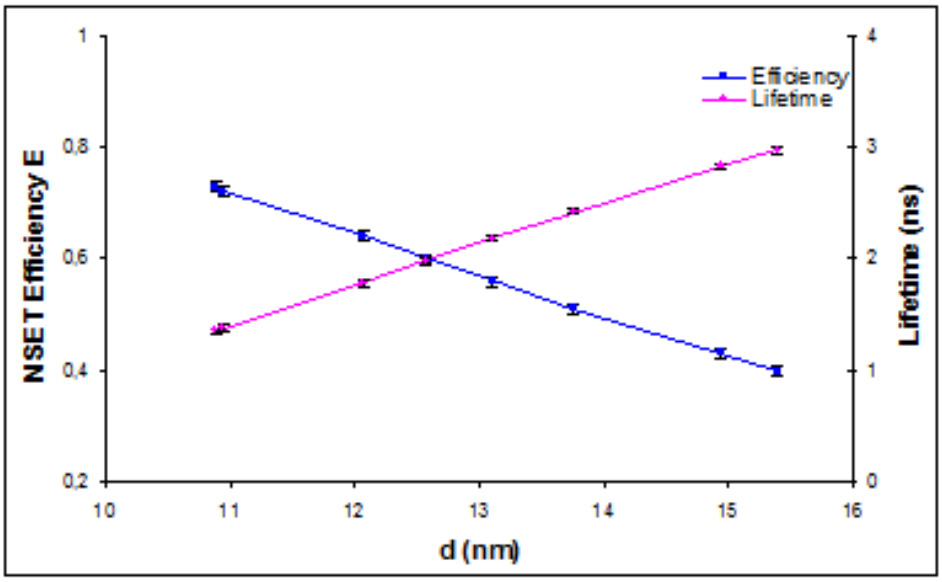

Figure 3.18. Dependency of the NSET energy-transfer efficiency (E) and fluorescence lifetime of BODIPY dye (τ) on silicon oxide layer thickness.

A grown silicon dioxide layer on the surface is very resistant and can only be etched by hydrofluoric acid (HF). Water or other acid types cannot remove this layer from the silicon surface. Silicon nanostructures are obtained from an electrochemical anodization method in a HF solution. Therefore, as the etching process starts, the SiO_2

layers on these nanostructures are completely removed. After BODIPY dye solution is deposited on the silicon nanostructures, these structures are exposed to air and the oxidation process restarts from the beginning.

Our experimental FLIM results of SiO_2 thickness values are found to be consistent with the ellipsometric measurements, which are performed for a nonporous silicon wafer. Because the rough (or pillar-like) surface of a porous silicon sample does not allow measuring the oxide layer thickness using a conventional ellipsometric technique, a nonporous silicon wafer is considered to be a fairly good alternative to calculate and compare the oxide thickness with the oxide layer formed on the surface of a nanoporous silicon structure. The reason that a nonporous wafer is chosen for comparison of the SiO_2 thicknesses is due to the fact that, during the oxidation process, solid silicon crystals and oxygen molecules react to form a silicon dioxide layer on the crystal surface.

$$Si + O_2 \rightarrow SiO_2 \tag{3.11}$$

Initially, the growth of the silicon dioxide is only a surface reaction which is given in Equation 3.11. However, as the SiO_2 layer begins to build up, the arriving oxygen molecules naturally diffuse through this growing layer to get to the silicon surface in order to react. The growth rate primarily depends on the velocity of the oxygen diffusion through the silicon dioxide layer. In addition to the oxygen penetration rate, the doping type (n or p) and orientation of silicon crystals become important parameters in determining the reaction time of the oxygen and silicon. Therefore, it is expected that the oxide layer's thickness on the surface of a flat silicon wafer and a porous nanostructure produced from the same wafer should be relatively close to each other. In our experiments, each time before sample preparation of the nanostructures, a small piece is chopped from the silicon wafer for ellipsometric measurements of the oxide layer's thickness. Our nanostructures are exposed up to 70 day, which is a pretty long time period for the formation of the silicon dioxide layer to compare to that of the nonporous wafer's one. The maximum thickness measured for 70 day sample is 15.40 nm, which is close to the figure measured for the flat silicon wafer, that is,

20.784 ± 1.252 nm. This indicates that the experimental results and the NSET model give realistic results. If one waits for a very long time period, for example, about a year, it is likely that the oxide layer thickness on the surface of our nanostructures will be almost the same as that of the normal nonporous silicon wafer.

3.4. Interaction Between Two BODIPY Azide Dye Molecules within a PEG-Based Hydrogel

In this work, a chemically cross-linked three dimensional hydrogel network is doped with different concentrations of BODIPY dye molecules. They are covalently bound to a polyethylene glycol based hydrogel structure at two different concentrations: highly concentrated and dilute. The concentration of the dye molecules is controlled with the number of free reactive alkyne groups within the gel matrix. It is observed that the fluorescence intensity drastically decreases when the number of BODIPY azide dye molecules is increased within a cluster of a hydrogel. On the other hand, the fluorescence intensity significantly increases when the concentration of the dye molecules is reduced. The rationale of this research is to reveal the transduction mechanism that governs such a molecular concentration-dependent fluorescence change of the BODIPY dyes by means of a time-resolved fluorescence lifetime measurements.

3.4.1. General Synthesis of Hydrogels via [3+2] Huisgen "Click" Chemistry

To a small vial is added poly(ethylene glycol)-bis-octaacetylene **1** (20 mg, 2.67 μmol), tetra(ethylene glycol) diazide **2** (0.652 mg, 2.67 μmol) in H_2O (18 μL) and ethanol (50 μL). To the vial is added deionized H_2O (110 μL) containing sodium ascorbate (1.0 mg, 5.04 μmol) and the mixture is mixed under ultrasound to give a clear solution. Copper sulfate (1.0 mg, 6.28 μmol) in water (25 μL) is added and after stirring for 10 seconds, the reaction mixture is poured into a teflon O-ring with 1.5 mm height and 1.0 cm diameter. The bottom of the ring is capped with a teflon rod and upon addition of the reaction mixture, the ring is covered with a glass slide. The solution is allowed to react for 10 min at room temperature and then the glass slide is removed. The formed gel is taken out of the ring with the help of the teflon rod

and then is submerged into an aq EDTA solution (5%, pH 7-8) to extract the trapped $CuSO_4$ and ethanol and finally is washed with deionized water.

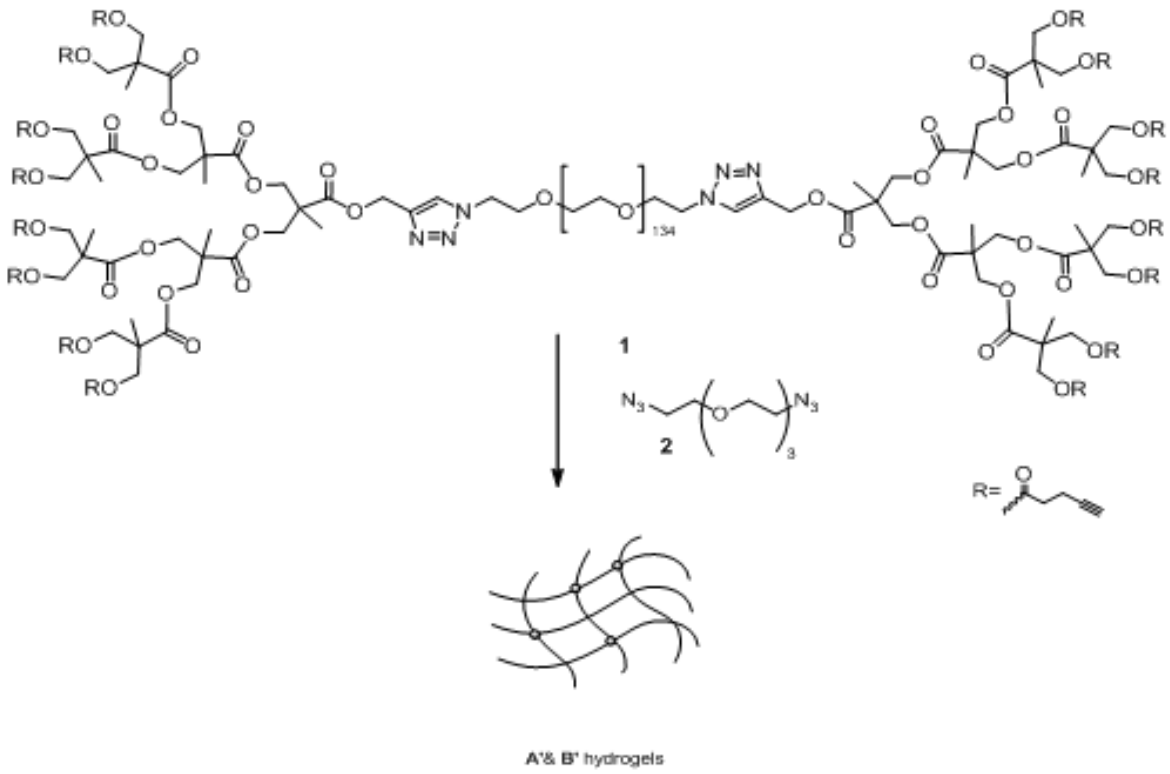

Figure 3.19. Chemical synthesis of hydrogels.

Procedure outlined above is used to make (**A**) hydrogel which is containing 50:50 percent ratio of crosslinker **2** and copolymer **1**. Same procedure is used only changing the crosslinker percent ratio of 75:25 monomers to form (**B**) hydrogel containing less amount of remaining alkyne functional groups. The control of free reactive alkyne groups provides a handle for precise control on the location of dye attachment.

3.4.2. Functionalization of Hydrogel with Concentrated and Dilute BODIPY Azide Dyes

Two identical cylindrically shaped hydrogels (**A** & **B**) are synthesized (each about 20 mg) and placed into two different vials. Prior to the reaction, the hydrogels are washed with THF to remove water. BODIPY azide **4** (0.25 mg, 0.00058 mmol) in THF

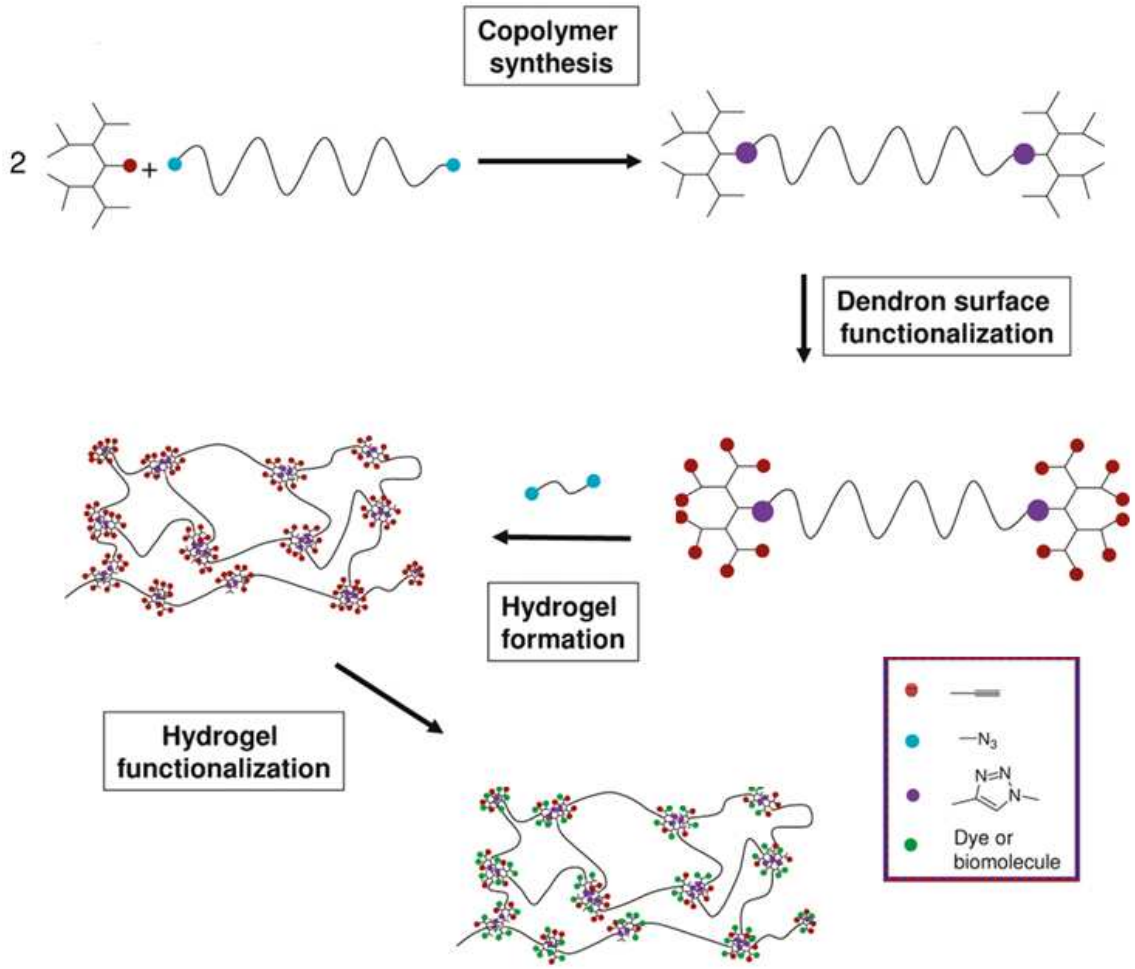

Figure 3.20. General Scheme for the Synthesis of Functionalized Hydrogels [69].

(2.5 mL) is added to each of the vials. PMDETA (1.20 L, 0.0058 mmol) and CuBr (1.00 mg, 0.007 mmol) are added to vial of A and B for copper catalyzed cycloaddition. The reactions are stirred at room temperature for 12 h. After the reaction is completed, hydrogels are washed with THF to remove any trapped dye molecules and then washed with an aq EDTA solution (5%, pH 7-8) to extract the trapped $Cu(I)Br$ and finally washed with deionized water [69].

Fiber optic spectrometer is used to monitor the effects of the dye concentration on the BODIPY-doped hydrogel photoluminescence. The number of the reactive alkyne groups in highly concentrated hydrogel is larger than that of the dilute one; as a result, BODIPY dyes aggregate in clusters in highly concentrated hydrogel matrix. It

is observed that there are two important differences between concentrated and dilute hydrogels: emission spectrum of highly concentrated hydrogel is red shifted and the fluorescence intensity of this gel severely decreases due to the high concentration of the dye molecules (see Figure 3.21).

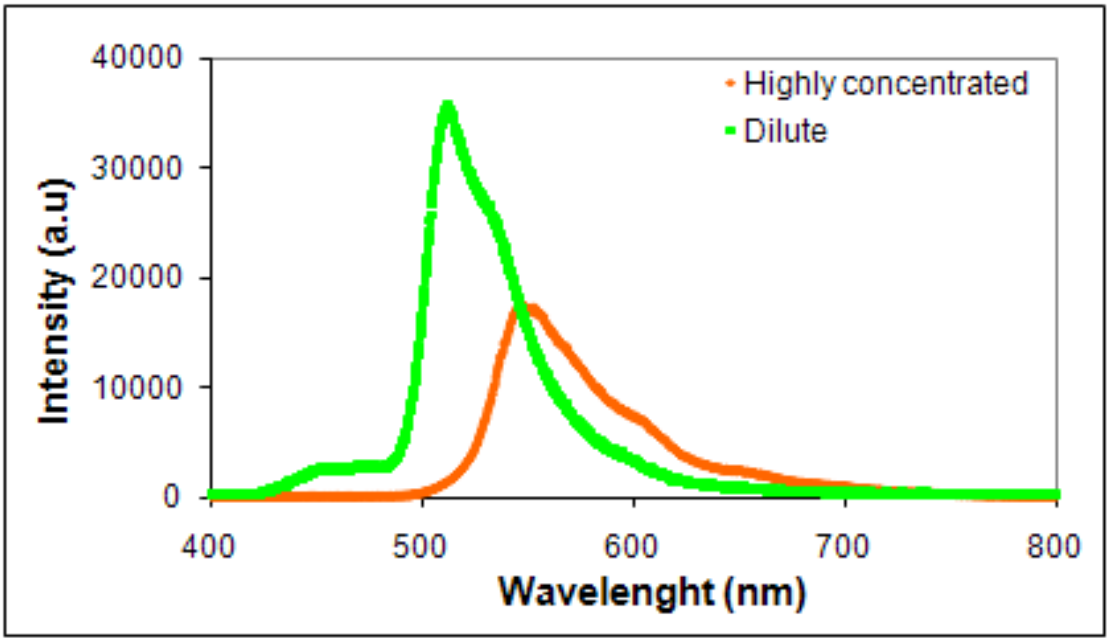

Figure 3.21. The fluorescence intensity of highly concentrated and dilute hydrogels.

3.4.3. Swelling Properties of the Highly Concentrated and Dilute Hydrogel

To reveal the dynamics of the fluorescence mechanism, we decided to gradually increase the distance between the BODIPY dye molecules through exposing the hydrogels to water induced swelling. Water induced swelling process of a hydrogel can be controlled with the following parameters: the pH value of the hydrogel, the salt concentration in the hydrogel system, and immersion time in distilled water [70-72]. In our work, the swelling experiments for the hydrogels are carried out at room temperature in distilled water. Dried hydrogel is immersed in distilled water. By taking the sample out of the water periodically, their mass and the fluorescence lifetime of BODIPY dye

are measured. The percentage swelling ratio ($\%S$) is expressed as:

$$\%S = \frac{W_t - W_0}{W_0} \times 100 \tag{3.12}$$

where W_0 and W_t are the weights of hydrogels initially and at time t, respectively. Figure 3.22 shows the dependency of the percentage swelling ratio of hydrogels on swelling time. The equilibrium swelling value of concentrated BODIPY dye attached hydrogel is obtained after 100 min of swelling, reaching a maximum $\%S$ of around 800. Moreover, the dilute BODIPY attached hydrogel saturates after 100 min and its maximum swelling ratio value is measured to be about 1200.

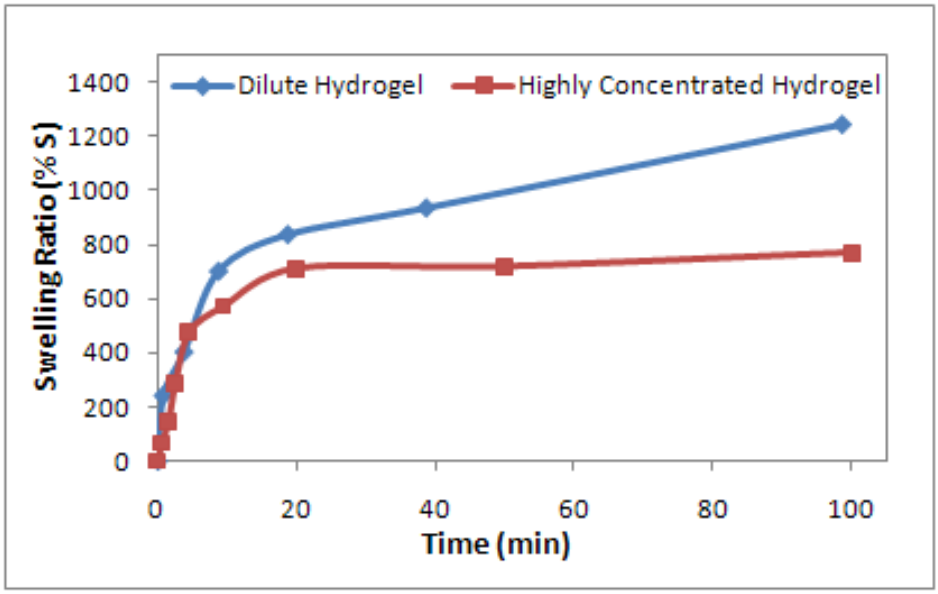

Figure 3.22. Dependency of swelling ratio ($\%S$) of highly concentrated and dilute hydrogel on time.

3.4.4. Swelling Effects on the Fluorescence Lifetime of BODIPY Dye

The time-resolved fluorescence lifetime of the BODIPY dye molecule is performed using the Timeharp 200 PC-Board system. The measurement of the fluorescence lifetime is based on the time correlated single photon counting (TCSPC) method. In this method, the time between the detected single photon of the fluorescence (start signal)

and the excitation laser pulse (stop signal) is measured. The measured data is plotted as a fluorescence lifetime histogram (see Figure 3.23). The fluorescence lifetime of BODIPY dye molecules attached to dried and swollen hydrogel network are compared. The results for highly concentrated and dilute hydrogels are presented in Figure 3.24 and Figure 3.25, respectively.

As the hydrogel sample swells, the fluorescence lifetime of BODIPY dye molecule increases in both hydrogel networks. Decay parameters are determined using the double exponential tailfit model and the best fits are obtained by minimizing the values. Decay times for concentrated and dilute type hydrogels are summarized in Table 3.4 and Table 3.5, respectively. In the highly concentrated sample, we measured a fluorescence lifetime increase up to a factor of 3.5 at room temperature ($\langle\tau\rangle_{dry}$=2.0309 ns and $\langle\tau\rangle_{swollen}$=7.1437 ns). Moreover, the value of the intensity weighted average lifetime of dried dilute hydrogel increases from 5.6154 to 6.3292 ns.

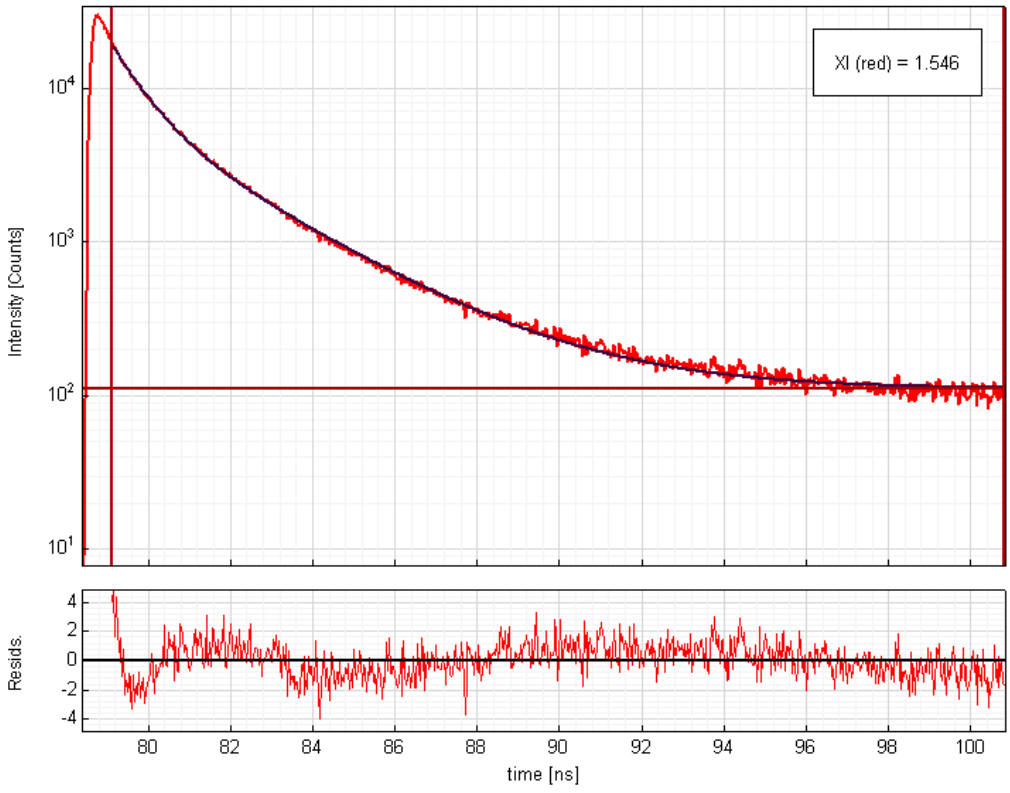

Figure 3.23. Decay fitting and calculation of the decay parameters of dried highly concentrated hydrogel ($\%S = 0$).

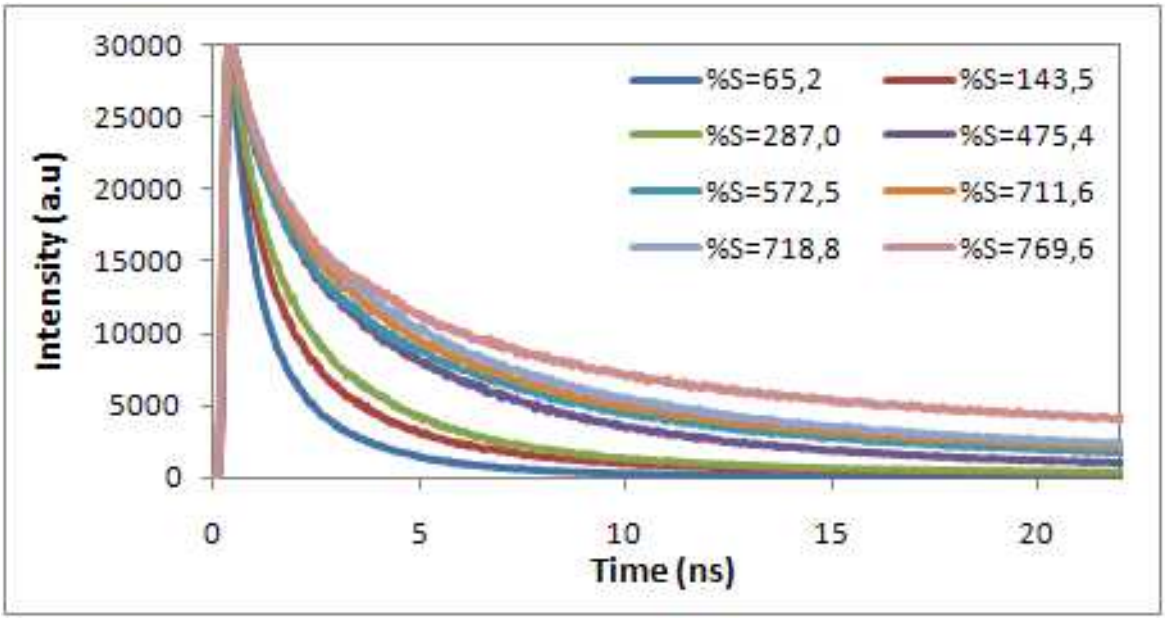

Figure 3.24. Decay plots of highly concentrated hydrogel for different swelling ratios ($\%S$).

Table 3.4. Decay Parameters for Highly Concentrated BODIPY-Azide-Doped Hydrogel.

% S	A_1	τ_1	A_2	τ_2	χ^2	$\bar{\tau}$	$\langle\tau\rangle$
0	6540.2	2.7071	12454	0.7510	1.546	1.4245	2.0309
65.2	7038.0	3.9975	11965	1.1025	1.917	2.1747	3.0734
143.5	9239.3	4.0607	10363	1.2162	1.602	2.5569	3.3454
287.0	14883.9	5.3893	7657	1.1440	1.329	3.9472	4.9713
475.4	13466.5	6.0868	7313	1.1993	1.302	4.3667	5.6144
572.5	14065.4	6.2000	8188	1.4229	1.597	4.4423	5.6370
711.6	14608.7	6.5150	7557	1.4810	1.377	4.7987	5.9853
718.8	13113.3	7.2000	8204	1.3099	1.753	4.9332	6.5981
769.6	12746.0	8.0304	9939	1.6674	1.768	5.2426	7.1437

Table 3.5. Decay Parameters for Dilute BODIPY-Azide-Doped Hydrogel.

% S	A_1	τ_1	A_2	τ_2	χ^2	$\bar{\tau}$	$\langle\tau\rangle$
0	17050.4	5.9648	7958	0.9591	1.386	4.3719	5.6154
242	16003.3	6.0365	7523	0.9625	1.896	4.1440	5.6827
404	16255.3	6.1556	7628	0.9325	1.956	4.4874	5.8089
702	16986.5	6.1100	6327	0.9218	1.527	4.7020	5.8340
838	13254.0	6.6274	6900	1.3695	1.181	4.8273	6.1167
937	15003.0	6.9520	7256	1.9620	1.856	5.1906	6.1618
1246	19025.0	6.3850	5826	2.0689	1.569	5.4270	6.3292

Where intensity weighted average lifetime values ($\langle\tau\rangle$) are calculated using Equation 3.4 and the amplitude weighted average lifetime values ($\bar{\tau}$) are calculated using Equation 3.5.

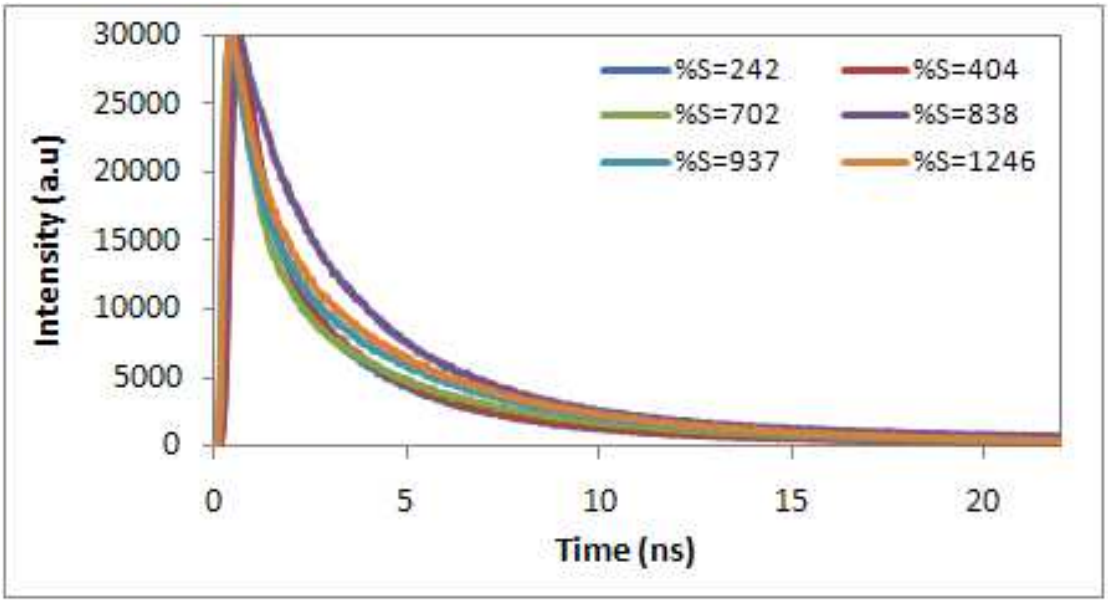

Figure 3.25. Decay plots of dilute hydrogel for different swelling ratios (%S).

3.4.5. Calculation of Spectral Overlap Region and Förster Distance R_0

One of the criteria which must be satisfied in order for Förster resonance energy transfer to occur is spectral overlap region between emission spectrum of the donor and absorption spectrum of the acceptor molecule. In this work, the donor and the acceptor are the same species and Figure 3.26 shows the absorption and emission spectra obtained from the highly concentrated and dilute BODIPY attached hydrogel samples. According to these spectra, fluorescence energy transfer is very likely to occur between two BODIPY dye molecules in both hydrogel networks.

It is found that there is a good spectral overlap between the fluorescence and absorption spectra of the concentrated BODIPY, whereas the overlap between the fluorescence and absorption spectra of the dilute BODIPY is comparatively poorer. Concentration-dependent spectroscopic characteristics of BODIPY dye molecules in hydrogel networks and their Förster distances are given in Table 3.6. We are particularly interested in the case where the dyes have rapidly rotating dipoles; therefore the κ^2 orientation factor value is taken to be 2/3. Refractive index of the medium is 1.4 and the quantum yield is equal to 0.9 in methanol [73]. The spectral overlap integral $J(\lambda)$ is calculated using Equation 2.36. The value of the Förster distances R_0 is determined using Equation 2.35.

Table 3.6. Spectroscopic Characteristics of BODIPY Azide Dye in the Hydrogel Network.

Hydrogel type	λ_{abs} (nm)	λ_f (nm)	$\varepsilon^1 M^{-1} cm^{-1}$)	$J(\lambda)(M^{-1}cm^3)$	$R_0(nm)$
concentrated	528	548	70000	1.763×10^{13}	5.38
dilute	504	512	82000	1.086×10^{13}	4.96

[1]The molar extinction coefficient at the peak wavelength.

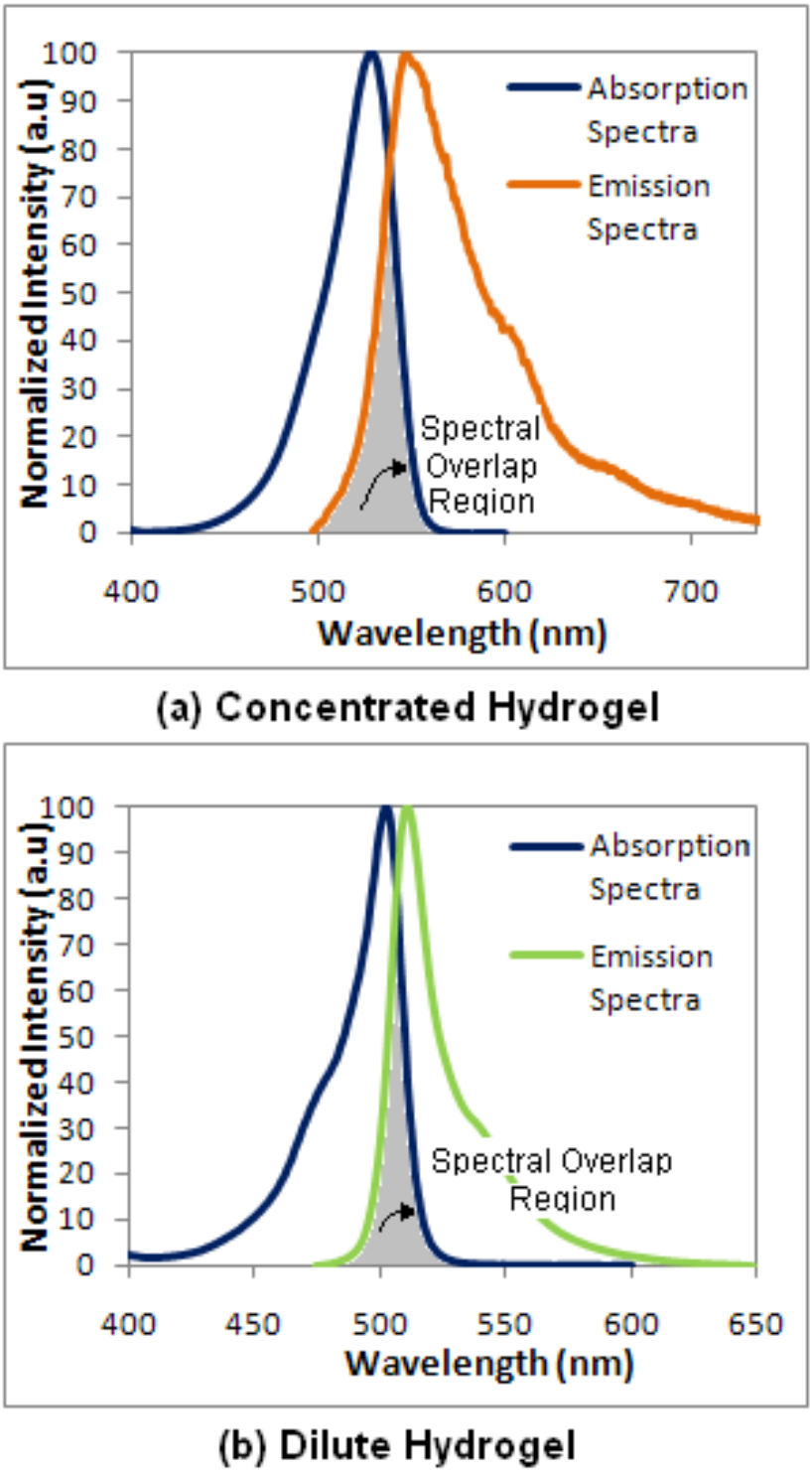

Figure 3.26. Normalized absorption and emission spectra for (a) Highly concentrated BODIPY dye doped hydrogel and (b) Dilute BODIPY dye doped hydrogel.

3.4.6. Energy Transfer Mechanism Between BODIPY Dye Molecules

If the donor and acceptor fluorophores in the hydrogel clusters are the same species, like the BODIPY dye molecules used here in this work, two different types of mechanism can be effective on quenching of the fluorescence intensity: self-quenching (or contact quenching) and fluorescence resonance energy transfer (FRET). Self-quenching is the predominant mechanism of quenching if there is a physical contact between the donor and acceptor dye molecules. Otherwise, FRET becomes the predominant mechanism and efficiency of the energy transfer is strongly sensitive to the distance between the donor and acceptor, typical distance changes from $\sim$ 1 to 10 nm. It is possible to find many applications of the fluorescence self quenching method in the literature. For example, recently, fluorescence quenching between two dye molecules has been employed to elucidate the movement of single kinesin molecules on microtubules in real time [74]. Calculations based on our experimental results, specifically, the overlap integral that represents the degree of the spectral overlap between the donor emission and the acceptor absorption, confirm that the fluorescence dynamics of the BODIPY azide dye molecules confined within the hydrogel network obeys the Förster resonance energy transfer.

It is seen that an efficient FRET is taking place between two BODIPY dye molecules that are both covalently bound to the same cluster of a hydrogel network. As the Förster resonance energy transfer theory states, FRET efficiency E depends on the distance between the donor-acceptor pairs (Equation 2.41) and also the lifetime of the donor molecule (Equation 2.42). The distance between two BODIPY dye molecules at different swelling ratios is calculated via fluorescence lifetime measurements. Experimental data points for r -shown in Table 3.7 and 3.8 also in Figure 3.27- are obtained through the experimental values of FRET efficiency E, which are obtained from the lifetime measurements, using Equation 2.41. The theoretical solid curves in Figure 3.27 are generated for the FRET efficiency E versus r (again using Equation 2.41) by simply giving arbitrary values to distance r from 0 to 15 nm. It is seen that our experimental data points fall on these theoretical curves when R_0 values are adjusted to 5.4 nm and 5.0 nm, which are quite close to our experimental R_0 values (i.e., 5.38 nm and 4.96

nm). Figure 3.27 is useful, since it shows where the data points lie on these curves; however, this shall not be interpreted as a perfect agreement between the theory and experiment as the experimental data points do not carry any more information than the tables. Such proper donor-acceptor distances are summarized in Tables 3.7 and Table 3.8, together with the percentage swelling and the FRET efficiency E.

Table 3.7. S, E and r Values for the Concentrated Hydrogel Sample ($R_0 = 5.38$ nm).

% S	E	r(nm)
0	0.721	4.59
65.2	0.578	5.11
143.5	0.540	5.24
287.0	0.317	6.11
475.4	0.229	6.59
572.5	0.226	6.61
711.6	0.178	6.94
718.8	0.094	7.85
769.6	0.019	10.41

Table 3.8. S, E and r Values for the Dilute Hydrogel Sample ($R_0 = 4.96$ nm).

% S	E	r(nm)
0	0.229	6.07
242	0.219	6.13
404	0.202	6.24
702	0.199	6.26
838	0.180	6.54
937	0.127	6.84
1246	0.043	8.31

From the absorption and emission spectra shown in Figure 3.26, the value of the Förster distance is determined to be 5.38 nm for the concentrated type hydrogel sample. When the hydrogel is in the deswollen state, the energy transfer efficiency equals to 72% and the fluorescence lifetime of the BODIPY dye molecules is measured to be 2.031 ns. Using Equation 2.39 and 2.40, the distance between two dye molecules within the cluster is calculated as 4.59 nm. After immersion of the concentrated hydrogel in distilled water, its average lifetime is measured at definite intervals of time and the separation between two dye molecules is calculated for each swelling ratio. The lifetime measurements are iterated until the hydrogel achieved a constant weight. It is observed that the average lifetime of the concentrated hydrogel starts to increase. For a water-saturated hydrogel state, average lifetime is measured up to 7.143 ns. In this case, the bonds within the cluster are widely separated from each other and the distance between the two close BODIPY dye molecules reaches 10.41 nm, which corresponds to a FRET efficiency of about 2%. On the other hand, the Förster distance of the BODIPY dye molecule, which is covalently bound to dilute hydrogel, is calculated as 4.96 nm. As far as the dried dilute hydrogel sample is concerned, the fluorescence energy transfer efficiency equals to 23% and the fluorescence lifetime is measured to be 5.615 ns. After applying the same swelling process, the fluorescence lifetime of the BODIPY dyes increases up to 6.329 ns and the distance between the two close BODIPY dye molecules reaches 8.31 nm, which corresponds to a FRET efficiency of about 4.30%.

It is well known that a hydrogel consists of a network of polymer chains. Any two polymer chains are connected to each other with a cluster, that is, a cross linking point. Each cluster is depicted with a red dot in Figure 3.28 and has also a flexible chemical structure. The method of cross-linking used here in this work for preparation of samples allows one to obtain hydrogels with a control over the degree of cross-linking and also control over the number of reactive groups in its interior. This control of reactive groups allows controlled dye loading using covalent dye immobilization. In this work, two different hydrogels are prepared, one with concentrated and the other with dilute BODIPY fluorophore density. Experimental results presented in this thesis give the following physical insight of this work and help explaining the significance of the

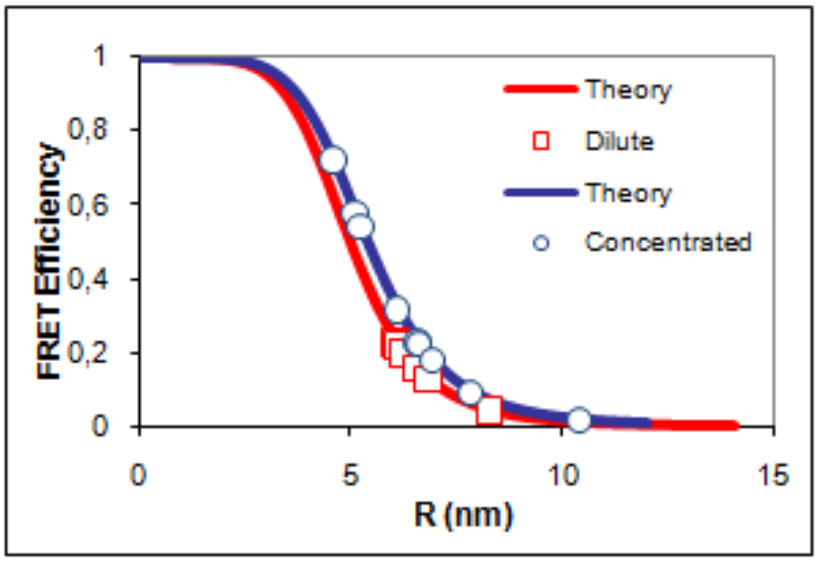

Figure 3.27. Normalized FRET efficiency and the separation between two dye molecules within one cluster of highly concentrated hydrogel and dilute hydrogel.

measurements on commenting the fluorescence dynamics of the BODIPY dye molecules attached to hydrogel clusters: A BODIPY dye molecule is used as both a donor and an acceptor fluorophore, which is covalently bound to the same cluster. As briefly stated above, when the donor and acceptor fluorophores are chosen to be the same species, two different types of mechanism can be effective on the dynamics of the fluorescence intensity. These mechanisms are self-quenching (or contact quenching) and fluorescence resonance energy transfer. Self-quenching is the predominant mechanism of quenching if there is a physical contact between the donor and acceptor dye molecules. In this kind of processes, the typical donor-acceptor separation is less than 1 nm. If such a donor-acceptor separation is between 1 and 10 nm, fluorescence resonance energy transfer becomes the predominant mechanism and the efficiency of energy transfer is strongly sensitive to the distance between the donor and acceptor. Since our hydrogels are designed to allow attachment of the dye molecules only at cross-linking points, one needs to clarify whether the fluorescence energy transfer or self-quenching is due to the interaction of the dye molecules within the same cluster or between the molecules in different clusters of the hydrogel network, before deciding which mechanism is predominant for the fluorescence dynamics. As two clusters of the hydrogel are connected to each other with long hydrophilic polyethylene glycol polymer chain, which has 134

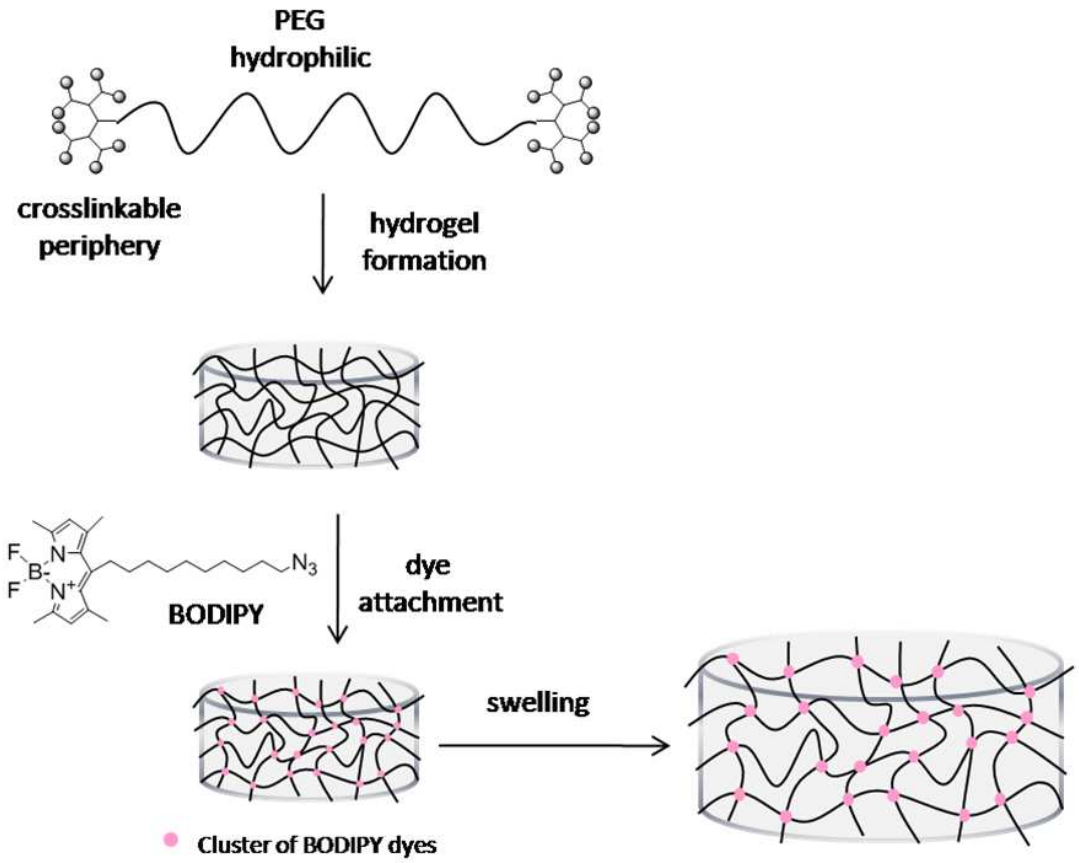

Figure 3.28. General illustration of stimuli responsive fluorescent hydrogel.

repeating units of ethylene glycols, and the length of this polymer chain is expected to be longer than 40 nm when the hydrogel is fully swollen, it is obvious that the cluster-cluster interaction of the hydrogel have no contribution effects neither on self quenching nor on resonance energy transfer. However, the spectral overlap shown in Figure 3.26 between the fluorescence and absorption spectra of the BODIPY together with the determined molecular separations of 5.38 nm and 4.96 nm strongly suggest that the underlying predominant fluorescence mechanism is based on the resonance energy rather than that of self-quenching. Such a large molecular separation implies that there is no physical contact between two dye molecules within one cluster of the hydrogel matrix. Furthermore, one more verification that our fluorescence dynamics does not obey self quenching but conforms to resonance energy transfer is due to the concentration induced change in the lifetime of the dyes and the red-shift occurrence in the absorption spectrum. As it is known that self-quenching takes place between the same type of the dye molecules and is divided into two categories; namely, static self-

quenching and dynamic self-quenching [75]. In the static self-quenching, absorption spectrum of the dye molecules is red-shifted upon increasing the dye concentration in the network but lifetime of the molecules is constant and experiences no change [76, 77]. In the dynamic quenching case, the lifetime of molecules change as the dye concentration is altered; however, no spectral shift occurs in the absorption spectrum [78, 79]. Additionally, for very dilute dye concentrations, one may observe a complete self-quenching, that is, no fluorescence intensity at all, when two single molecules are touching each other [74]. In our experiments, fluorescence is never detected to be zero even for extremely dilute samples; moreover, both spectral shift and concentration induced change in the lifetime is observed for the BODIPY dye molecules used in the hydrogel network.

The separation displacement between dye molecules is studied via exposing the BODIPY doped hydrogel samples to water induced swelling. As far as the physical mechanism is concerned, we may assume each cluster, depicted with red dot in Figure 3.28, as a spherical polymer ball that contains covalently bound hydrogel BODIPY azide dye molecules. Water induced swelling of the hydrogel causes elongation in the network chains and hence introduces tensional forces onto the clusters, causing an increase in the volume of the cluster and consequently forcing attached-BODIPY-molecules to undergo a separation from each other. The level of fluorescence intensity is observed to clearly increase as the dye separation increases. When the hydrogel is in a dehydrated (or deswollen) state, BODIPY dye molecules are in close proximity and one BODIPY molecule can transfer its energy to another one. As a result, the decay time of the BODIPY dye molecules is quenched and their intensity weighted average lifetime decreases.

An alternative way of determining the separation distance between two dye molecules is to extract such information from the fluorescence intensity measurements. In our experiments, as seen in Figure 3.21, it is observed that the emission spectrum of the highly concentrated dye molecules is red-shifted and the fluorescence intensity is dramatically low when compared to the dilute sample. This is mainly due to formation of aggregates and hence the resonance energy transfer of the dyes in the hydrogel clus-

ters, which significantly reduces the fluorescence intensity of these dyes. By changing the swelling ratio, one can increase the dye-dye separation without deforming the network and hence can partially avoid the effects of this phenomenon on the fluorescence intensity. However, for a dynamic system like ours, intensity based measurements may not be absolutely reliable since each time one needs to monitor the fluorescence intensity over the same number of dye clusters through a confocal microscopic technique. As the hydrogel swells, the physical locations of these dye-doped clusters will not remain the same, and therefore, one may not guarantee the same number of the dye clusters to get trapped within the spot size of the monitoring laser beam upon swelling. Therefore, we believe that the time resolved technique presented in this paper is much accurate, more reliable method and also does not suffer from the aforementioned deficiency.

4. CONCLUSIONS

The illumination light source effects on the structural properties of porous silicon are described for the samples produced by an electrochemical anodization method. Conical regular nanopillar structures are formed under pulsed, coherent and monochromatic UV illumination. While white light source irradiation, which contains multiple wavelengths, causes formation of irregular nano-pores with various diameters, a blue LED irradiation gives relatively regular and greater nanopores. Our work shows that the porous layer structure can be controlled easily by suitable selection of a coherent illumination light source and better control can be achieved when a pulsed UV laser is used in the etching process. The wavelength effects on the pillar tip size and vertex angle are investigated for 337, 405 and 467 nm UV pulsed lasers. As the illumination wavelength increases, the nanopillar size increases proportionally. In addition to structural analysis, the fluorescence dynamics due to the interaction of fluorescent BODIPY azide dye molecules with such silicon nanostructures is studied with a time resolved fluorescence lifetime measurement system. The fluorescence lifetime of a dye molecule in the close proximity of silicon nanopillar is inhibited, which means that the spontaneous emission rate depends on the pillar size. In other words, smaller nanopillars give rise to smaller lifetimes for BODIPY dye molecules. A pulsed UV tunable source can be conveniently used to produce appropriate pillar sizes and hence the desired lifetimes.

The fluorescence dynamics due to the interaction of fluorescent BODIPY azide dye molecules with a porous silicon nanostructure is described via fluorescence lifetime imaging. When a dye molecule is attached to a freshly etched PSi surface, the fluorescence of the dye molecule is almost completely quenched. As the porous silicon nano structure oxidizes over time, fluorescence intensity of the attached dye molecules increases. As the growing oxide layer increases, the separation between the dye and the semiconductor nanostructure increases, thus causing a significant increase in the fluorescence lifetime of the dye molecules. Due to the thickness of the oxide layer, which acts as an insulator, being more than 10 nm, it is anticipated that the effective energy transfer mechanism is based on nano surface energy transfer process. BODIPY

dye molecules transfer their electronic state energy to the porous silicon nanosurface through the free Fermi electrons. Oxidation converts the porous silicon semiconductor to a SiO_2 insulator, significantly reducing the free carrier concentration and density of the free electronic states. Therefore, the fluorescence lifetime of BODIPY dye on oxidized porous silicon is much greater than the freshly etched porous silicon. The enhancement in the fluorescence lifetime is attributed to a reduction in the efficiency of the energy transfer between the BODIPY azide dyes and the PSi nanostructure. The increase in the fluorescence lifetime measured from the dye-modified PSi nanostructures provides a convenient means of monitoring the extent of the oxidation of the porous silicon surface. In this work, NSET theory is successfully combined with the FLIM microscopy method in order to monitor the PSi surface topography and obtain a three-dimensional map of the oxide layer on a PSi nanosurface.

The last part of this work describes the fluorescence dynamics of BODIPY azide dye molecules embedded within a hydrogel matrix employing time-resolved fluorescence lifetime measurements. Due to the distance between the dye molecules being smaller than 10 nm, it is anticipated that effective dynamical mechanism is based on the resonance energy transfer process. The conformational change in hydrogel clusters is analyzed and the distance between the dye molecules inside one cluster is calculated with respect to the lifetime of donor molecule in the presence of the acceptor for different swelling ratios. Förster distance measurements show that the energy transfer observed in these gels is due to dipole-dipole (or dye-dye) interaction that are confined in individual single clusters but not due to cluster-cluster interactions. Water induced swelling allowed us to continuously change the distance between the dye molecules. Upon swelling, the physical displacement between BODIPY-doped clusters, that is, the red color nodes shown in Figure 3.28, increases. However, this cluster displacement is far too big to affect the dipole-dipole interaction and consequently has no possessions on the fluorescence self-quenching and the Förster energy transfer. Our experimental results and theoretical calculations show that the mechanism that governs the Förster energy transfer is mainly due to dipole-dipole interaction within BODIPY-doped single clusters (nodes) but not due to cluster-cluster interaction. It is observed that FRET efficiency significantly decreases as the dipole-dipole distance increases within a single

cluster upon water swelling. Such a large change in FRET efficiency can, for example, provide a handle for measuring stimuli responsiveness of hydrogels to be employed as a sensing mechanism for an application in concern.

REFERENCES

1. Canham, L. T., "Silicon quantum wire array fabrication by electrochemical and chemical dissolution of wafers", *Applied Physics Letters*, Vol. 57, No. 10, pp. 1046-1048, 1990.

2. Canham, L. T., "Laser Dye Impregnation of Oxidized Porous Si on Si Wafer", *Applied Physics Letters*, Vol. 63, No. 3, pp. 337-339, 1993.

3. Charrier, J., E. Gorju, L. Haji and M. Guendouz, "Optical Waveguides Fabricated from Oxidised Porous silicon", *Journal of Porous Materials*, Vol. 7, pp. 243-246, 2000.

4. Chouket, A., H. Elhouichet, M. Oueslati, H. Koyama, B. Gelloz and N. Koshida, "Energy transfer in porous-silicon/laser-dye composite evidenced by polarization memory of photoluminescence", *Applied Physics Letters*, Vol. 91, No. 21, pp. 211902-211904, 2007.

5. Letant, S. and J. C. Vial, "Energy transfer in dye impregnated porous silicon", *Journal of Applied Physics*, Vol. 82, No. 21, pp. 397-401, 1997.

6. Wu, E. C., J. H. Park, J. Park, E. Segal, F. Cunin and M. J. Sailor, "Oxidation-triggered release of fluorescent molecules or drugs from mesoporous Si microparticles", *American Chemical Society Nano*, Vol. 2, No. 11, pp. 2401-2409, 2008.

7. Gonzalez-Diaz, B., R. Guerrero-Lemus, J. Mendez-Ramos, B. Diaz-Herrera and V. D. Rodriguez, "Gradual oxidation of stain etched porous silicon nanostructures applied to silicon-based solar cells", *Sensors and Actuators A: Physical*, Vol. 150, No. 1, pp. 97-101, 2009.

8. Barillaro, G., A. Diligenti, A. Nannini, L. M. Strambini, E. Comini and G. Sberveglieri, "Low-concentration NO_2 detection with an adsorption porous silicon FET",

IEEE Sensors Journal, Vol. 6, pp. 19-23, 2006.

9. Charrier, J., M. Kloul, P. Pirasteh, J.-F. Bardeau, M. Guendouz, A. Bulou and L. Haji, "Structural and optical studies of porous silicon buried waveguides: Effects of oxidation and pore filling using DR1 dyes", *Optical Materials*, Vol. 30, No. 3, pp. 431-437, 2007.

10. Ogata, Y. H., T. Tsubo, T. Sakka and S. Naito, "Oxidation of porous silicon in dry and wet environments under mild temperature conditions", *Journal of Porous Materials*, Vol. 7, No. 1, pp. 63-66, 2000.

11. Mawhinney, D. B., J. A. Glass and J. T. Yates, "FTIR Study of the Oxidation of Porous Silicon", *Journal of Physical Chemistry B*, Vol. 101, No. 7, pp. 1202-1206, 1997.

12. Zhang, Y., J. Yu, D. J. S. Birch and Y. Chena, "Gold nanorods for fluorescence lifetime imaging in biology", *Journal of Biomedial Optics*, Vol. 15, No. 2, pp. 20504-20506, 2010.

13. Festy, F., S. M. Ameer-Beg, T. Ngab and K. Suhling, "Imaging proteins in vivo using fluorescence lifetime microscopy", *Molecular Biosystems*, Vol. 3, No. 6, pp. 381391, 2007.

14. Chan, F. K. M., "Monitoring molecular interactions in living cells using flow cytometric analysis of Fluorescence Resonance Energy Transfer", *Methods in Molecular Biology*, Vol. 261, pp. 371-381, 2004.

15. Watson, P., A. T. Jones and D. J. Stephens, "Intracellular trafficking pathways and drug delivery: fluorescence imaging of living and fixed cells", *Advanced Drug Delivery Reviews*, Vol. 57, No. 1, pp. 43-61, 2005.

16. Sytnik, A. and I. Litvvinyuk, "Energy transfer to a proton-transfer fluorescence probe: Tryptophan to a flavonol in human serum albumin", *Proceedings of the*

National Academy of Sciences of the United States of America, Vol. 93, No. 23, pp. 12959-12963, 1996.

17. Truong, K. and M. Ikura, "The use of FRET imaging microscopy to detect protein-protein interactions and protein conformational changes in vivo", *Current Opinion in Structural Biology*, Vol. 11, No. 5, pp. 573-578, 2001.

18. Kaper, T., I. Lager, L. L. Looger, D. Chermak and W. B. Frommer, "Fluorescence resonance energy transfer sensors for quantitative monitoring of pentose and disaccharide accumulation in bacteria", *Biotechnology for Biofuels*, Vol. 1, No. 11, pp. 11-20, 2008.

19. Sahoo, H., D. Roccatano, A. Hennig and W. M. Nau, "A 10-A spectroscopic ruler applied to short polyprolines", *Journal of the American Chemical Society*, Vol. 129, No. 31, pp. 9762-9772, 2007.

20. Lee, K. Y., J. A. Rowley, P. Eiselt, E. M. Moy, K. H. Bouhadir and D. J. Mooney, "Controlling mechanical and swelling properties of alginate hydrogels independently by cross-linker type and cross-linking density", *Macromolecules*, Vol. 33, No. 11, pp. 4291-4294, 2000.

21. Binstock, E. E., A. Bentolila, N. Kumar, H. Harel and A. Domb, "Preparation, characterization, and sterilization of hydrogel sponges for iontophoretic drug-delivery use", *Polymers for Advanced Technologies*, Vol. 18, No. 9, pp. 720-730, 2007.

22. Klimov, V. V., "Spontaneous emission rate of an excited atom placed near a nanofiber", *Physical Review A: Atomic, Molecular, and Optical Physics*, Vol. 69, No. 1, pp. 13812-13828, 2004.

23. Lakowicz, J. R., "Radiative Decay Engineering: Biophysical and Biomedical Applications", *Analytical Biochemistry*, Vol. 298, No. 1, pp. 1-24, 2001.

24. Braginsky, V. B., M. L. Gorodetsky and V. S. Ilchenko, "Quality-factor and nonlinear properties of optical whispering-gallery modes", *Physics Letters A*, Vol. 137, No. 7, pp. 393-397, 1989.

25. Carminati, R., J. -J. Greffet , C. Henkel and J. M. Vigoureux, "Radiative and non-radiative decay of a single molecule close to a metallic nanoparticle", *Optics Communications*, Vol. 261, No. 2, pp. 368-375, 2006.

26. Dekker, C., "Carbon nanotubes as molecular quantum wires", *Physics Today*, Vol. 52, No. 5, pp. 22-28, 1999.

27. Chen, Y., M. B. Donoghue, Y. -F. Huang, H. Kang, J. A. Phillips, X. Chen, M.-C. Estevez, C. J. Yang and W. Tan, "A Surface Energy Transfer Nanoruler for Measuring Binding Site Distances on Live Cell Surfaces", *Journal of the American Chemical Society*, Vol. 132, No. 46, pp. 16559-16570, 2010.

28. McGraw, C. M., G. Khalil and J. B. Callis, "Comparison of Time and Frequency Domain Methods for Luminescence Lifetime Measurements", *The Journal of Physical Chemistry C*, Vol. 112, No. 21, pp. 8079-8084, 2008.

29. Möller, M. and A. Denicola, "Protein Tryptophan accessibility studied by fluorescence quenching", *Biochemistry and Molecular Biology Education*, Vol. 30, No. 3, pp. 175-178, 2002.

30. Chang, G. G. and H. J. Lee, "Monitoring protein conformational changes by quenching of intrinsic fluorescence", *Journal of Biochemical and Biophysical Methods*, Vol. 9, No. 4, pp. 351-355, 1984.

31. Nakamura, I., A. C. Shi, R. Nutiu, J. M. Y. Yu and Y. Li, "Kinetics of signaling-DNA-aptamer-ATP binding", *Physical Review E*, Vol. 79, No. 3, pp. 31906-31914, 2009.

32. Albani, J. R., "Structure and dynamics of macromolecules: Absorption and Fluo-

rescence studies", 1^{st} edition, Elsevier, Amsterdam, 2004.

33. Kuhn, H., "Classical aspects of energy transfer in molecular systems", *Journal of Chemical Physics*, Vol. 53, pp. 101-108, 1970.

34. Verma, P. K. and S. K. Pala, "Ultrafast resonance energy transfer in bio-molecular systems", *The European Physical Journal D*, Vol. 60, No. 1, pp. 137156, 2010.

35. Persson, B. N. J. and N. D. Lang, "Electron-hole-pair quenching of excited states near a metal", *Physical Review B*, Vol. 26, No. 10, pp. 5409-5415, 1982.

36. Singh, M. P. and G. F. Strouse, "Involvement of the LSPR Spectral Overlap for Energy Transfer between a Dye and Au Nanoparticle", *Journal of American Chemical Society*, Vol. 132, No. 27, pp. 9383-9391, 2010.

37. Das, P., D. Sarkar and N. Chattopadhyay, "Fluorescence energy transfer from a β-carboline analogeu to a cationic photosensitizer in aqueous solution", *Indian Journal of Chemistry*, Vol. 47, pp. 843-847, 2008.

38. Kang, J. S. and J. R. Lakowicz, "Fluorescence resonance energy transfer in calf thymus DNA from a long-lifetime metal-ligand complex to nile blue", *Journal of Biochemistry and Molecular Biology*, Vol. 34, No. 6, pp. 551-558 , 2001.

39. Lakowicz, J. R., "Principles of Fluorescent Spectroscopy", 2^{nd} edition, Kluwer Plenum, New York, 1999.

40. Mayor, S. and S. Bilgrami, "Fretting about FRET in Cell and Structural Biology", *In Evaluating Techniques in Biochemical Research*, D. Zuk, ed., Cambridge, MA: Cell Press, 2007.

41. Gaburro, Z., H. You and D. Babic, "Effect of resistivity and current density on photoluminescence in porous silicon produced at low HF concentration", *Journal of Applied Physics*, Vol. 84, No. 11, pp. 6345-6350, 1998.

42. Cheung, M. C. , P. J. R. Roche, M. H. Hassan, A. G. Kirk, Z. Mi and V. P. Chodavarapu, "Controlling optical properties and surface morphology of dry etched porous silicon", *Journal of Nanophoton*, Vol. 5, pp. 53503-53510, 2011.

43. Chiboub, N., N. Gabouze, J. N. Chazalviel, F. Ozanam, S. Moulay and A. Manseri, "Nanopore formation on low-doped p-type silicon under illumination", *Applied Surface Science*, Vol. 256, No. 12, pp. 3826-3831, 2010.

44. Erdamar, O., B. Bilen, Y. Skarlatos, G. Aktas and M. N. Inci, "Effects of humidity and acetone on the optical and electrical properties of porous silicon nanostructures", *Physica status solidi. C*, Vol. 4, No. 2, pp. 601-603, 2007.

45. Takagahara, T. and K. Takeda, "Theory of the quantum confinement effect on excitons in quantum dots of indirect-gap materials", *Physical Review B*, Vol. 46, No. 23, pp. 15578-15581, 1992.

46. Ciurea, M. L., "Quantum confinement in nanocrystalline silicon", *Journal of Optoelectronics and Advanced Materials*, Vol. 7, No. 5, pp. 2341-2346, 2005.

47. Naddaf, M. and H. Hamadeh, "Visible luminescence in photo-electrochemically etched p-type porous silicon: Effect of illumination wavelength", *Materials Science and Engineering C*, Vol. 29, No. 7, pp. 2092-2098, 2009.

48. Doan, V. V., R. M. Penner and M. J. Sailor, "Enhanced photoemission from short-wavelength photochemically etched porous silicon", *Journal of Physical Chemistry*, Vol. 97, No. 17, pp. 4505-4508, 1993.

49. Kumar, R., H. S. Mavi and A. K. Shukla, "Macro and microsurface morphology reconstructions during laser-induced etching of silicon", *Micron*, Vol. 39, No. 3, pp. 287-293, 2008.

50. Crouch, C. H., J. E. Carey, J. M. Warrender, M. J. Aziz and E. Mazur, "Comparison of structure and properties of femtosecond and nanosecond laser-structured

silicon", *Applied Physics Letters*, Vol. 84, No. 11, pp. 1850-1852, 2004.

51. Saygili, A. C., "Coherence and wavelength effects on the growth mechanism of porous silicon nano-structures", M.S. Thesis, Boğaziçi University, 2009.

52. Sivakov, V., G. Andra, A. Gawlik, A. Berger, J. Plentz, F. Falk and S. H. Christiansen, "Silicon nanowire-based solar cells on glass: synthesis, optical properties, and cell parameters", *Nano Letters*, Vol. 9, No. 4, pp. 1549-1554, 2009.

53. Dancil, K. S., D. P. Greiner and M. J. Sailor, "A Porous Silicon Optical Biosensor: Detection of Reversible Binding of IgG to a Protein A-Modified Surface", *Journal of American Chemical Society*, Vol. 121, No. 34, pp. 7925-7930, 1999.

54. Park, N. M., T. S. Kim and S. J. Park, "Band gap engineering of amorphous silicon quantum dots for light-emitting diodes", *Applied Physics Letters*, Vol. 78, No. 17, pp. 2575-2577, 2001.

55. Gersten, J. I. and A. Nitzan, "Spectroscopic properties of molecules interacting with small dielectric particles", *Journal of Chemical Physics*, Vol. 75, No. 3, pp. 1139-1152, 1981.

56. Shepherd, J. L., A. Kell, E. Chung, C. W. Sinclar, M. S. Workentin and D. Bizzotto, "Selective Reductive Desorption of a SAM-Coated Gold Electrode Revealed Using Fluorescence Microscopy", *Journal of American Chemical Society*, Vol. 126, No. 26, pp. 8329-8335, 2004.

57. Astilean, S., S. Garrett, P. Andrew and W. L. Barnes, "Controlling the fluorescence lifetimes of dyes in nanostructured geometries", *Journal of Molecular Structure*, Vol. 277, pp. 651-653, 2003.

58. Bardhan, R., N. K. Grady, J. R. Cole, A. Joshi and N. J. Halas, "Fluorescence Enhancement by Au Nanostructures: Nanoshells and Nanorods", *ACS Nano*, Vol. 3, No. 3, pp. 744752, 2009.

59. Vasic, M. R., L. D. Cola and H. Zuilhof, "Efficient Energy Transfer between Silicon Nanoparticles and a Ru-Polypyridine Complex", *Journal of Physical Chemistry C*, Vol. 113, No. 6, pp. 2235-2240, 2009.

60. Wu, E. C., J. H. Park, J. Park, E. Segal, F. Cunin and M. J. Sailor, "Oxidation-triggered release of fluorescent molecules or drugs from mesoporous Si microparticles", *ACS Nano*, Vol. 2, No. 11, pp. 2401-2409, 2008.

61. Acikgoz, S., G. Aktas, M. N. Inci, H. Altin and A.Sanyal, "FRET between BODIPY azide dye clusters within PEG-based hydrogel: a handle to measure stimuli responsiveness", *Journal of Physical Chemistry B*, Vol. 114, No. 34, pp. 10954-10960, 2010.

62. Jennings, T. L., M. P. Singh and G. F. Strouse, "Fluorescent Lifetime Quenching near d=1.5 nm Gold Nanoparticles: Probing NSET Validity", *Journal of American Chemical Society*, Vol. 128, No. 16, pp. 5462-5467, 2006.

63. Yun, C. S., A. Javier, T. Jennings, M. Fisher, S. Hira, S. Peterson, B. Hopkins, N. O. Reich and G. F. Strouse, "Nanometal Surface Energy Transfer in Optical Rulers, Breaking the FRET Barrier", *Journal of American Chemical Society*, Vol. 127, No. 9, pp. 3115-3119, 2005.

64. Sen, T., K. K. Haldar and A. Patra, "Au Nanoparticle-Based Surface Energy Transfer Probe for Conformational Changes of BSA Protein", *Journal of Physical Chemistry C*, Vol. 112, No. 46, pp. 17945-17951, 2008.

65. Jennings, T. L., J. C. Schlatterer, M. P. Singh, N. L. Greenbaum and G. F. Strouse, "NSET Molecular Beacon Analysis of Hammerhead RNA Substrate Binding and Catalysis", *Nano Letters*, Vol. 6, No. 7, pp. 1318-1324, 2006.

66. Hao, P. H., X. Y. Hou, F. L. Zhang and X. Wang, "Energy band lineup at the porous silicon/silicon heterointerface measured by electron spectroscopy", *Applied Physics Letters*, Vol. 64, No. 26, pp. 3602-3604, 1994.

67. Islam, M. N., S. K. Ram and S. J. Kumar, "Band edge discontinuities and carrier transport in c-Si/porous silicon heterojunctions", *Journal of Physics D: Applied Physics*, Vol. 40, No. 19, pp. 5840-5846, 2007.

68. Acikgoz, S., I. Sarpkaya, P. Milas, M. N. Inci, G. Demirci and R. Sanyal, "Investigation of Fluorescence Dynamics of BODIPY Embedded in Porous Silicon and Monitoring Formation of a SiO2 Layer via a Confocal FLIM-Based NSET Method", *Journal of Physical Chemistry C*, Vol. 115, No. 45, pp. 22186-22190, 2011.

69. Altin, H., I. Kosif and R. Sanyal, "Fabrication of Clickable Hydrogels via Dendron-Polymer Conjugates", *Macromolecules*, Vol.43, No. 8, pp. 3801-3808, 2010.

70. Kong, H. J., C. J. Kim, N. Huebsch, D. Weitz and D. J. Mooney, "Noninvasive Probing of the Spatial Organization of Polymer Chains in Hydrogels Using Fluorescence Resonance Energy Transfer (FRET)", *Journal of American Chemical Society*, Vol. 129, No. 15, pp. 4518-4519, 2007.

71. Ostroha, J., M. Pong, A. Lowman and A. Dan, "Controlling the Collapse/Swelling Transition in Charged Hydrogels", *Biomaterials*, Vol. 25, No. 18, pp. 4345-4353, 2004.

72. Barakat, M. A. and N. Sahiner, "Cationic hydrogels for toxic arsenate removal from aqueous environment", *Journal of Environmental Management*, Vol. 88, pp. 955-961, 2008.

73. Drooge, D. J., K. Braeckmans, W. L. J. Hinrichs, K. Remaut, S. C. Smedt and H. W. Frijlink, "Characterization of the mode of incorporation of lipophilic compounds in solid dispersions at the nano-scale using fluorescence resonance energy transfer (FRET)", *Macromolecular Rapid Communications*, Vol. 27, No. 14, pp. 1149-1155, 2006.

74. Toprak, E., A. Yildiz, M. T. Hoffman, S. S. Rosenfeld and P. R. Selvin, "Why kinesin is so processive", *Proceedings of National Academy of Sciences*, Vol. 106,

pp. 12717-12722, 2009.

75. Wang, C., Q. H. Wu, Z. Wang and Zhao J., "Study of the interaction of carbamazepine with bovine serum albumin by fluorescence quenching method", *Analytical Sciences*, Vol. 22, pp. 435-438, 2006.

76. Rahimi, Y., A. Goulding, S. Shrestha, S. Mirpuri and S. K. Deo, "Mechanism of copper induced fluorescence quenching of red fluorescent protein DsRed", *Biochemical and Biophysical Research Communications*, Vol. 370, No. 1, pp. 57-61, 2008.

77. Johansson, M. K., H. Fidder, D. Dick and R. M. Cook, "A New Strategy to Fluorescence Quenching in Dual-Labeled Oligonucleotide Probes", *Journal of American Chemical Society*, Vol. 124, No. 24, pp. 6950-6956, 2002.

78. Rahman, M. and H. J. Harmon, "Absorbance change and static quenching of fluorescence of meso-tetra(4-sulfonatophenyl)porphyrin (TPPS) by trinitrotoluene (TNT)", *Spectrochim Acta, Part A Molecular Biomolecular Spectroscopy*, Vol. 65, No. 3, pp. 901-906, 2006.

79. Mcguire, R. and I. Feldman, "Static and dynamic quenching of protein fluorescence. II. lysozyme", *Biopolymers*, Vol. 14, pp. 1095-1102, 1975.